MICROSTRUCTURAL DESIGN IN MARTENSITIC STAINLESS STEELS VIA QUENCHING AND PARTITIONING TO IMPROVE THEIR MECHANICAL PROPERTIES

by

Andrés Sierra Soraluce

A dissertation submitted in partial fulfillment of the requirements for the degree of Doctor of Philosophy in

Materials Science and Engineering

Universidad Carlos III de Madrid

Advisor:

Dr. Ilchat Sabirov

Tutor:

Prof. José Manuel Torralba Castelló

December 2023

To the people in my life.
Your actions have consequences, this is just one.

ACKNOWLEDGEMENTS

I begin by expressing my heartfelt gratitude to Dr. Ilchat Sabirov and Prof. Jose Manuel Torralba Castelló for their unwavering guidance throughout my years of Ph.D. research. I also extend my appreciation to Dr. Jon Mikel Molina Aldareguia for his support, even as my thesis ventured away from his field.

Sincere thanks are due to the QPINOX consortium partners for their outstanding collaboration, with special acknowledgment to Dr. Ali Smith for his role as the project coordinator. I am deeply thankful to Prof. Maria Jesús Santofimia Navarro for inviting me to conduct a three-month stay at TU Delft.

I would also like to acknowledge the wonderful people at IMDEA Materials who have made my time there truly memorable. The friendships forged will last a lifetime. My gratitude extends to those outside of IMDEA who have endured my presence with remarkable patience.

Lastly, heartfelt thanks to my parents and sister. Their support has been my grounding force and a constant upliftment in my journey.

PUBLISHED AND SUBMITTED CONTENT

1. "**Effect of microstructure on tensile properties of quenched and partitioned martensitic stainless steels**"
   A. Sierra-Soraluce, G. Li, M.J. Santofimia, J.M. Molina-Aldareguia, A. Smith, M. Muratori & I. Sabirov.
   Published in *Materials Science and Engineering: A*, vol 864, 144540.
   February 2023
   DOI: 10.1016/j.msea.2022.144540
   Article partly included in the thesis: microstructural characterization included in section 5.1.2 and mechanical properties in section 5.2.1.
   The material from this source included in this thesis is not singled out with typographic means and references.
   Role: Experimental work and article draft.

2. **"Assessing the feasibility of cold forming of automotive parts from quenched and partitioned martensitic stainless steels"**
   J.L. de Pablos, A. Sierra-Soraluce, I. Sabirov, M. Muratori & A. Smith.
   Published in *Steel Research International,* vol 95, issue 1, 2300280.
   August 2023
   DOI: 10.1002/srin.202300280
   Article partly included in the thesis: model definition included in section 4.1 and simulation results reported in sections 5.4.2 and 5.4.3.
   The material from this source included in this thesis is not singled out with typographic means and references.
   Role: Experimental work, data generation and supply, article drafting.

3. **"Exploring the effect of complex hierarchic microstructure of quenched and partitioned martensitic stainless steels on their high cycle fatigue behaviour"**
   A. Sierra-Soraluce, G. Li, M.J. Santofimia, J.M. Molina-Aldareguia, A. Smith, M. Muratori & I. Sabirov.
   Published in *Materials & Design,* vol 233, 112286.
   September 2023
   DOI: 10.1016/j.matdes.2023.112286
   Article partly included in the thesis: microstructural characterization included in section 5.1.3, mechanical properties in section 5.2.2, and fatigue behaviour characterization in section 5.3.
   The material from this source included in this thesis is not singled out with typographic means and references.
   Role: Experimental work and article draft.

4. **"Resistance spot welding of QP stainless steels: role of heat treatment and microstructure on joint strength"**
   A. Smith, E. Macia, M. Muratori, A. Sierra-Soraluce & I. Sabirov.
   Published in *Key Engineering Materials,* vol 966, 71-76.
   November 2023
   DOI: 10.4028/p-22MapG
   Article not included in the thesis.
   Role: Experimental work and data interpretation.

ARTICLES UNDER PREPARATION

- "Fatigue crack initiation and propagation in multiphase stainless steels"
- "Microstructure evolution during formability testing of Q&P martensitic stainless steels"

OTHER RESEARCH MERITS

ORAL PRESENTATIONS AT INTERNATIONAL CONFERENCES

1. "**Control of strain hardening ability and uniform elongation via microstructural design in martensitic stainless steels**"
   A. Sierra-Soraluce, G. Li, I. Sabirov, J.M. Molina-Aldareguia, M.J. Santofimia & A. Smith
   ESAFORM Conference 2022
   April 2022. Braga, Portugal.

2. "**High-cycle fatigue behaviour of quenching and partitioning (Q&P) treated stainless steels**"
   A. Sierra-Soraluce, J.M. Molina-Aldareguia, A. Smith, M. Muratori & I. Sabirov
   19th International Conference on Strength of Materials (ICSMA)
   June 2022. Metz, France.

3. "**Fatigue crack initiation and propagation mechanisms in quenching and partitioning (Q&P) treated stainless steels**"
   A. Sierra-Soraluce, G. Li, J.M. Molina-Aldareguia, A. Smith, M. Muratori, M.J. Santofimia & I. Sabirov
   Junior Euromat 2022
   July 2022. Coimbra, Portugal.

4. "**Fatigue performance of quenching and partitioning (Q&P) treated martensitic stainless steels**"
   A. Sierra-Soraluce, G. Li, J.M. Molina-Aldareguia, A. Smith, M. Muratori, M.J. Santofimia & I. Sabirov
   10th International Conference on Fatigue, Fracture and Wear (FFW) 2022
   August 2022. Online event.

5. "**Mechanical properties and strain hardening behaviour of quenching and partitioning (Q&P) treated martensitic stainless steels**"
   A. Sierra-Soraluce, G. Li, I. Sabirov, J.M. Molina-Aldareguia, A. Smith, M. Muratori & M.J. Santofimia
   Material Science and Engineering (MSE) Congress 2022
   September 2022. Darmstadt, Germany.

6. "**The effect of stress state on the microstructure evolution during plastic deformation of Q&P-treated martensitic stainless steels**"
   A. Sierra-Soraluce, J.L. de Pablos, J.M. Molina-Aldareguia, A. Smith, M. Muratori and I. Sabirov
   8th International Conference of the Hellenic Metallurgical Society (ICHMS)
   December 2022. Patras, Greece.

7. "**Cold-forming of quenched and partitioned martensitic stainless steels: from Nakajima to simulation**"
A. Sierra-Soraluce, J.L. de Pablos, A. Smith, M. Muratori and I. Sabirov
7th International Conference of Engineering Against Failure (ICEAF)
June 2023. Spetses Island, Greece.

AWARDS

- Best oral presentation at 10th International Conference on Fatigue, Fracture and Wear (FFW) 2022

ABSTRACT

Quenching and partitioning (Q&P) treatment has been proven effective in manufacturing advanced high strength steels with high content of retained austenite, showing the improved balance of high strength and sufficient ductility. This method has been very well elaborated for carbon steel processing over the last two decades. Though it can also be potentially applied for processing other steel families, this has been scarcely studied. Recent research, albeit limited, has shown the viability of Q&P treatment for processing martensitic stainless steels showing an improved balance of high strength and sufficient ductility. However, their application-related properties have never been investigated.

This thesis focuses on the effect of chemistry and heat treatment parameters on the microstructure and properties of Q&P-treated martensitic stainless steels. Three different martensitic stainless steels with different contents of alloying elements are subjected to Q&P processing with varying Q&P parameters. It is demonstrated that the Q&P-treated martensitic stainless steels can show a favorable combination of enhanced strength and sufficient tensile ductility. Their uniform elongation increases with the increasing volume fraction of retained austenite, attributed to the transformation induced plasticity (TRIP) effect. The alloy-process-microstructure-property relationship is discussed.

High-cycle fatigue performance and formability of the Q&P-treated martensitic stainless steels is explored. The results reveal satisfactory high-cycle fatigue performance, surpassing that of their traditional counterparts. Fatigue cracks predominantly form and propagate along martensite packet and block boundaries, while prior austenite grain boundaries, MnS inclusions and nanocarbides have minimal influence on fatigue crack formation and growth.

To assess the mechanical behavior of the Q&P-treated martensitic stainless steels during cold forming, a computational approach is developed. The Johnson-Cook (J-C) constitutive model and Forming Limit Diagram (FLD) are derived and validated for each alloy using experimental data from tensile and Nakajima tests. From the simulated FLD, a theoretical Forming Limit Stress Diagram (FLSD) is calculated. The latter is used as a fracture criterion for the cold-forming process. Cold stamping simulations of two automotive parts, the B-pillar and tunnel, are conducted using the J-C constitutive model and the FLSD. The study demonstrates successful cold forming of the tunnel using all three studied steels. In contrast, extensive cracking is expected during the cold forming of the B-pillar for all materials.

The life cycle cost analysis reveals that initial materials acquisition costs dominate total material costs, followed by final heat treatments, casting, and hot rolling. Q&P-treated grades are more cost-effective than traditional austenitic stainless steel, as the latter is comparatively expensive due to its high nickel content. The Q&P process demonstrates low energy intensity and cost, indicating minimal impact on overall manufacturing energy and material costs upon implementation. While the Q&P process has no direct effect on carbon emissions, its adoption may indirectly reduce manufacturing-related emissions by utilizing lower nickel content materials compared to standard austenitic stainless steels.

RESUMEN

El tratamiento térmico de "temple y particionado" ha demostrado su eficacia en la fabricación de aceros avanzados de alta resistencia con alto contenido en austenita retenida, logrando un equilibrio mejorado entre alta resistencia y suficiente ductilidad. Aunque ampliamente estudiado en las dos últimas décadas para aceros al carbono, su aplicabilidad a otras familias de aceros apenas ha sido investigada. Estudios recientes confirman la viabilidad de aplicar este tratamiento a aceros inoxidables martensíticos, alcanzando este equilibrio mejorado entre resistencia y ductilidad. Sin embargo, las propiedades industriales aún han de ser investigadas.

Esta tesis se centra en el impacto de la composición química y los parámetros del tratamiento térmico sobre la microestructura y las propiedades de los aceros inoxidables martensíticos tratados con temple y particionado. Tres aceros inoxidables martensíticos con diferentes contenidos en sus elementos de aleación fueron tratados mediante temple y particionado, variando sus parámetros de tratamiento. Se demuestra que estos aceros inoxidables martensíticos tratados con temple y particionado alcanzan una resistencia mejorada manteniendo suficiente ductilidad. Su elongación uniforme aumenta con la fracción volumétrica de austenita retenida atribuida al efecto de la transformación inducida por plasticidad (TRIP). Se examina la relación entre aleación, proceso, microestructura y propiedades.

El rendimiento a fatiga de alta frecuencia y la formabilidad de los aceros inoxidables martensíticos tratados con temple y particionado son estudiados. Los resultados revelan un rendimiento satisfactorio de estos materiales a fatiga de alta frecuencia, superando a homólogos convencionales. Las grietas de fatiga se forman y propagan predominantemente a lo largo de las fronteras de paquetes y bloques de martensita, mientras que las fronteras de grano de austenita primitiva, las inclusiones MnS y los nanocarburos tienen una influencia mínima en la formación y el crecimiento de las grietas de fatiga.

Se desarrolla un enfoque computacional para evaluar el comportamiento mecánico de los aceros inoxidables martensíticos tratados con temple y particionado conformados en frío. El modelo constitutivo de Johnson-Cook (JC) y el diagrama límite de conformado (FLD) se derivan y validan para cada aleación utilizando datos experimentales de tracción uniaxial y ensayos de Nakajima. Del FLD simulado, se calcula un diagrama límite de tensiones de conformado (FLSD) teórico. Este es utilizado como criterio de fractura en el proceso de conformado en frío. El estampado en frío de dos piezas automovilísticas, un pilar B y un túnel, es modelado usando el modelo constitutivo JC y el FLSD. Se demuestra que el túnel puede ser conformado en frío con éxito para las tres aleaciones estudiadas. Por otro lado, se espera un agrietamiento extenso en el conformado en frío de un pilar B para todas las aleaciones.

El análisis de los costes del ciclo de vida revela que los costes iniciales de adquisición de las materias primas dominan el coste total, seguido por los tratamientos térmicos finales, la colada y el laminado en caliente. Las aleaciones tratadas por temple y particionado son más económicas que los aceros inoxidables austeníticos, siendo estos últimos más caros debido a su contenido superior de níquel. El proceso de temple y particionado muestra baja intensidad de energía y coste, resultando en un impacto mínimo en los gastos globales de materiales y energía por su implementación. Aunque el proceso de temple y particionado no tenga un efecto directo en las emisiones de carbono, su adopción puede reducir de manera indirecta las emisiones atribuidas a la fabricación al utilizar contenidos inferiores de níquel en comparación con los aceros inoxidables austeníticos estándar.

TABLE OF CONTENTS

1. INTRODUCTION 1

1.1. Stainless Steels 2

1.1.1. Classification 2

1.1.2. Processing of standard martensitic stainless steel 4

1.1.3. Typical microstructures of martensitic stainless steels 5

1.1.4. Properties of martensitic stainless steel 6

1.1.4.1. Mechanical properties 6

1.1.4.2. Application-related properties 7

1.2. Quenching and partitioning as a promising method for martensitic stainless steels 8

1.2.1. Concept of quenching and partitioning (Q&P) 8

1.2.2. Microstructure and properties achieved in carbon steels via Q&P 9

1.2.3. Current development of Q&P process for manufacturing martensitic stainless steel 10

1.2.3.1. Microstructure in martensitic stainless steel via Q&P 10

1.2.3.2. Properties reached in Q&P-treated martensitic stainless steels 11

2. MOTIVATION & OBJECTIVES 13

3. MATERIALS & EXPERIMENTAL PROCEDURES 15

3.1. Materials 15

3.2. Q&P treatment 17

3.2.1. Physical simulation of the Q&P process, using GLEEBLE 3800 system 17

3.2.1.1. The GLEEBLE 3800 system 17

3.2.1.2. Q&P parameters screened using the GLEEBLE 3800 system 18

3.2.2. Q&P processing of large sheets 19

3.3. Microstructural characterization 20

3.3.1. Scanning Electron Microscopy (SEM) & Energy Dispersive X-Ray Spectroscopy (EDS) 20

3.3.2. Electron Backscatter Diffraction (EBSD) analysis 21

3.3.3. X-Ray Diffractometry (XRD) analysis 22

3.3.4. Magnetometry study 23

3.3.5. High resolution Transmission Electron Microscopy (TEM) & Energy Dispersive Spectroscopy (EDS) 24

3.4. Characterization of properties 24

3.4.1. Tensile testing 24

3.4.1.1. Tensile testing of sub-size samples 24

3.4.1.2. Standard tensile testing 25

3.4.2. High-cycle fatigue 25

3.4.3. Formability testing 25

4. FEM MODEL FOR FORMABILITY TESTING AND COLD-FORMING OF AUTOMOTIVE PARTS 27

4.1.1. Johnson-Cook model in formability studies 27

4.1.1.1. Johnson-Cook constitutive relations 28

4.1.2. Development of FEM models 28

5. RESULTS & DISCUSSION 31

5.1. Effect of chemical composition and Q&P parameters on the microstructure 31

5.1.1. Microstructure of the as-received materials 31

5.1.2. Microstructure of samples after physical simulation of Q&P process 33

5.1.2.1. Volume fraction of retained austenite measured using different characterization techniques 38

5.1.2.2. Carbon content determination results from XRD measurements 40

5.1.2.3. Selection of optimum Q&P parameters for processing large sheets 41

5.1.3. Microstructure of large Q&P-treated sheets 42

5.1.4. Conclusions to Section 5.1 46

5.2. Effect of Q&P treatment on tensile properties 46

5.2.1. Tensile behavior of sub-size samples from physical simulation experiments 46

5.2.1.1. Tensile properties of sub-size specimens from physical simulation experiments 46

5.2.1.2. Effect of tensile deformation on the microstructure of the GLEEBLE Q&P-treated sub-size samples 49

5.2.2. Tensile behavior of large Q&P-treated sheets 55
5.2.3. Conclusions to Section 5.2 55
5.3. High-cycle fatigue behavior of Q&P-treated large sheets 56
5.3.1. Fatigue performance 56
5.3.2. Analysis of mechanisms governing fatigue behavior 59
5.3.3. Interaction of fatigue crack with microstructural constituents 62
5.3.4. Conclusions to Section 5.3 69
5.4. Formability of the Q&P-treated large sheets 69
5.4.1. Results of Nakajima testing 69
5.4.2. Validation of the developed model 75
5.4.2.1. Approach to plasticity simulation: Johnson-Cook vs. traditional stress-strain curves 75
5.4.2.2. Plastic strain distribution and FLD curves comparison in the Nakajima tested samples 77
5.4.2.3. FLSD vs FLD: improving fracture modeling 80
5.4.3. Feasibility of the developed grades for stamping automotive parts 81
5.4.4. Conclusions to Section 5.4 85
6. COST ANALYSIS & FEASABILITY 87
6.1. Production costs analysis 87
6.1.1. Initial material acquisition costs 87
6.1.2. Cost of steel processing 88
6.1.3. Other related costs 91
6.1.4. Summary of production costs analysis 91
6.2. Environmental effect 92
6.3. Conclusion to Chapter 6 94
7. CONCLUSIONS 95
8. FUTURE WORK 97
9. REFERENCES 99

TABLE OF FIGURES

Figure 1-1. Ashby plot, elongation vs ultimate tensile strength for different generations of AHSS [4]. 1

Figure 1-2. Schaeffler diagram for stainless steels classification [9]. 2

Figure 1-3. Typical microstructure of AISI 410 stainless steel, Vilella's etching [13]. 5

Figure 1-4. Hierarchical structure of martensite [15]. 6

Figure 1-5. A schematic presentation of the Q&P heat treatment, where A_{c3} indicates the temperature above which only austenite is present in the microstructure, M_S martensite start temperature, QT quenching temperature and RT room temperature. C_i, C_γ and C_m represent initial carbon concentration in austenite, carbon concentration in retained austenite and carbon concentration in martensite, respectively. Color code: austenite in white, retained austenite in yellow, fresh martensite in dark blue and tempered martensite in light blue. Adapted graph from [32]. 9

Figure 1-6. Engineering stress–strain curves of Q&P-treated 410 grade (partitioning at 723 K) and quench-and-tempered (Q&T) specimen (tempered at 723 K – for 0.12 ks) with the same tensile strength [43]. 11

Figure 3-1. Q&P treatment in the GLEEBLE 3800 system: a) experimental set-up for sample treatment in the GLEEBLE chamber, b) geometry of specimen for Q&P treatment in the GLEEBLE chamber, and c) subsequent machining of the sub-size tensile samples from the GLEEBLE Q&P-treated coupons. 18

Figure 3-2. Q&P heat treatment for the large sheets. 20

Figure 3-3. A typical EBSD phase map of 420ma sample with identified microstructural constituents: a) in the first step, retained austenite (RA) in the martensitic matrix is detected; b) in the second step, fresh martensite (FM) and tempered martensite (TM) are discriminated. FM is in blue, RA is in red, and TM is the matrix. 22

Figure 3-4. Geometry of samples used for high-cycle fatigue testing. 25

Figure 3-5. Five geometries of the specimens for Nakajima testing. From a) to e) Geometries 1 to 5. 26

Figure 4-1. a) Nakajima samples after testing (1–5, from left to right) and b) computational layout of Nakajima test using ABAQUS software. 29

Figure 5-1. SEM images of the microstructures of the as-received materials. 31

Figure 5-2. EDS elemental maps of banded microstructure present in the as-received alloy 420ma. Point 1 and Point 2 correspond to the analyzed areas inside and outside the band, respectively, and those results are shown in Table 5-1. 32

Figure 5-3. Bright field (BF) and high-angle annular dark field (HAADF) TEM images with corresponding elemental maps of as-received alloy 420ma. 33

Figure 5-4. Typical microstructures of the Q&P-treated samples in the GLEEBLE system. Left: EBSD band contrast map overlaid by retained austenite IPF Z map; Right: KAM map of the corresponding area. 34

Figure 5-5. A fragment of EBSD band contrast map illustrating prior austenite grain (PAG) boundaries, martensite packet boundaries and block boundaries (in the central grain) in the Q&P-treated 420ma alloy. 35

Figure 5-6. Histograms of grain size distribution for retained austenite in the Q&P-treated: a) alloy 410, b) alloy 420, and c) alloy 420ma. 37

Figure 5-7. BF and HAADF TEM images with corresponding elemental maps of the sample 420ma-OQT-450-5. 38

Figure 5-8. Typical microstructures of the large Q&P-treated sheets: a) alloy 410; b) alloy 420; c) alloy 420ma. Left: EBSD band contrast map overlaid by retained austenite IPF map; Right: KAM map of the corresponding area. 44

Figure 5-9. a) Appearance of Fe_3C nanoscale carbides in the Q&P-treated 410 steel; b) appearance of complex (Ti,Nb)C nanocarbides in the large Q&P-treated sheets of 420ma alloy. 45

Figure 5-10. Typical engineering stress – engineering strain curves for the Q&P-treated alloys in the GLEEBLE 3800 system. 47

Figure 5-11. Typical microstructures of the GLEEBLE Q&P-treated samples after tensile testing. Left: EBSD band contrast map overlaid by retained austenite IPF map; Right: KAM map of the corresponding area. 50

Figure 5-12. Histograms of the size distribution of blocky retained austenite (dashed lines) and interlath retained austenite (solid lines) before testing (BT) and after testing (AT) of GLEEBLE Q&P-treated samples: a) 410-OQT-450-5 alloy, b) 420-OQT-450-5 alloy, c) 420-RTQ-450-5 alloy, d) 420ma-OQT-450-5 alloy, e) 420ma-RTQ-450-5 alloy; f) a comparison of total volume fraction (f_γ) and grain size of retained austenite before testing (BT) and after testing (AT) in all studied samples. 53

Figure 5-13. Histograms of the local misorientation distribution before testing (BT) and after testing (AT) of GLEEBLE Q&P-treated samples: a) 410-OQT-450-5 alloy; b) 420-OQT-450-5 alloy; c) 420-RTQ-450-5 alloy; d) 420ma-OQT-450-5 alloy; e) 420ma-RTQ-450-5 alloy. 54

Figure 5-14. The S-N curves obtained from high-cycle fatigue testing of the Q&P-treated large sheets. One sample with fatigue crack initiated at surface rolling defects is marked by a cross (x). 57

Figure 5-15. SEM images of fatigue fracture surface shown by 410 alloy tested with σ_a = 320 MPa (289263 cycles to failure): a) fatigue crack initiation (marked by white arrow) and propagation areas;

b) fatigue crack initiation area shown at higher magnification; c) fatigue crack striations seen on the fatigue crack propagation area. 60

Figure 5-16. SEM image of fatigue fracture surface shown by 420ma alloy tested with σ_a = 300 MPa (62619 cycles to failure): fatigue crack initiation (marked by white arrow) by intergranular cracking (the only case observed in this work). 60

Figure 5-17. SEM images of fatigue fracture surface shown by 420 alloy tested with σ_a = 325 MPa (644000 cycles to failure): a) MnS inclusion debonded from the martensitic matrix in the fatigue crack propagation area, fatigue crack striations are seen; b) local crack propagation in the intergranular mode. 61

Figure 5-18. SEM images of fatigue fracture surface shown by 420ma alloy tested with σ_a = 460 MPa (25804 cycles to failure): a) fatigue crack initiation (marked by white arrow) and propagation areas; b) fatigue crack initiation area shown at higher magnification (fragment of a broken MnS inclusion is seen); c) the outcomes of the EDX analysis performed on the area of fatigue crack initiation confirming the presence of MnS inclusion....61

Figure 5-19. Results of EBSD analysis of the fatigue crack initiation area (left edge): a) map of martensite packets, b) map of martensite variants, c) map of prior austenite grains, d) band contrast map with retained austenite colored in green, e) KAM map. Black lines represent PAG boundaries along with the twin boundaries. 63

Figure 5-20. Results of EBSD analysis of the fatigue crack propagation area (at ~350 μm from the fatigue crack initiation spot): a) map of martensite packets, b) map of martensite variants, c) map of prior austenite grains, d) band contrast map with retained austenite colored in green, e) KAM map. Black lines represent PAG boundaries along with the twin boundaries and the white arrow indicates the secondary crack along a prior austenite grain boundary....64

Figure 5-21. Histograms of the local misorientation distribution of the Q&P-treated 420ma alloy after fatigue testing with stress amplitude σ_a = 460 MPa: a) area of the fatigue crack initiation; b) area of the fatigue crack propagation at the distance of ~ 350 μm from the fatigue crack initiation area. Local misorientations of the tested sample were measured on the subsurface area (≤ 2 μm) from the fatigue fracture surface and the remaining area of the tested sample (bulk)....65

Figure 5-22. Plot showing the critical inclusion sizes for 1045 normalized and quenched and tempered bar steels along with experimentally observed inclusion sizes at the crack nucleation site in the core microstructure of induction-hardened 1045 quenched and tempered steel, from [122]. The red dashed line marks the $\sqrt{area}$ = 2.72 μm inclusion size of the present work.....68

Figure 5-23. Typical appearance of tested Nakajima samples. 70

Figure 5-24. Forming limit diagrams. 70

Figure 5-25. EBSD maps of Nakajima samples from alloy 410: a) undeformed sample, b) geometry 1, c) geometry 3, d) geometry 5. 72

Figure 5-26. EBSD maps of Nakajima samples from alloy 420ma: a) undeformed sample, b) geometry 1, c) geometry 3, d) geometry 5....73

Figure 5-27. Distribution of local misorientation in the martensitic matrix for a) alloy 410 and b) alloy 420ma. 74

Figure 5-28. Nakajima force vs. displacement data comparison between simulated and experimental tests for alloy 410 (a, b), 420 (c, d) and 420ma (e, f). 77

Figure 5-29. Nakajima test comparison for ε_p, showing experimental (a) vs. computational (b) results, with maximum values of 0.29 and 0.343 marked with a white dot, respectively. The data are provided by RINA Consulting – Centro Sviluppo Materiali. 78

Figure 5-30. Comparison of experimental and simulated FLD curves for alloy 410 (a), alloy 420 (b) and alloy 420ma (c). 79

Figure 5-31. FLSD curves calculated for the studied Q&P-treated martensitic stainless steels. 81

Figure 5-32. Actual final shape of the automotive parts whose stamping process is simulated, a) B-pillar and c) tunnel [139]. Corresponding setup of the ABAQUS simulation models for both parts, b) B-pillar and d) tunnel. 82

Figure 5-33. Example of final result of B-pillar stamping simulation, in this case for alloy 410....83

Figure 5-34. Example of final result of tunnel stamping simulation, in this case for alloy 410.....83

Figure 5-35. Example of final result of B-pillar stamping simulation, in this case for alloy 420ma. 84

Figure 5-36. Example of final result of tunnel stamping simulation, in this case for alloy 420ma.84

Figure 6-1. Calculation of total life cycle cost (LCC). 87

Figure 6-2. Simplified flow diagram and carbon emissions of the BF-BOF steelmaking route [145]. 93

Figure 6-3. Simplified flow diagram and carbon emissions of the EAF steelmaking route [145]..93

Figure 6-4. Distribution of CO_2 emissions [146]. 94

TABLE OF TABLES

Table 1-1. Tensile properties and hardness of commercially available martensitic stainless steels..7

Table 1-2. Corrosion resistance properties and uses of selected martensitic stainless steel grades [24]. 8

Table 3-1. Chemical composition of the studied martensitic stainless steels in wt.% (Fe, balance). 15

Table 3-2. Estimated characteristic temperatures and volume fractions of retained austenite for the selected alloys. 16

Table 3-3. Q&P heat treatment applied in the GLEEBLE 3800 system. 19

Table 3-4. QT, PT and Pt parameters studied for the GLEEBLE Q&P treatments. 19

Table 3-5. Optimal Q&P parameters for the heat treatment of the large sheets..... 20

Table 5-1. Alloying element contents (wt. %) inside and outside bands in as-received alloy 420ma measured via EDS. 31

Table 5-2. Local volume fractions of the individual microstructural constituents measured by EBSD. 35

Table 5-3. Size of the individual microstructural constituents measured by EBSD. 36

Table 5-4. Volume fraction of retained austenite measured by XRD and magnetometry, and comparison with the EBSD data. 39

Table 5-5. Lattice parameter of retained austenite in the GLEEBLE Q&P-treated samples. 40

Table 5-6. Results of carbon content determination using different equations. 41

Table 5-7. Microstructural constituents identified using EBSD analysis and their local volume fractions in the large Q&P-treated sheets. 43

Table 5-8. Size of the microstructural constituents in the large Q&P-treated sheets determined using EBSD analysis. 43

Table 5-9. Basic tensile mechanical properties of the GLEEBLE Q&P-treated martensitic stainless steels and their conventional quenched and tempered counterparts. 48

Table 5-10. Volume fraction (V_{total}^{RA}) and grain size (d_{total}^{RA}) of retained austenite before and after tensile deformation of the selected conditions. Data on volume fraction and grain size of blocky retained austenite (V_{blocky}^{RA} and d_{blocky}^{RA}, respectively) and interlath retained austenite (V_{il}^{RA} and d_{il}^{RA}, respectively) are also provided. 52

Table 5-11. Data from tensile testing of the standard samples of the Q&P-treated large sheets. .55

Table 5-12. Data from tensile and fatigue testing of Q&P-treated martensitic stainless steels. 57

Table 5-13. Comparison of the fatigue limit data for martensitic stainless steels. 59

Table 5-14. Local volume fractions of interlath and blocky retained austenite measured on the EBSD maps taken from the areas of the fatigue crack initiation and propagation. 65

Table 5-15 Parameters used to calculate the radius of plastic zone at the tip of the fatigue crack. 67

Table 5-16. Major and minor stresses for each of the tested samples. 70

Table 5-17. Microstructural data from EBSD characterization of samples after Nakajima testing. 74

Table 5-18. Parameters in J-C model used for simulations. 76

Table 6-1. Chemical composition of the analyzed alloys (in wt.%). 88

Table 6-2. Cost of raw materials (€/tonn). 88

Table 6-3. Cost of the raw materials used for making each grade (€/tonn). 89

Table 6-4. Final heat treatments applied to studied grades. 89

Table 6-5. Power of an average beam-walking furnace used in steel processing at different heat treatment temperatures. 90

Table 6-6. Data on the energy spent for the final heat treatment and its cost. 90

Table 6-7. The outcomes of cost analysis (provided that the final Q&P treatment is performed by steelmaker). 91

Table 6-8. The outcomes of cost analysis (provided that the final Q&P treatment is performed by customer-end-user). 92

LIST OF ABBREVIATIONS & SYMBOLS

AC	Acquisition Costs
AHSS	Advanced High Strength Steels
AISI	American Iron and Steel Institute
APT	Atom Probe Tomography
ASTM	American Society for Testing and Materials
AT	After testing
B-RA	Blocky Retained Austenite
BF	Bright Field
BF-BOF	Blast Furnace – Basic Oxygen Furnace
BT	Before testing
CAE	Computer Aided Engineering
DBTT	Ductile – Brittle Transition Temperature
DIC	Digital Image Correlation
EAF	Electric Arc Furnace
EBSD	Electron Backscatter Diffraction
EDS	Energy Dispersive X-Ray Spectroscopy
FEM	Finite Element Method
FLD	Forming Limit Diagram
FLSD	Forming Limit Stress Diagram
FM	Fresh Martensite
GAIQ	Grain Average Image Quality
GNDs	Geometrically Necessary Dislocations
HAADF	High Angle Annular Dark Field
IC	Initial materials fabrication Costs
IL-RA	Interlath Retained Austenite
IPF	Inverse Pole Figure
ISO	International Organization for Standardization
J-C	Johnson-Cook
KAM	Kernel Average Misorientation
K-S	Kurdjumov-Sachs
LCC	Life Cycle Cost
MSS	Martensitic Stainless Steels
ND	Normal Direction
OC	Operating and maintenance Costs

OQT	Optimum Quenching Temperature
PAG	Prior Austenite Grain
PT	Partitioning Temperature
Pt	Partitioning time
Q&P	Quenching and Partitioning
QoI	Quantities of Interest
QT	Quenching Temperature
Qt	Quenching time
RA	Retained Austenite
RC	Replacement materials Costs
RD	Rolling Direction
RTQ	Room Temperature Quench
SEM	Scanning Electron Microscope
TEM	Transmission Electron Microscope
TM	Tempered Martensite
TRIP	Transformation Induced Plasticity
XRD	X-Ray Diffractometry

a	Lattice parameter
A	Initial yield stress
A_{50}	Elongation of sample with gauge length 50 mm
Ac_3	Critical temperature ferrite-austenite
B	Strain hardening coefficient
C	Strain rate coefficient
c_γ	Carbon concentration in austenite
c_i	Initial carbon concentration
c_m	Carbon concentration in martensite
d	Interplanar spacing
d_{blocky}^{RA}	Grain size of blocky retained austenite
d_{il}^{RA}	Grain size of interlath retained austenite
d_{total}^{RA}	Grain size of retained austenite
$\boldsymbol{d\varepsilon_{ij}}$	Tensor of incremental strain
ε_p	Equivalent plastic strain
$\dot{\varepsilon}_p^*$	Plastic strain rate
$\dot{\varepsilon_{p_0}}$	Reference plastic strain rate
ε_{pl}	Local plastic strain
ε_t	Elongation to fracture
$(h\ k\ l)$	Miller Indices
K	Strength coefficient
K_I	Stress intensity factor
ΔK	Stress intensity range
ΔK_{th}	Fatigue crack growth threshold
$d\lambda$	Incremental plastic slip
λ	Wavelength
m	Thermal softening exponent
M_{sat}	Magnetization saturation
M_f	Martensite finish temperature
M_s	Martensite start temperature
n	Strain hardening exponent
R	Stress ratio

r_p	Radius of plastic zone
$\boldsymbol{s_{ij}}$	Tensor of incremental stress
σ	True stress
$\sigma_{0.2}$	Yield strength
σ_a	Stress amplitude
σ_f	Fatigue limit
σ_{max}	Maximum stress applied
σ_{min}	Minimum stress applied
σ_{UTS}	Ultimate tensile strength
σ_y	Yield stress
t_f	Final thickness
t_o	Initial thickness
ν	Poisson ratio
θ	Temperature
θ_*	Equivalent temperature
θ_{exp}	Experiment temperature
θ_{melt}	Melting temperature
θ_{room}	Room temperature
V_{FM}	Volume fraction of fresh martensite
V_{RA}	Volume fraction of retained austenite
V_{blocky}^{RA}	Volume fraction of blocky retained austenite
V_{il}^{RA}	Volume fraction of interlath retained austenite
ω	Incident angle
x_{Fe}	Mass fraction of iron

1. INTRODUCTION

Given the increasing awareness of the effects of human activity on the environment [1], society is asking the industry to carry out better practices. One of the most affected by this change of paradigm is the automotive industry, which contributes to pollutant emissions in both the manufacturing stage and the service stage. Manufacturers have investigated different approaches to reduce carbon emissions, such as lightening the frame structure of the vehicle. This can be achieved via using advanced high strength steels (AHSS) [2]. With this strategy, emissions are reduced in both stages: 1) Less material is required for the frame, less has to be produced; 2) As the vehicle is lighter, less fuel is consumed during its service. The frame of the vehicle fulfills a security function, preventing the occupants of suffering any damage in case of collision by absorbing impact energy and deforming in a controlled manner. Thus, the material chosen to lighten the structure has to meet the high requirements to its mechanical properties.

Stainless steel offers a compromise between light-weighting, mechanical and functional properties to suit the aforementioned application. A shortcoming is the high cost of the traditionally used alloys that fulfill the requirements for the application. Austenitic stainless steels contain high amounts of chromium and nickel, alloying elements that increase the cost, especially the latter. Martensitic stainless steel is another grade inside this family that does not require nickel in its composition. Hence, the price of the alloy is lower than of an austenitic one; although mechanical properties and corrosion resistance are not as good.

The mechanical properties of certain martensitic stainless steels can be enhanced using a relatively new heat treatment called quenching and partitioning (Q&P) [3]. This heat treatment has been applied to carbon steels with successful results, generating a family named 'Q&P steels'. Q&P steels belong to the Third Generation AHSS, whose mechanical properties put this generation between the First and the Second Generations, as shown in Figure 1-1. Q&P martensitic stainless steels aim to achieve a similar combination of mechanical properties.

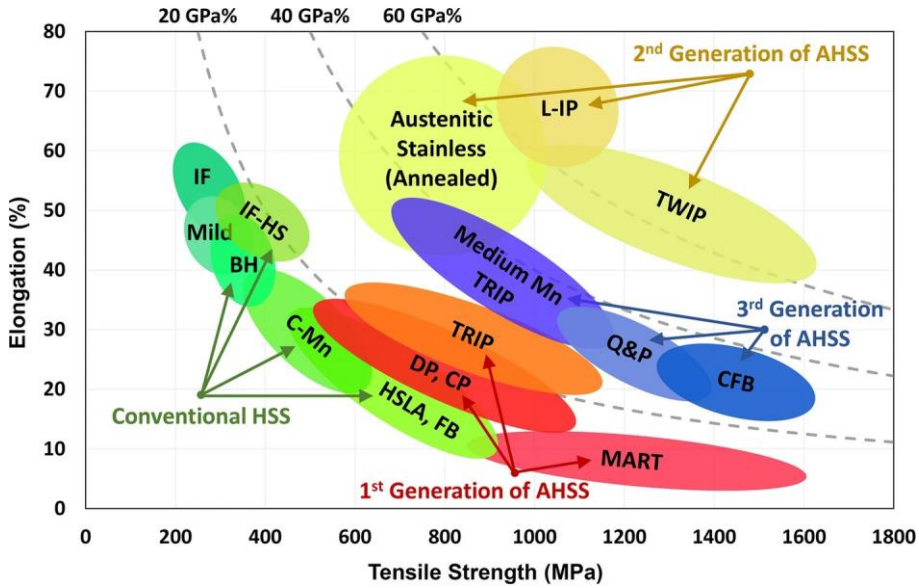

Figure 1-1. Ashby plot, elongation vs ultimate tensile strength for different generations of AHSS [4].

1.1. Stainless Steels

Stainless steels are a class of iron-carbon alloys distinguished by their elevated chromium content, typically exceeding 10.5% by weight. This distinctive chromium composition is the key to the corrosion resistance for which stainless steels are renowned [5]–[8]. The significant chromium presence facilitates the development of a thin but robust chromium oxide layer on the surface of the steel. This passive layer serves a dual role: it shields and isolates the underlying substrate from the surrounding environment and exhibits a remarkable ability to self-repair in the face of damage, preserving an aesthetically appealing appearance over time.

The corrosion-resistant attributes of stainless steels are further augmented through the incorporation of various alloying elements, including nickel, molybdenum, titanium, and others [8]. These additional elements enhance the corrosion resistance of the protective layer, rendering stainless steels suitable for a wide array of environments, including those characterized by increased aggressiveness. Moreover, these alloying elements confer unique properties to stainless steels, broadening their utility beyond mere corrosion resistance.

1.1.1. Classification

Within the stainless steel family, various subtypes can be found, classified based on the microstructure they exhibit at room temperature. The Schaeffler Diagram (Figure 1-2) offers a straightforward visualization of the relationship between equivalent chromium and nickel content ((Eq. 1.1) and (Eq. 1.2), respectively) and the anticipated microstructure [9].

$$\%Cr_{eq} = \%Cr + 2 \cdot \%Si + 1.5 \cdot \%Mo + 5.5 \cdot \%Al + 1.75 \cdot \%Nb + 1.5 \cdot \%Ti \qquad \textit{(Eq. 1.1)}$$

$$\%Ni_{eq} = \%Ni + 30 \cdot \%C + 0.5 \cdot \%Mn + 25 \cdot \%N \qquad \textit{(Eq. 1.2)}$$

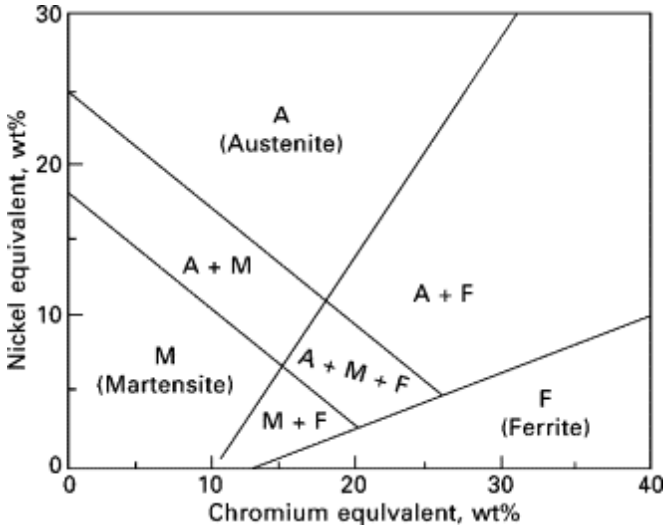

Figure 1-2. Schaeffler diagram for stainless steels classification [9].

The Schaeffler Diagram accounts for three primary types: austenitic, ferritic, and martensitic steels. In addition, the literature commonly recognizes two more major types: duplex and precipitation hardening steels. Below, some brief notes on each of these types are listed:

- **Austenitic stainless steel.** Despite its higher production cost due to the significant nickel content required to stabilize the austenitic microstructure, it is among the most widely used varieties. Known for its exceptional corrosion resistance, weldability, and formability, austenitic stainless steels find applications across a broad spectrum, from cryogenic temperatures to the demanding environments of jet engines and furnaces.
- **Ferritic stainless steel.** This category of stainless steels provides excellent corrosion and oxidation resistance at relatively low cost. However, these alloys are prone to coarsening of the ferritic grains, impacting significantly their toughness. This factor explains the reluctance to use them widely, but there are numerous applications where ferritic stainless steels can effectively substitute for austenitic stainless steels. Ferritic stainless steel is mainly used in manufacturing automotive parts, industrial machinery and kitchenware.
- **Martensitic stainless steel.** While its corrosion resistance may be lower than that of other categories, it still surpasses that of carbon steels. The lower alloying element content required for the martensitic microstructure results in a cost advantage compared to other alloys. This group possesses high-strength, hardness and toughness – characteristics that render martensitic stainless steels valuable for various applications, including pump and valve parts, bearings, propeller shafts and medical devices and tools.
- **Duplex stainless steel.** This group features a microstructure composed of ferrite and austenite. The mechanical properties and corrosion resistance of these alloys depend on the ratio of ferrite to austenite. Generally, they exhibit outstanding corrosion resistance in strongly acidic environments and possess mechanical properties that exceed those of both austenitic and ferritic stainless steels, although they do not quite reach the level of martensitic stainless steels. However, their formability is relatively low due to the differing plasticity of the two phases. This steel found a wide application in chemical processing, transport and storage, as well as marine and other high chloride environments.
- **Precipitation-hardening stainless steel.** This category of stainless steels is distinguished by its unique ability to precipitate coherent inclusions, significantly enhancing strength without compromising corrosion resistance. These materials rely on the low stability of the austenite, which undergoes near-total transformation into martensite, further hardenable through the precipitation of coherent inclusions. What sets these steels apart from conventional martensitic stainless steels is their superior combination of strength, toughness, and corrosion resistance achieved through precipitation, surpassing the hardening achieved through carbon. This led to their wide use in aerospace and marine components, fuel tanks, pump parts and landing gear covers.

After briefly reviewing the major types of stainless steels, it becomes evident that martensitic stainless steels (MSS) possess the potential to meet the requirements for quenching and partitioning heat treatments without compromising the martensitic microstructure. In the Schaeffler Diagram (Figure 1-2), we observe that the least alloyed grades of stainless steel fall under the classification of martensitic stainless steel. This steel family, first commercialized by Brearley in 1913 [10], traces its origins to grade 410. Subsequent grades were developed by introducing various alloying elements. For example, increasing nickel content results in grade 414, while elevating the carbon content yields grade 420. These steels find widespread use in diverse applications, including knife-making, surgical equipment, valves, and springs [11]. In the automotive industry, they have primarily been employed in exhaust systems.

1.1.2. Processing of standard martensitic stainless steel

The thermal processing of standard martensitic stainless steel requires careful control to achieve the desired mechanical and structural properties. These treatments play a pivotal role in tailoring the microstructure and enhancing the performance of martensitic stainless steel for various applications.

Austenitization is typically the initial heat treatment applied in the case of martensitic stainless steels, and it plays a crucial role in defining the final microstructure. During this process, the austenitizing temperature directly influences the grain size of the prior austenite, which, in turn, affects several critical factors. The prior austenite grain size has a notable impact on the martensite start temperature (M_s), but more significantly, it influences the material's toughness. At around 475 °C, phosphorus precipitates along the prior austenite boundaries, a phenomenon infamously known as temper embrittlement. An increase in the austenitizing temperature leads to a larger austenite grain size, allowing for greater phosphorus concentration at the boundaries. This results in a decrease in the toughness of the steel. The control of temper embrittlement hinges on the management of austenite size, as achieving low phosphorus levels in the alloys can be a challenging and expensive process.

The austenitizing temperature controls the dissolution of carbon and carbides in the austenite phase. Many martensitic stainless steel grades are deliberately alloyed with specific carbon contents to enable the precipitation of carbides, serving various objectives. Precise control of this temperature is essential to effectively dissolve undesired carbides while retaining the beneficial ones (if present). Additionally, the carbon dissolved in the austenite significantly impacts ferrite content, M_s, and certain mechanical properties. Furthermore, it is crucial to account for surface decarburization during austenitization, a phenomenon that intensifies with higher austenitizing temperatures and base carbon content. This surface decarburization can result in a superficial softening of the material. Careful attention to the protective atmosphere within the furnace is necessary to prevent such effects, including not only surface decarburization but also potential nitrogen or carbon enrichment or susceptibility to hydrogen embrittlement [12].

Following austenitization, the steel must undergo quenching, with the air quenching method often preferred to prevent cracking and excessive warpage. During quenching, the austenite → martensite transformation occurs, leading to the development of residual stresses in the inherently brittle material. As a result, a subsequent heat treatment is necessary to alleviate these stresses.

For the tempering stage, the temperature range 475 – 550 °C is avoided because temper embrittlement occurs within this range. Below this temperature range, heating as-quenched material between 150 – 400 °C leads to stress-relieving and a minor precipitation of fine cementite particles. This precipitation slightly decreases the C content in martensite, resulting in a slight decrease in the hardness. At higher temperatures (400 – 475 °C) further carbides precipitate, which can result in a secondary hardening (precipitation-hardening effect) [12].

True tempering is conducted above 550 °C, a temperature at which the temper embrittlement effect begins to disappear. At these temperatures, tempering effects include sought-after stress relief, carbide precipitation, coarsening, and the loss of carbon from the solid solution. In cases where retained austenite is present in the microstructure, it decomposes into ferrite and carbides, negatively affecting toughness. Higher-chromium grades typically undergo stress relief only,

as removing chromium from the solid solution to form carbides would result in an unacceptable loss of corrosion resistance.

1.1.3. Typical microstructures of martensitic stainless steels

The microstructure of martensitic stainless steels is primarily martensitic in nature, with some minor secondary phases resulting from the austenitization process and typical inclusions found in various steel types. Notably, the martensite in martensitic stainless steels exhibits a lath morphology rather than a plate-like structure. In Figure 1-3 a typical microstructure of these steels is displayed.

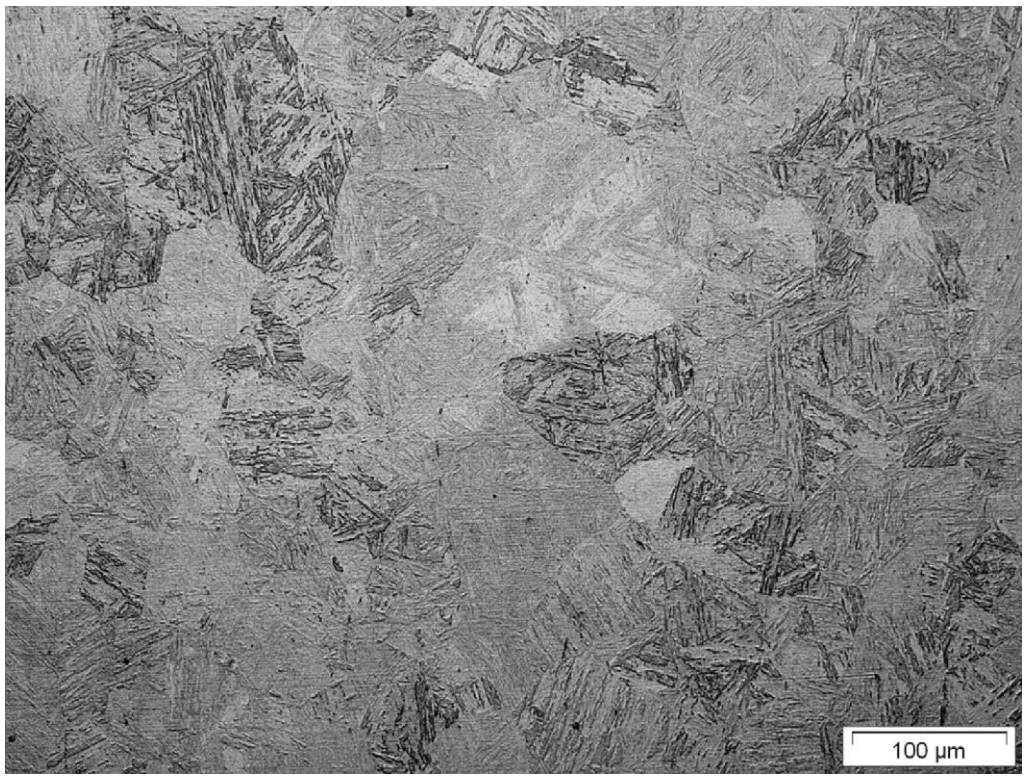

Figure 1-3. Typical microstructure of AISI 410 stainless steel, Vilella's etching [13].

The ferromagnetic martensite in steels usually has a body centered tetragonal (BCT) structure but in case of stainless steels due to the relatively low content of interstitials, the martensite is often referred to as BCC rather than BCT.

During the transformation from austenite to martensite, the martensite laths inherit the orientation of their parent austenite grain. In the case of low-carbon steels, the Kurdjumov–Sachs (K-S) relationship defines 24 equivalent crystallographic variants in the martensite phase originating from a single austenite grain [14]–[16]. Martensite laths sharing the same crystallographic orientation, or variant, form a martensite block. In Figure 1-3, the blocks can be seen in different shades of grey, depending on the strength of Vilella's etching on a specific crystallographic orientation. The martensite packet is a collection of martensite blocks that share the same habit plane in the austenite [15].

This hierarchy of martensite structures is visually depicted in Figure 1-4. The characteristics of lath martensite, including its morphology and crystallography, are of paramount importance

since they have a direct impact on the strength and toughness of martensitic steels [17]. The sizes of packets and blocks, essentially effective grain sizes within the lath martensite structure, play a critical role in determining the mechanical properties of martensitic stainless steels.

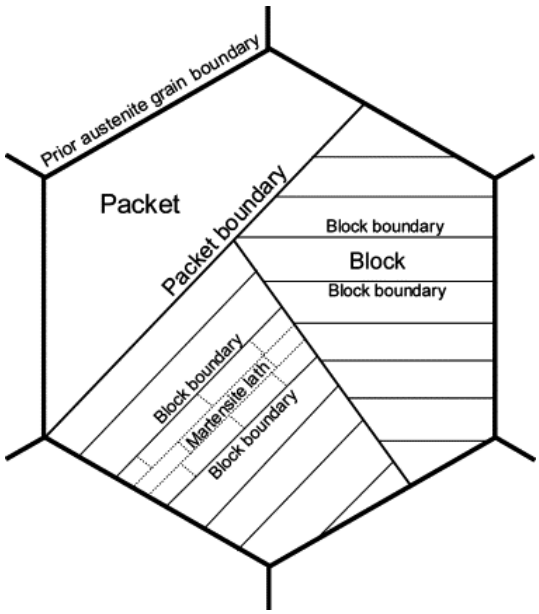

Figure 1-4. Hierarchical structure of martensite [15].

1.1.4. Properties of martensitic stainless steel

In this section a general overview of the diverse properties of martensitic stainless steels is given, ranging from mechanical strength and hardness to corrosion resistance.

1.1.4.1. Mechanical properties

As previously mentioned, the mechanical properties of these steels greatly depend on the chemical compositions and heat treatment cycle applied. The characteristic high strength of martensitic stainless steels is achieved in a quenched and tempered state. A martensitic grade can have an ultimate tensile strength above 1000 MPa and an elongation to fracture below 10 % [18]. The hardness depends as well on the heat treatment, achieving from 9 HRC in annealed states to 40 – 60 HRC in the quenched and tempered condition. In Table 1-1 mechanical properties for some grades of martensitic stainless steels are reported. The fatigue and fracture resistance of martensitic stainless steels is similar to low-alloy martensitic steels with comparable strength and hardness [19].

Martensitic stainless steels present unique challenges in forming processes due to their high yield strength and relatively low ductility. These properties can limit their versatility in shaping applications. At room temperature, the primary method employed for shaping these steels is roll forming. However, it's important to note that this technique has inherent limitations when it comes to achieving intricate and highly complex shapes [20].

Type 410 and 420 are prized for their corrosion resistance coupled with remarkable strength, boasting yield strength values surpassing the 1000 MPa mark, yet they do exhibit some

limitations in terms of toughness. Notably, these grades manage to retain their tensile properties even when exposed to elevated temperatures. At 600 °C, they maintain approximately 45% of their strength observed at room temperature. Thanks to their high levels of hardness, they also exhibit excellent resistance to abrasion and cavitation, making them highly sought after for applications demanding these particular attributes [21].

Table 1-1. Tensile properties and hardness of commercially available martensitic stainless steels.

Designation ASTM	State	Tensile properties			Hardness [HRB]	Ref.
		$\sigma_{0.2}$ [MPa]	σ_{UTS} [MPa]	Elongation A_{50} [%]		
410	A	300	560	30	-	[18]
416	A	350	550	20	-	
420	A	500	650	20	-	
420	A	375	660	24	89	
403,410	A	275	480	20	-	[22]
403,410	T	550	690	12	-	
403,410	H	620	830	12	-	
410	H	1030	1360	8.5	-	[23]

A = annealed state
T = Hardened and tempered at a relatively low temperature
H = Hardened and tempered at a relatively high temperature

1.1.4.2. Application-related properties

The corrosion resistance of martensitic stainless steel is lower compared to highly alloyed austenitic and duplex stainless steels. However, martensitic stainless steels still present an optimal corrosion resistance in a limited range of media, including food industry and surgical equipment. This corrosion resistance is superior against hot oils and wet carbon dioxide [21]. Table 1-2 summarizes the corrosion resistance of the main martensitic stainless steel grades and their typical applications [24].

In terms of the weldability of martensitic stainless steels, their typical higher carbon content compared to other stainless steels makes them slightly more challenging to weld. The welded region and the heat affected zone are sensitive to cracking due to the residual tensions generated from the martensitic transformation and its associated volume change. Additionally, the presence of hydrogen during the welding process can accentuate the crack apparition due to hydrogen induced cracking. Following certain precautions these issues can be avoided. Preheating and/or post-weld heat treatments are usually applied to martensitic stainless steels, in combination with low hydrogen welding processes [25].

Table 1-2. Corrosion resistance properties and uses of selected martensitic stainless steel grades [24].

Designation ASTM	Description	Uses
410	Resistant in dry atmospheres, fresh water, mild alkalis and acids. Suitable for steam and other hot gases. Better heat and corrosion resistance in the hardened state.	Fasteners, pump parts and shafts, turbine parts, cutlery, rulers.
420	Higher carbon content than 410. Good resistance at atmospheric conditions in the hardened state.	Cutlery, surgical equipment, needle valves.
431	Corrosion resistance comparable to grade 304, excellent to a wide variety of corrosive media.	Pump and boat shafts, nuts, bolts, marine hardware.
440	Superior strength and hardness in this high-carbon grade. Moderate corrosion resistance.	Knives, ball bearings, gauge blocks, dies.

1.2. Quenching and partitioning as a promising method for martensitic stainless steels

1.2.1. Concept of quenching and partitioning (Q&P)

The "quenching and partitioning" (Q&P) heat treatment was first proposed in 2003 as a novel tool for the microstructural design in carbon steels [26]. This process is based on quenching austenite to an intermediate temperature between the martensite start (M_s) and martensite finish (M_f) followed by a partitioning treatment at quenching temperature or above to enrich the remaining austenite with carbon, thereby stabilizing it to room temperature (Figure 1-5). The presence of retained austenite in the final microstructure enables the transformation induced plasticity (TRIP) effect, which increases the strain hardening ability and ductility due to the austenite → martensite transformation during plastic deformation [27]. Hence, a better balance of high strength and sufficient ductility is obtained compared with a typical quenching and tempering heat treatment [28]–[31].

The steels processed using this heat treatment have been referred to as "Q&P steels". They belong to the third generation of AHSS. The chemical composition of the Q&P steels is designed to enable the stabilization of austenite via carbon partitioning. Alloying elements that prevent carbide precipitation, such as silicon, are expressly introduced to facilitate the partitioning process. Thus, the alloying requirements for this heat treatment are quite lenient, making this heat treatment potentially applicable to a wide range of alloys.

In Figure 1-5 a schematic representation of the Q&P heat treatment routes is shown. This heat treatment starts from a complete austenitization of the steel (by heating above Ac_3), followed by quench to a selected temperature that determines the martensite and austenite fractions, and ends with a partitioning step to stabilize the remaining austenite to room temperature. The selected temperature for the partitioning step can be either the same

temperature as the quenching temperature, resulting in a one-step Q&P; or a temperature slightly above it, resulting in a two-step Q&P.

As mentioned, the partitioning step has the objective of stabilizing the austenite, so it can be retained at room temperature, as opposed to a usual tempering process. At the partitioning temperature, the diffusion of carbon from martensite to austenite is favored causing the martensite to desaturate its carbon content in a process "equivalent" to tempering. Carbide precipitation is inhibited by silicon and aluminum; thus, carbon stabilizes the gamma-field, making retained austenite present at room temperature.

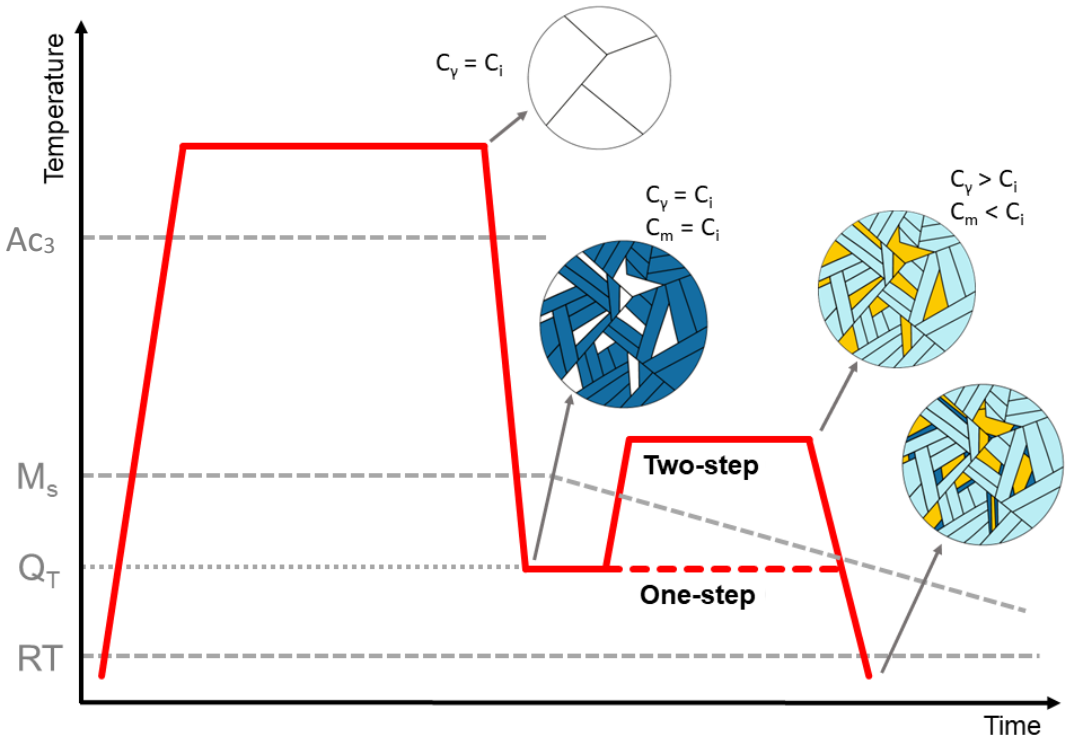

Figure 1-5. A schematic presentation of the Q&P heat treatment, where Ac_3 indicates the temperature above which only austenite is present in the microstructure, M_S martensite start temperature, QT quenching temperature and RT room temperature. C_i, C_γ and C_m represent initial carbon concentration in austenite, carbon concentration in retained austenite and carbon concentration in martensite, respectively. Color code: austenite in white, retained austenite in yellow, fresh martensite in dark blue and tempered martensite in light blue. Adapted graph from [32].

1.2.2. Microstructure and properties achieved in carbon steels via Q&P

Carbon steels have been thoroughly investigated as Q&P steels, proven by the extensive bibliography [28]–[31]. The main outcomes of these studies can be roughly summarized as follows. The ultimate tensile strength of the Q&P-treated carbon steels reported in the literature was from ~1000 MPa to ~2000 MPa, with elongation to fracture ranging from ~5 to ~25 %

[28]. Both strength and ductility were strongly dependent on the microstructure, which was determined by steel chemical composition and applied Q&P parameters.

The Q&P processing can lead to microstructures of tempered martensite with a high volume fraction of retained austenite [28]–[31]. Its content, morphology and mechanical stability play a key role in determining the mechanical behavior and properties of Q&P steels. Mechanical stability of retained austenite is determined by various factors including carbon content, size and its crystallographic orientation [33]. Gradual austenite-martensite phase transformation is required during plastic deformation to achieve the enhanced strain hardening ability, tensile ductility and ultimate tensile strength [27]. This can be done via intelligent microstructural design by inducing austenite grains with varying transformation potential.

The performance of steels in automotive applications is not solely determined by its mechanical strength and tensile ductility. Improved mechanical properties must be coupled with satisfactory application-related characteristics, which have also gathered attention from the research community. There are studies showing promising formability [34], impact resistance [35], fracture resistance [36], fatigue performance [37] and resistance to hydrogen embrittlement [38]. It should also be noted that special industrial lines were designed by Baosteel [39] and AK Steel [40], where Q&P process can be easily implemented. A component B-pillar was manufactured successfully using Q&P1000 steel at Baosteel [39].

1.2.3. Current development of Q&P process for manufacturing martensitic stainless steel

The application of Q&P heat treatment to martensitic stainless steels is still a relatively unexplored field, as demonstrated by the limited bibliography published [41]–[46]. These studies have clearly shown that Q&P processing of 13Cr type martensitic stainless steel is feasible,

1.2.3.1. Microstructure in martensitic stainless steel via Q&P

The Q&P process was successfully applied to the 410 [43], [44] and 420 [42], [45], [47], [48] martensitic stainless steels. This heat treatment has resulted in typical Q&P microstructures characterized by high volume fractions of retained austenite (up to 50 %) embedded into tempered martensite matrix, exhibiting high mechanical properties [41]–[44]. Similar to carbon steels, alloying martensitic stainless steels with silicon serves to inhibit the precipitation of cementite. This strategic alloying ensures that carbon remains available to stabilize the austenite phase during partitioning step, resulting in higher fractions of retained austenite (RA) and consequently, improved ductility [43]. However, it should also be noted that the high content of silicon is not necessarily required to retard the formation of carbides during the tempering in martensitic stainless steels with high chromium content, especially during short partitioning times [43].

It has been demonstrated that with sufficient alloying [41] (13.6wt.%Cr, 0.44wt.%C), the Q&P process can be applied through room temperature quenching. In this case, austenite reversion occurs during partitioning process (the austenite fraction increases due to carbon enrichment at grain and phase boundaries). This finding is highly relevant to industry and of great practical interest.

1.2.3.2. Properties reached in Q&P-treated martensitic stainless steels

The achieved mechanical properties in Q&P-treated martensitic stainless steels exhibit a wide range, with ultimate tensile strengths (UTS) ranging from 1200 MPa in low-carbon alloys to an impressive 2000 MPa in high-carbon alloys [41]–[44]. Moreover, ductility is notably enhanced following Q&P treatment in comparison to standard quenching and tempering processes. For instance, in one study [43], ductility saw a significant improvement of 5 % in the Q&P-treated 410 grade compared to their quenched and tempered counterparts due to TRIP effect by retained austenite.

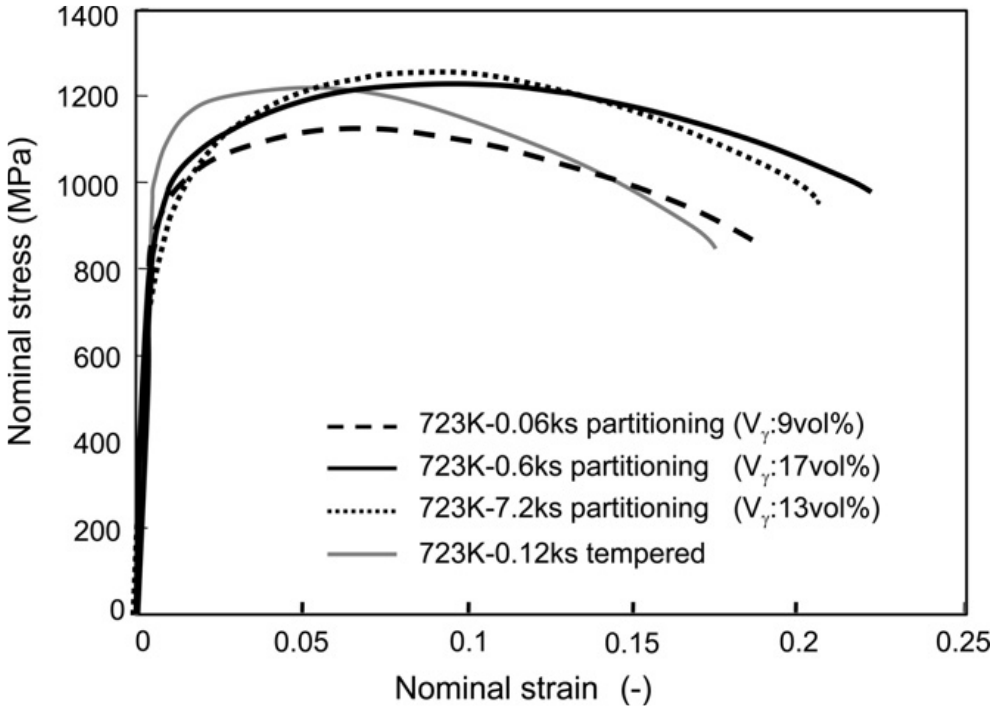

Figure 1-6. Engineering stress–strain curves of Q&P-treated 410 grade (partitioning at 723 K) and quench-and-tempered (Q&T) specimen (tempered at 723 K – for 0.12 ks) with the same tensile strength [43].

Notably, local corrosion resistance exhibits improvement in Q&P-processed steel compared to conventional quenching and tempering methods. This enhancement can be attributed to the presence of retained austenite and reduced chromium precipitation [45], rendering Q&P an attractive option for making parts for corrosion-sensitive applications.

2. MOTIVATION & OBJECTIVES

From the state of the art, it is clearly evident that, for carbon steels, the general trends of Q&P processing are well understood. This includes the role of alloying and Q&P heat treatment parameters, as well as microstructure – property relationships. Moreover, properties relevant to automotive applications have also received attention. However, in the case of martensitic stainless steels, there is a limited number of publications regarding Q&P processing. These scarce studies indicate that Q&P processing can lead to attractive strength-ductility combinations. Furthermore, the possibility of using a modified route with quenching to room temperature was demonstrated for high carbon chemistry [42], primarily focusing on basic mechanical properties. Hence, there exists ample opportunity for further research. First, the effect of alloy composition and Q&P heat treatment parameters on the microstructure should be thoroughly studied including also the room temperature quenching route considering industrial processing windows. The current literature only covers commercially available martensitic stainless steels with little attention paid to alloy design [44]. Second, application-related properties critical for the automotive sector, such as fatigue and formability, should be explored. Finally, the relationships between alloy, composition, the Q&P process, microstructure and properties have not been studied in depth. As a result, research on Q&P-treated martensitic stainless steels is in its infancy, and comprehensive studies are needed to understand the alloy – process – microstructure – property relationships in these promising materials.

The main goal of this work was to study the effect of chemical composition and Q&P heat treatment parameters on the microstructure and tensile deformation behavior, as well as to explore critical application-related properties for Q&P-treated martensitic stainless steels. The knowledge gained from this research will enable the optimization of alloy chemistry and Q&P processes for microstructural design in martensitic stainless steels to improve their mechanical properties and overall performance. The following specific objectives have been defined:

1) To investigate the effect of chemistry and Q&P treatment parameters on the microstructure and tensile deformation behavior of three martensitic stainless steels.

2) To explore the high-cycle fatigue behavior of Q&P-treated martensitic stainless steels and study the effect of the complex hierarchical microstructure on fatigue crack formation and growth.

3) To develop a computational approach moderately based on experimental data, which will allow us to assess the feasibility of cold forming automotive parts from Q&P-treated martensitic stainless steels.

4) To conduct a life cycle cost analysis of Q&P-treated martensitic stainless steels, comparing them to standard stainless steels, as well as to analyze the environmental effect of implementing Q&P treatment in the industrial process.

3. MATERIALS & EXPERIMENTAL PROCEDURES

In this section, the three steels used in the present thesis are introduced, and the rationale behind their selection is provided. The corresponding designed heat treatments are explained, which were implemented using two different approaches: a thermo-mechanical simulator and standard industrial equipment. The experimental methods and techniques employed to characterize the resulting samples are described.

3.1. Materials

Considering the intended final applications of the Q&P-treated martensitic stainless steels for the automotive industry, the following constraints have been taken into account for the material selection:

- **Low alloying cost.** Expensive alloying elements (such as Ni or Mo) should be minimized, in favor of lean martensitic stainless steel compositions (13 wt.% Cr).
- **Weldability.** The C content should be limited (C $\lesssim$ 0.3 wt.%) to control the hardness of the resulting weld and avoid the need of post-weld heat treatments.
- **Industrial production.** Consider the limitations for industrial implementation of the steel grade with its corresponding heat treatment.

Under these constraints, three martensitic stainless steel grades are selected for this work, and their chemical compositions are collected in Table 3-1.

Table 3-1. Chemical composition of the studied martensitic stainless steels in wt.% (Fe, balance).

Alloy	C	Cr	Mn	Si	Ni	Al	N	Nb	Ti
410	0.2	12.5	0.7	0.35	0.2	0.01	0.03	-	-
420	0.3	13.0	0.7	0.35	0.2	0.01	0.03	-	-
420ma	0.3	13.0	3.0	0.35	0.2	0.01	0.03	0.05	0.05

The first alloy has a chemical composition similar to that of an AISI 410 grade (hereafter referred to as 410 alloy). The second alloy has increased carbon content for higher strength and austenite stabilization (hereafter referred to as 420, due to its similarity with AISI 420). Slightly higher Cr contents are considered when the C content is increased to retain the steel's high corrosion resistance [49]. The third alloy has a similar composition as the second, but with increased Mn content (up to 3 wt. %) and the addition of Nb and Ti as microalloying elements (hereafter referred to as 420ma). This addition of Mn leads to a notable increase in austenite stability to a level in which significant fractions can already be present at room temperature after quenching. The addition of Ti and Nb is expected to promote the refinement of the prior austenite grains, leading to a general grain refinement in the final microstructure [50]. Finer austenite grains lead to a more efficient carbon partitioning process from martensite to austenite and facilitates carbon homogenization in the interior of the austenite grains [51]. The addition of Si in the presence of high Cr contents inhibits the precipitation of undesired carbides during the partitioning temperatures range [43].

To assess the suitability of the selected steels, relevant characteristic temperatures are calculated. The first of them is the martensite start temperature (M_s) which indicates the temperature where the martensitic transformation starts. The modified Andrews equation proposed by Kung and Rayment [52] is used to predict this value using the wt.% of some of the alloying elements present (Eq. 3.1). The results of this calculation are collected in Table 3-2.

$$M_s = 553.7 - 530.8 \cdot \%C - 9.7 \cdot \%Si - 12.1 \cdot \%Cr - 30.4 \cdot \%Mn \quad \textit{(Eq. 3.1)}$$

With the M_s temperature, it is possible to apply the model proposed by Speer et al. [3] to calculate the optimum quenching temperature (OQT) for each of the alloys (see Section 1.2.1). The estimated OQT is then improved by a dilatometry test campaign performed by project partners at TU Delft. The improved OQT for each alloy is provided in Table 3-2, along with the estimated maximum volume fraction of retained austenite (V_{RA}) achieved by this quenching temperature. This estimation is based on the carbon balance.

To assess the feasibility of the room temperature quench (RTQ) for these alloys, the martensite finish temperature M_f is roughly estimated using (Eq. 3.2), based on the results reported in previous works [41], [49], [53]. As indicated in Section 1.2.1, the quenching temperature has to be above the M_f temperature. The results of this equation and the suitability of the room temperature quench for these alloys are collected in Table 3-2.

$$M_f = M_s - 200 \quad \textit{(Eq. 3.2)}$$

Another estimated temperature is the critical temperature Ac_3 which indicates the temperature above which austenite is the only phase. In the case of alloy 420ma, TiC and NbC nanoparticles are still present above Ac_3, until their dissolution temperature (between 1100 – 1250 °C) [54]. The model proposed by Capdevila et al. [55] is chosen for the calculation (Eq. 3.3). The resulting temperatures are shown in Table 3-2.

$$\begin{aligned} Ac_3 = 922 - 233 \cdot C^{0.5} + 67.5 \cdot C^2 - 5.7 \cdot Cr + 64.7 \cdot Si - 14.3 \\ \cdot Mn + 30.2 \cdot Cr \cdot C - 65.7 \cdot Si \cdot Mn + 32.7 \cdot Mn \cdot C \\ + 1.3 \cdot Cr^2 + 4.1 \cdot Si^2 - 8.4 \cdot Mn^2 \end{aligned} \quad \textit{(Eq. 3.3)}$$

Table 3-2. Estimated characteristic temperatures and volume fractions of retained austenite for the selected alloys.

Alloy	Ac_3	M_s	M_f	OQT	V_{RA}	Suitable for RTQ?
410	952 °C	272 °C	72 °C	160 °C	30 %	NO
420	1012 °C	212 °C	12 °C	99 °C	36 %	BARELY
420ma	1016 °C	143 °C	-57 °C	62 °C	57 %	YES

From the results reported in Table 3-2, the following observations can be outlined:

- All the alloys are expected to achieve the required Q&P microstructure after a standard Q&P treatment, as demonstrated by the high V_{RA} estimated using the model.
- The expected V_{RA} fractions are considered sufficient for the enhanced mechanical properties, based on the results reported for carbon steels (see Section 1.2.2) and martensitic stainless steels (see Section 1.2.3) in the literature.
- Alloy 410 is not suitable for room temperature quench, as its M_f temperature (72 °C) is above room temperature (20 °C). Alloy 420 is barely suitable, as its M_f is 12 °C; meaning that the remaining volume fraction of austenite after room temperature quenching is very low. Alloy 420ma is totally suitable for room temperature quenching ($M_f = -57$ °C).
- The temperature required for the full austenitization of the studied steels has to be above 1020 °C, and for alloy 420ma it should not greatly exceed 1100 °C.

3.2. Q&P treatment

Two processing routes were used in the development of this work. Initially, the thermo-mechanical simulator GLEEBLE 3800 was employed to evaluate the effect of varying Q&P parameters on the microstructure and basic mechanical properties. Once the optimum Q&P parameters were chosen, the Q&P treatment was applied to large sheets of the selected alloys using standard industrial equipment.

3.2.1. Physical simulation of the Q&P process, using GLEEBLE 3800 system

3.2.1.1. The GLEEBLE 3800 system

The GLEEBLE 3800 system is the thermo-mechanical simulator used in this work. The heating process in the GLEEBLE is produced by the passing of electrical current through the sample, resulting in the Joule effect. The refined control of the power supplied to the system allows a precise control over the temperature reached by the sample. The physics behind the Joule effect define the requirements for the sample: conductive thin specimens with uniform sections, to minimize thermal gradients and prevent the skin effect. A water heat exchanger provides the cooling to the system during heat treatment, and additionally a quenching system can be mounted to increase further the cooling rates.

The samples used for Q&P heat treatments were machined from hot-rolled thick plates along their rolling direction, and their dimensions are outlined in Figure 3-1b. In Figure 3-1a, the experimental set-up in the GLEEBLE chamber is shown, with the following numbered parts: 1) copper grips for electrical contact; 2) sample fixed with the copper grips; 3) a K-type thermocouple welded on the midsection, providing temperature readings to the control program; and 4) quenching system, using two perforated tubes expelling a cooling fluid (compressed air in this case) over the sample. A schematic depiction of the heat-treated region is shown in Figure 3-1b, while Figure 3-1c illustrates the machining of sub-size tensile samples from the GLEEBLE Q&P-treated coupons.

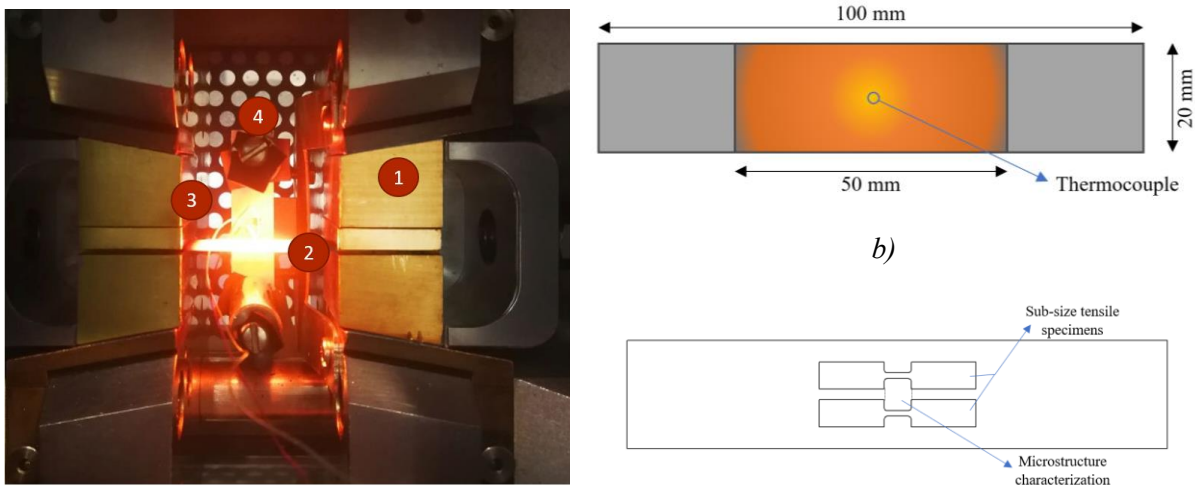

Figure 3-1. Q&P treatment in the GLEEBLE 3800 system: a) experimental set-up for sample treatment in the GLEEBLE chamber, b) geometry of specimen for Q&P treatment in the GLEEBLE chamber, and c) subsequent machining of the sub-size tensile samples from the GLEEBLE Q&P-treated coupons.

3.2.1.2. Q&P parameters screened using the GLEEBLE 3800 system

Taking into account the relevant temperatures for the selected steels (Table 3-2, Section 3.1), the parameters for the austenitization, quenching, and partitioning stages are selected. These Q&P parameters are listed in Table 3-3. The selected austenitization temperature (1100 °C) ensures a full austenitization for all the alloys (their transformation temperatures A_{c3} are < 1100 °C) at the time of 15 min. As it is proven in Section 5.1, these austenitization conditions allow the full dissolution of undesired carbides, while in the case of alloy 420ma, maintaining the desired TiC and NbC nanocarbides.

The quenching and partitioning parameters are defined for each condition of each alloy in Table 3-4. For alloys 420 and 420ma, two quenching temperatures (QT) are explored: the optimal quenching temperature (OQT) as reported in Section 3.1, and the room temperature quench (RTQ), since both alloys allow it, and it is advantageous for the industrial implementation. To reach the room temperature at the minimum cooling rate of 5 °C/s, the quenching system of the GLEEBLE has to be activated as the heat flux through copper grips is not sufficient for providing high cooling rates at temperatures under 200 °C. Hence, upon reaching 200 °C during cooling, the quenching system is activated to maintain the cooling rate until the sample reaches room temperature. It is important to note that the minimum quenching temperature achievable with the described set-up is 30 °C, which is considered as the room temperature in this context. Alloy 410 cannot be quenched at room temperature, so in its case, the effect of partitioning conditions is explored, varying the partitioning temperature (PT) between 400 °C and 450 °C, and the partitioning time (Pt) between 2 min and 5 min. Hereafter, all Q&P processed samples will be designated as 'alloy-QT-PT-Pt'.

Table 3-3. Q&P heat treatment applied in the GLEEBLE 3800 system.

Initial heating rate	Austenitization	Cooling rate to QT	Soaking at QT	Heating rate to PT	Partitioning	Final cooling rate to RT
10 °C/s	1100 °C for 15 min	5 °C/s	QT for 20 s	10 °C/s	PT for Pt	5 °C/s

Table 3-4. QT, PT and Pt parameters studied for the GLEEBLE Q&P treatments.

Sample	Quenching temperature (QT)	Partitioning temperature (PT)	Partitioning time (Pt)
410-OQT-400-5	160 °C	400 °C	5 min
410-OQT-450-2	160 °C	450 °C	2 min
410-OQT-450-5	160 °C	450 °C	5 min
420-OQT-450-5	99 °C	450 °C	5 min
420-RTQ-450-5	30 °C	450 °C	5 min
420ma-OQT-450-5	62 °C	450 °C	5 min
420ma-RTQ-450-5	30 °C	450 °C	5 min

3.2.2. Q&P processing of large sheets

Once the optimum Q&P heat treatments are defined for each alloy, as reported in Section 5.1.2.3, their implementation on an industrial scale is carried out. To recreate an industrial implementation two furnaces have been used at the RINA Consulting – Centro Sviluppo Materiali facilities (Rome, Italy). Cold-rolled sheets with 1.5 mm thickness and a width of 200 mm were used. The length of the sheets for alloys 420 and 420ma is 500 mm, and for alloy 410 is 250 mm, to ease the thermal homogeneity during its quench. The temperature is monitored via a thermocouple welded at the center of each sheet (half-length and mid-width).

Figure 3-2 shows a schematic representation of the heat treatment applied to the large sheets using two furnaces. The first furnace is used for the austenitization stage for all the alloys with the same parameters (1100 °C for 15 min). In the case of alloys 410 and 420, after the austenitization process, the samples are transferred to the second furnace at their respective quenching temperature QT (Table 3-5) for their quenching time (Qt). Once this Qt is passed, the temperature of the furnace is increased to 450 °C to continue with the partitioning stage. After 5 min at 450 °C, the sheets are removed and left to air cool to room temperature. In the case of alloy 420ma, after the austenitization stage is completed, the sheet is removed from the furnace, left to air cool until 250 °C (controlled by the thermocouple), and then water quenched. Once the temperature of the sheets is homogeneous, the sheets are transferred to the second furnace at 450 °C for the partitioning stage. Following the 5 min partitioning period, the samples are left to air cool outside the furnace until room temperature is achieved.

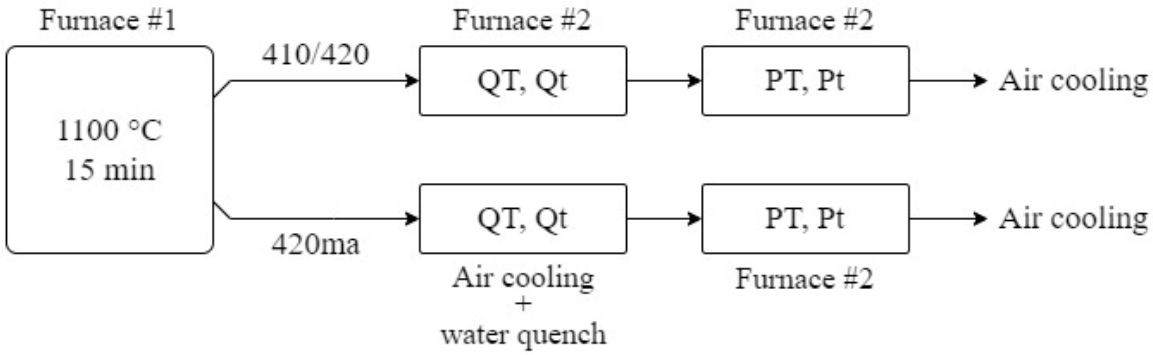

Figure 3-2. Q&P heat treatment for the large sheets.

In Table 3-5, the optimal Q&P parameters for the heat treatment of the large sheets are collected. As it can be observed, there are small deviations from these parameters to the ones reported in Table 3-4 (or chosen in Section 5.1.2.3), such as the QT for alloy 420 (reduced from 99 °C to 90 °C) or the variation of the Qt (20 s in Table 3-3 to various times in Table 3-5). The reason behind these changes is to improve thermal homogeneity of the samples (lower quenching temperatures and longer quenching times). Furthermore, in this experimental process, the heating and cooling rates are not as precisely regulated as in the GLEEBLE simulator. Consequently, these slight changes of temperatures serve to eliminate thermal gradients. As demonstrated in Section 5.1, these minor adjustments in the heat treatment process have a minimal effect on the final microstructure of the Q&P-treated large sheets when compared to the GLEEBLE-treated samples.

Table 3-5. Optimal Q&P parameters for the heat treatment of the large sheets.

Alloy	QT	Qt	PT	Pt
410	160 °C	30 s		
420	90 °C	45 s	450 °C	5 min
420ma	20 °C	120 s		

3.3. Microstructural characterization

A wide range of experimental techniques has been employed to characterize the microstructure of the materials under investigation. These techniques and corresponding experimental procedures are described below.

3.3.1. Scanning Electron Microscopy (SEM) & Energy Dispersive X-Ray Spectroscopy (EDS)

Scanning electron microscopy is the generation of images produced by the scanning of an area with a focused beam of electrons. There are multiple interactions of the incident electrons with the surface of the material and, depending on the detector selected, the obtained information can be on the topography, the chemical composition or the crystallography. Usually, a scanning electron microscope (SEM) is equipped with multiple detectors. One of the most extended

detectors is the Everhart–Thornley detector (ETD) which reads the signal of both secondary electrons and backscattered electrons. In this work, it is used to obtain high magnification (x2500) images. Additionally, energy dispersive X-ray spectroscopy (EDS) is a technique that usually appears in combination with SEM, as it only requires a spectrometer. This detector measures the energy levels of the X-rays generated in the material (sub)surface. These measurements provide quantitative information on the local chemical composition of the observed sample. It is a useful technique to identify inclusions and precipitates.

The requirements for sample preparation are not excessive. However, for the consistency of the measurements, the standard metallographic preparation is applied to all samples. It consists of the following steps: grinding the sample with successively finer sandpapers (from 320 to 2000 grit), polishing with diamond pastes of 6, 3 and 1 μm; and finishing with a polishing step using a suspension of colloidal silica (OP-S, brand Struers). A slightly etched mirror-polished surface is achieved at the end of this process.

The SEM used in this work is an APREO 2S LoVac equipped with an Oxford Instruments Ultim Max 40 detector controlled by the AZtec Oxford Instruments Nanoanalysis (version 5.0) software. The data are acquired at an accelerating voltage of 20 kV and a working distance of 13 mm.

3.3.2. Electron Backscatter Diffraction (EBSD) analysis

Another of the detection technologies that can be integrated into a SEM is electron backscatter diffraction (EBSD) detector. This detector collects the pattern left by the backscattered electrons after their diffraction through the crystal lattice. This pattern receives the name of Kikuchi pattern, and can be matched with material databases to identify the crystal lattice (and thus the material studied) and its spatial orientation.

The Apreo SEM is equipped with an Oxford Instruments Symmetry S2 EBSD detector controlled by the AZtec Oxford Instruments Nanoanalysis (version 5.0) software. The acquisition parameters are an accelerating voltage of 20 kV, a working distance of 13 mm, a tilt angle of 70°, and a step-size of 50 nm. Samples for this technique are prepared following standard metallographic procedures, as described in the previous section.

The analysis of the acquired EBSD maps is performed using the HKL Post-processing Oxford Instruments Nanotechnology software (version 5.12) and TSL Data analysis version 8.0 software. These programs allow for the generation of phase content maps, IPF (Inverse Pole Figure) maps, KAM (Kernel Average Misorientation) maps, etc.; and statistical data. Additionally, the MTEX package (version 5.9.0), developed for Matlab, is utilized to study the hierarchy of the martensitic microstructure (martensite packets and martensite blocks) and perform the reconstruction of prior austenite grains (PAG) using the routine developed by T. Nyyssonen et al. [56].

The volume fractions of tempered martensite, fresh martensite and retained austenite are determined by a two-step partitioning procedure [57]. In this procedure, retained austenite and martensite are separated in the first step (Figure 3-3a). The iron fcc phase exclusively consists of retained austenite, while the iron bcc contains tempered martensite and fresh martensite. In the second step, fresh martensite (FM) and tempered martensite (TM) are separated using the

grain average image quality (GAIQ) criterion (Figure 3-3b) which is directly correlated to the sharpness of the Kikuchi pattern. The fresh martensite formed during the final quench derives from retained austenite that was not sufficiently stabilized during the partitioning step. Therefore, fresh martensite demonstrates lower GAIQ values compared to tempered martensite due to higher lattice distortions caused by a higher carbon content. The threshold GAIQ value is selected based on the distribution of GAIQ values in the map and the grain size. Furthermore, fresh martensite should be located close to retained austenite clusters and/or between tempered martensite laths, and it should be smaller in size and rounder in shape than tempered martensite. Additionally, fresh martensite has low quality on the band contrast map. This is used as another criterion to validate the selected GAIQ threshold value. Grain size is calculated as an average equivalent circular diameter. The microstructure is observed on the plane perpendicular to the sample transverse direction (the RD–ND plane).

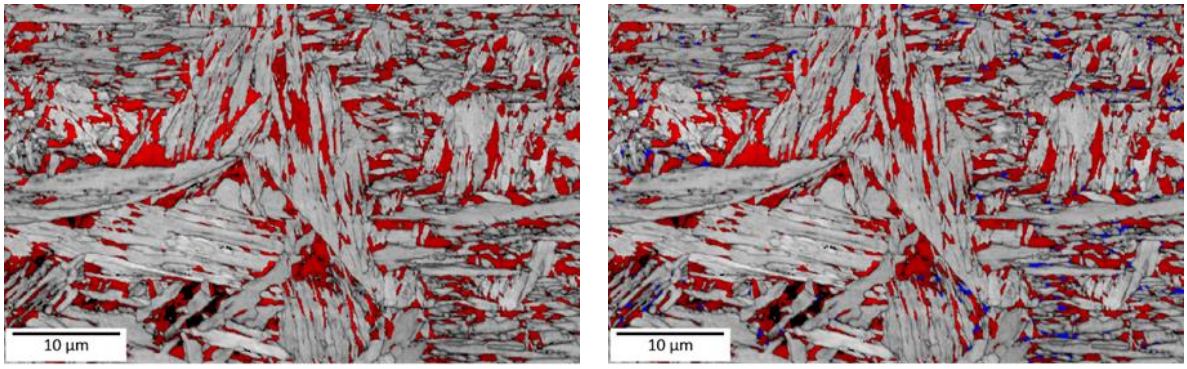

a) *b)*

Figure 3-3. A typical EBSD phase map of 420ma sample with identified microstructural constituents: a) in the first step, retained austenite (RA) in the martensitic matrix is detected; b) in the second step, fresh martensite (FM) and tempered martensite (TM) are discriminated. FM is in blue, RA is in red, and TM is the matrix.

3.3.3. X-Ray Diffractometry (XRD) analysis

X-ray diffractometry (XRD) is a non-destructive technique that allows in the present study to characterize the volume fraction of retained austenite, its lattice parameter and the carbon content of this phase. The X-rays with a wavelength λ are generated against a target inside the diffractometer. The X-rays' photons hit the sample with an angle ω, and transfer part of their energy to the electrons of the atoms. The photons are emitted (or scattered), and those that maintain the same wavelength (elastic scattering) may interfere with each other constructively, thus generating the diffraction pattern [58]. When considering atoms spaced a distance d, Bragg's law relates these parameters and is fundamental for the interpretation of the generated diffraction pattern (Eq. 3.4).

$$\lambda = 2d \sin \omega \qquad \textit{(Eq. 3.4)}$$

The X-ray diffractometer used in this thesis is an Empyrean from PANalytical. It is operated with a Cu K_α target at 45 kV and 40 mA. The scans were performed in the range of 40~105° with a step size of 0.05°. The sample preparation required for this technique is less demanding than for SEM imaging, as just a grinding up to 2000 grit sand paper is sufficient.

From the obtained diffraction spectra, the first set of data that can be derived is the volume fraction of austenite using Rietveld refinement [59] along with the reference patterns for austenite and martensite (Table 5-4). By analyzing the diffraction spectra's peak characteristics (peak position, associated crystallographic plane and interplanar spacing), the Nelson-Riley function (Eq. 3.5) can be applied to calculate the increment of the lattice parameter of the austenite for a specific diffraction peak [60], and with (Eq. 3.6) the lattice parameter for that peak is calculated. Plotting the Nelson-Riley function against the corresponding increment of austenite lattice parameter, performing a linear regression and determining the y-intercept (where the Nelson-Riley function takes value 0) the lattice parameter of the austenite is calculated (Table 5-5).

$$f(\theta) = \left(\frac{\cos\theta^2}{\sin\theta} + \frac{\cos\theta^2}{\theta}\right) \qquad \textit{(Eq. 3.5)}$$

$$\frac{1}{d^2} = \frac{\sqrt{h^2 + k^2 + l^2}}{a^2} \qquad \textit{(Eq. 3.6)}$$

3.3.4. Magnetometry study

Another technique that is used for measuring the volume fraction of retained austenite in the Q&P-treated specimens is magnetometry, following the method detailed in [61]. In summary, a magnetometer measures the induced magnetization on the sample under an applied magnetic field. The sample reaches a maximum value called magnetization saturation (M_{sat}), which corresponds to the sum of all magnetic moments in the steel aligned with the applied field. The M_{sat} of the studied steel alloys can be calculated using the Fe content (x_{Fe}, in wt.%) of the three grades and the saturation magnetization of pure BCC-Fe ($M_{sat}^{Fe} = 215\ \mathrm{Am^2kg^{-1}}$) [62].

$$M_{sat}^{alloy} = M_{sat}^{Fe} \cdot x_{Fe} \qquad \textit{(Eq. 3.7)}$$

Considering that martensite is ferromagnetic and austenite is paramagnetic, it can be assumed that the magnetization of the samples is due to martensite content, since the susceptibility of the ferromagnetic materials is superior. Therefore, the martensite fraction is the ratio between the measured magnetization saturation measured in the sample and the magnetization saturation of the same grade (M_{sat}^{alloy}). A simple mass balance results in the retained austenite fraction (Eq. 3.8).

$$V_{RA} = 1 - \frac{M_{sat}^{sample}}{M_{sat}^{alloy}} \qquad \textit{(Eq. 3.8)}$$

The magnetometer used for this analysis is a Lakeshore VSM 7307, located in the Technical University of Delft (The Netherlands). The experiments were carried out by me during my 3-month research stay. The tests were carried out at room temperature, and the magnetic field applied ranged from 2 T to -2 T. Small cubes of around 2x2x2 mm^3 are required for this technique. The results from this technique should provide a more representative measurement

since it measures the bulk of the material rather than a local surface area (as it is the case for EBSD and XRD).

3.3.5. High resolution Transmission Electron Microscopy (TEM) & Energy Dispersive Spectroscopy (EDS)

Transmission electron microscopy (TEM) is based on the transmission of electrons through the thickness of a very thin sample. The transmitted electrons undergo energy and trajectory modifications, providing insights into the internal structure of the material [63]. This technique allows to reach atomic resolution, much finer than the previously mentioned SEM. However, just like in SEM, the interaction of electrons with the material also causes the emission of X-rays, which can be employed in energy dispersive spectroscopy (EDS) to locally analyze the chemical composition. In the present work, this high-magnification EDS is fundamental for the identification of the TiC and NbC nanocarbides.

The TEM microscope used is a FEG S/TEM (Talos F200X, FEI) operated at an accelerating voltage of 200 kV. Integrated in it, EDS detector SuperX (4 detectors) from FEI & Bruker allows to carry out elemental mapping. For this technique, the samples are ground down to a thickness of 0.1 mm. These thin foils are then further thinned out on a TenuPol 5 (Struers®) by twin-jet electropolishing with 10% perchloric acid in acetic acid at 15 °C at an operating voltage of 40 V. TEM imaging was carried out in bright-field (BF) and high-angle annular dark field (HAADF) modes.

3.4. Characterization of properties

To explore the effect of the Q&P heat treatment on the properties of martensitic stainless steels, three different kinds of testing are carried out: tensile testing, fatigue testing and formability testing. In the following sections, each one is briefly explained.

3.4.1. Tensile testing

For the characterization of the basic mechanical properties, the tensile tests are chosen, as they allow to determine strength and ductility. Two different sizes of specimens are used during the testing campaigns. The GLEEBLE-treated materials (Section 3.2.1) are machined to obtain sub-size tensile specimens (Section 3.4.1.1). From the large Q&P-treated sheets (Section 3.2.2), standard tensile samples are machined (Section 3.4.1.2).

3.4.1.1. Tensile testing of sub-size samples

The constraints of the coupon size during the GLEEBLE processing lead to the sub-sizing of tensile specimens. Samples with a gauge length of 4 mm and a gauge width of 1 mm are machined from the midsection of the Q&P-treated coupons (Figure 3-1c). The tensile axis is parallel to the rolling direction. The surface of the machined samples is carefully ground to remove the oxide layer, so the final thickness of the samples is ~0.9 mm.

Tensile tests are carried out at room temperature and strain rate of 10^{-3} s^{-1} using a Kammrath&Weiss testing module. The outcomes of tensile tests are analyzed, and basic mechanical properties (yield strength $\sigma_{0.2}$, ultimate tensile strength σ_{UTS}, uniform elongation ε_u, and elongation to fracture ε_t) are measured. To determine the strain hardening exponent n, true stress – true strain curves are plotted and fitted by the simple power law $\sigma = K \cdot \varepsilon^n$, where K is the strength coefficient. At least two tests are performed for each condition, and the results are found to be reproducible.

3.4.1.2. Standard tensile testing

From the large Q&P-treated sheets, samples are machined for standard uniaxial tensile testing. Dog bone samples (gauge length of 50 mm and gauge width of 12.5 mm) are machined oriented at 90° angle to the rolling direction. Similar to the sub-size samples, the surface of the standard samples undergoes careful grinding to remove the damaged layer from the rolling process.

Following the standard ASTM E8-M [64], tensile tests are conducted using a universal testing machine at room temperature and strain rate of 10^{-3} s^{-1}. Three tensile specimens are tested per alloy. From these curves, the yield strength ($\sigma_{0.2}$), the ultimate tensile strength (σ_{UTS}), and elongation to fracture (ε_t) are obtained.

3.4.2. High-cycle fatigue

Specimens for fatigue testing are also machined from the large Q&P-processed sheets. The geometry of samples is presented in Figure 3-4. The surface of the specimens is carefully prepared using standard metallographic techniques to remove the superficial defects induced during the machining process and the oxide layer formed during the Q&P process. Additionally, it improves the surface quality. After sample preparation, the high-cycle fatigue tests are performed in pull-pull stress-controlled mode using sinusoidal-waveform cyclic loading. The experiments are carried out at room temperature using an INSTRON 8802 servo-hydraulic fatigue testing system according to the ISO 1099 standard [65]. The stress ratio R is 0.1, and the load frequency is 50 Hz. The stress amplitude σ_a values are in the range of 260 – 490 MPa. The number of cycles to failure is recorded, and the S-N curves (Wöhler curves) are plotted. At least 14 samples are tested per each material. The fatigue limit σ_f is estimated from the obtained S-N curves.

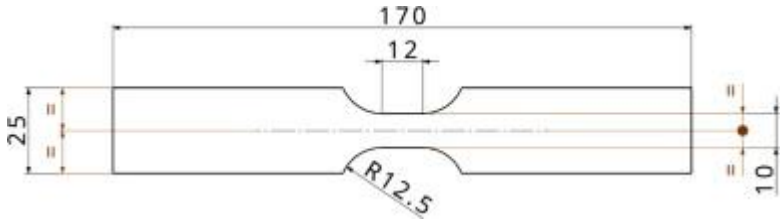

Figure 3-4. Geometry of samples used for high-cycle fatigue testing.

3.4.3. Formability testing

The large Q&P-treated steel sheets are machined to obtain a set of Nakajima specimens for alloys 410 and 420ma. Each group of Nakajima specimen encompasses five different geometries, which offer varying relationships between gauge length and gauge width (Figure

3-5). Thus, the stress state in the plane would be sampled from uniaxial (Geometry 1, Figure 3-5a) to biaxial (Geometry 5, Figure 3-5e). Prior to Nakajima testing, each specimen receives a square grid pattern for subsequent digital image correlation (DIC) analysis. The samples are clamped, applying 220 kN of blank holding force, and oil-lubricated to reduce friction with the punch. The punch used is semispherical and 100 mm in diameter, and its velocity is 25 mm/min. The test is sampled with a frequency of 5 Hz and stopped at the failure of the specimens. The strain measurements are extracted using DIC analysis of the deformed grid of the tested specimens. These experiments were performed by RINA Consulting – Centro Sviluppo Materiali (Rome, Italy), our collaborator.

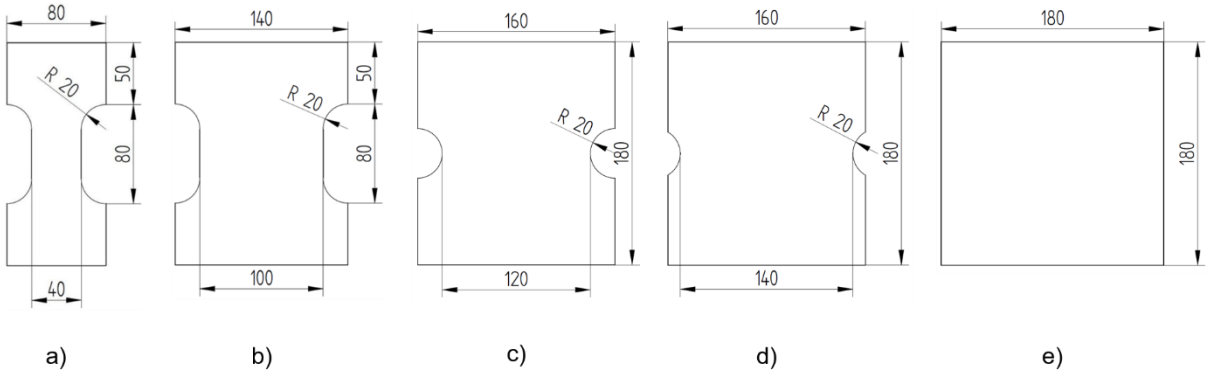

Figure 3-5. Five geometries of the specimens for Nakajima testing. From a) to e) Geometries 1 to 5.

4. FEM model for formability testing and cold-forming of automotive parts

The development of the FEM model for the formability testing and the cold-forming of automotive parts was performed by project collaborator Dr. Juan Luis de Pablos Gómez, and it has been reported in the article "*Assessing the feasibility of cold-forming of automotive parts from quenched and partitioned martensitic stainless steels*" (DOI: 10.1002/srin.202300280).

In this section, a comprehensive insight into the Johnson-Cook (J-C) constitutive model is given, including its mathematical formulation and the approach taken when using it for the development of formability simulations.

4.1.1. Johnson-Cook model in formability studies

The use of the J-C constitutive model to reproduce the mechanical behavior of materials undergoing forming processes is fairly standardized. In particular, Wang et al. [66] employ the mentioned equation to simulate the stamping process of preheated boron steel samples. A good match between simulated results and experimental data is found, thus enabling numerical prediction before performing the physical process at an industrial level. On the other hand, in another work [67], Yan et al. analyze the prediction capabilities of the model regarding the simulation of a steel material when subjected to the cold roll-beating, finding that the data of the true stress generated during the simulated procedure are consistent with those obtained with experimental methods. Likewise, in [68] Aghdami and Davoodi find a good agreement of the numerical data with regard to the prediction of the behavior of copper and aluminum alloys when being processed through a cold wire drawing cycle. In [69], Ben et al. explore the simulation of the oscillating cold forming process by using the J-C model coupled with different unloading models, finding that one of the combinations could successfully describe the experimentally observed deformation. It must be emphasized that while the J-C model is capable of simulating materials experiencing deformations under variable strain rate and temperature conditions, its application in scenarios, where strain is the only variable, does not diminish its simulation capabilities. In situations where only strain varies, as observed in previous studies [66]–[69], the J-C model is capable of independently handling this variable. This is due to the model's formulation, which accounts for the inherent independence of strain, strain rate, and temperature by representing them as separate factors in the equation.

Nevertheless, when employing a widely applicable strength model such as the J-C model in this case, it is essential to consider its use in conjunction with another constitutive equation that incorporates the material's fracture behavior. The strength model establishes the material's limits for failure under the given simulated conditions. In particular, a similar approach has already been used in the previous work by Panich et al. [70], where a yield model is coupled with the Forming Limit Diagram (FLD) and Forming Limit Stress Diagram (FLSD) fracture criteria to assess the formability of steel sheets under stamping processes, having as an outcome a successful prediction when comparing the data with those extracted from real experiments.

These works strengthen the initial hypothesis considered in this work, relying on the employment of the aforementioned constitutive equation coupled with either a strain-based or a stress-based criterion to properly assess the different martensitic stainless steels under study when used in industrial cold forming.

4.1.1.1. Johnson-Cook constitutive relations

The J-C constitutive model has been widely employed in the simulation of the plastic behavior of metals under conditions of large strains, high strain rates and high temperatures. It is not considered to be a constitutive equation able to offer extremely accurate predictions for all the possible variable ranges, but among its advantages, it counts on fair robustness and its computational implementation is relatively simple. Due to this, it has been used over the last decades in a wide spectrum of applications: machining simulations [71]; hot stamping process [72]; and Charpy test simulations [73].

The J-C constitutive equation is one of the J_2 classical plasticity models, in which the yield stress σ_y is assumed to be of the form

$$\sigma_y = \left(A + B\varepsilon_p^n\right)\left(1 + C\log\dot{\varepsilon_p^*}\right)(1 - \theta_*^m) \qquad \textit{(Eq. 4.1)}$$

where there are three main terms. The first part refers to the quasi-static hardening, in which the initial yield stress, A, together with the parameters representing the strain hardening, B and the exponent n can be found, as well as the variable ε_p, representing the equivalent plastic strain. The second one is related to the hardening provoked by the strain rate effects, where the strain rate parameter, C, as well as the dimensionless plastic strain rate, $\dot{\varepsilon_p^*} = \frac{\dot{\varepsilon_p}}{\dot{\varepsilon_{p_0}}}$, including $\dot{\varepsilon_{p_0}}$ as a reference plastic strain rate chosen in accordance to the lowest experimental values expected, are found. Finally, the third term, which accounts for the effects of temperature, includes the thermal softening exponent, m, and also the so-called "homologous temperature", as

$$\theta_* = \frac{\theta_{exp} - \theta_{room}}{\theta_{melt} - \theta_{room}} \qquad \textit{(Eq. 4.2)}$$

where θ_{exp} represents the experimental temperature at which the material is being modeled, θ_{melt} is the melting temperature of the material and θ_{room} is the ambient temperature for the minimum experimental reference.

4.1.2. Development of FEM models

FEM models are employed in this work to accomplish two objectives: Firstly, to replicate experimental tests and validate themselves by comparing the results with different material properties obtained from real data. Secondly, to predict the outcome of forming processes, specifically the cold stamping of automotive parts.

Nakajima experiments carried out using three different Q&P martensitic stainless steels are simulated, as shown in Figure 4-1, in order to validate the ductile fracture limits observed during the actual tests, being these expressed in the form of the equivalent plastic strain, ε_p , and the FLD curves. The latter referred simulated models are created employing the Computer Aided Engineering (CAE) software ABAQUS, in which the experiment is replicated by modeling the die, holder and the hemispheric punch parts as rigid 3D shells, being the first two fixed, holding the sample in place based on a penalty friction formulation with a coefficient of 0.02, while the

punch moves vertically at a constant speed of 1.5 mm/s, as dictated by the ISO standards 12004-1 [74] and 12004-2 [75]. All the parts count on axisymmetric displacement boundary conditions so that only a quarter of the whole setup can be simulated, saving important computational effort. More in detail, each of the differently shaped quarter-sheet parts are modeled through deformable 3D shells, with meshes consisting of approximately 5500 linear-S4R elements, counting on 6 integration points equally distributed over the 1.5 mm thickness of the sheets. The simulations are solved by employing an explicit integration scheme assisted by mass scaling techniques, aiming at reducing the overall computational cost.

a)

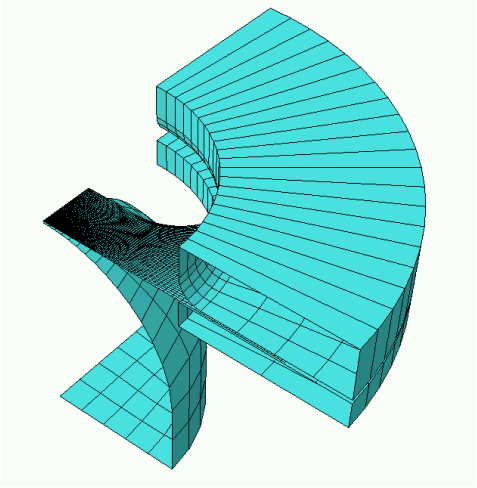

b)

Figure 4-1. a) Nakajima samples after testing (1–5, from left to right) and b) computational layout of Nakajima test using ABAQUS software.

The simulation of the behavior of each steel is approached from the plasticity point of view, considering two initial perspectives. The first relied on the use of the stress-strain curves recorded for each alloy during tensile tests carried out beforehand. While the second, and eventually the one which is chosen, is based on the use of the J-C constitutive model, whose parameters are obtained also employing the data from the latter experiments, with a similar method as the one shown in [76], and then validated employing the force vs. displacement curves extracted from the Nakajima tests.

Thus, once the model is set, the Quantities of Interest (QoI) ε_p and the FLD curves are recorded in the simulations and compared with those acquired during the tests, therefore aiming at validating them. Subsequently, the extraction of the Forming Limit Stress Diagram (FLSD) curves for each material is conducted through simulations of Nakajima tests. This approach proves advantageous as it circumvents the high cost associated with attempting to obtain these

curves directly through experimental procedures. Recording the entire deformation path in the failure region is necessary to calculate these values, as indicated by the Levy-Mises relation,

$$d\boldsymbol{\varepsilon_{ij}} = d\lambda \boldsymbol{s_{ij}} \qquad \textit{(Eq. 4.3)}$$

where the tensor of incremental strain ($d\boldsymbol{\varepsilon_{ij}}$) is proportional to the plastic slip $d\lambda$ and the tensor of deviatoric stress $\boldsymbol{s_{ij}}$,which, in turn, depends on the non-incremental tensor of strain $\boldsymbol{\varepsilon_{ij}}$. Finally, after carrying out the extraction of this alternative ductile fracture criteria of the three steels through numerical methods, some relevant stamping simulations are performed. These involve the cold stamping process of two automotive parts, namely the B-pillar and the central transmission tunnel of generic automobiles, being both representative examples of the standard usage and application of the materials studied.

5. RESULTS & DISCUSSION

5.1. Effect of chemical composition and Q&P parameters on the microstructure

In this section, the microstructure of Q&P-treated martensitic stainless steel is characterized. Samples from the two processing routes are studied using EBSD, XRD, TEM and magnetometry techniques to measure phase volume fractions, size and morphology of the microstructural constituents and chemical composition. The as-received material is also characterized to study the effect of the Q&P heat treatment on the initially present nanocarbides.

5.1.1. Microstructure of the as-received materials

Figure 5-1 presents typical microstructures of the as-received material, observed via SEM. Alloys 410 and 420 presented a homogeneous martensitic microstructure (Figure 5-1a). In contrast, alloy 420ma has a martensitic matrix with residual ferrite (Figure 5-1b). This banded microstructure can be associated to segregation of alloying elements with increased content (Mn and Cr) having low diffusivity [77], as shown in the measured EDS maps (Figure 5-2). The values for the measured mass fraction of alloying elements within the band and outside the band are reported in Table 5-1, confirming the segregation of Cr and Mn.

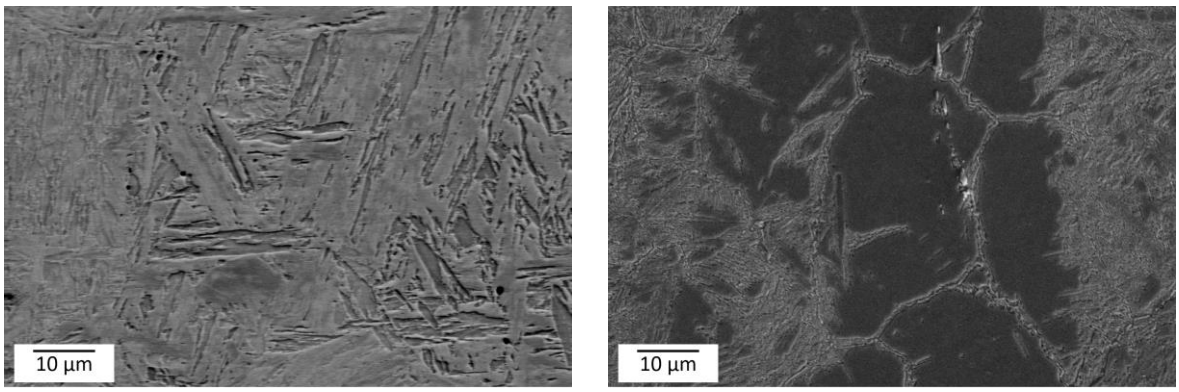

a) Alloy 410 as-received *b) Alloy 420ma as-received*

Figure 5-1. SEM images of the microstructures of the as-received materials.

Table 5-1. Alloying element contents (wt. %) inside and outside bands in as-received alloy 420ma measured via EDS.

Element	Area 1 (within band)	Area 2 (outside band)
Fe	80.7 %	82.9 %
Cr	14.0 %	12.3 %
Mn	4.0 %	2.6 %

HR-TEM coupled with EDS are used to assess the initial presence of carbides in the as-received alloy 420ma. The resulting elemental maps are collected in Figure 5-3, where two different composition of carbides can be identified: the sought-of (Ti,Nb)C and undesired (Cr,Mn,Mo)C. As previously explained in Section 3.2, the first step of the proposed Q&P treatments completely austenitizes the as-received microstructure. Hence, the as-received microstructure

does not significantly influence the final Q&P-treated microstructure. However, in the case of alloy 420ma, the austenitizing parameters are selected to maintain the presence of TiC and NbC nanocarbides while dissolving other undesired carbides. In the following sections (Sections 5.1.2 and 5.1.3) it is demonstrated that the undesired carbides are dissolved with the austenitizing step, and the TiC and NbC nanocarbides remain in the microstructure.

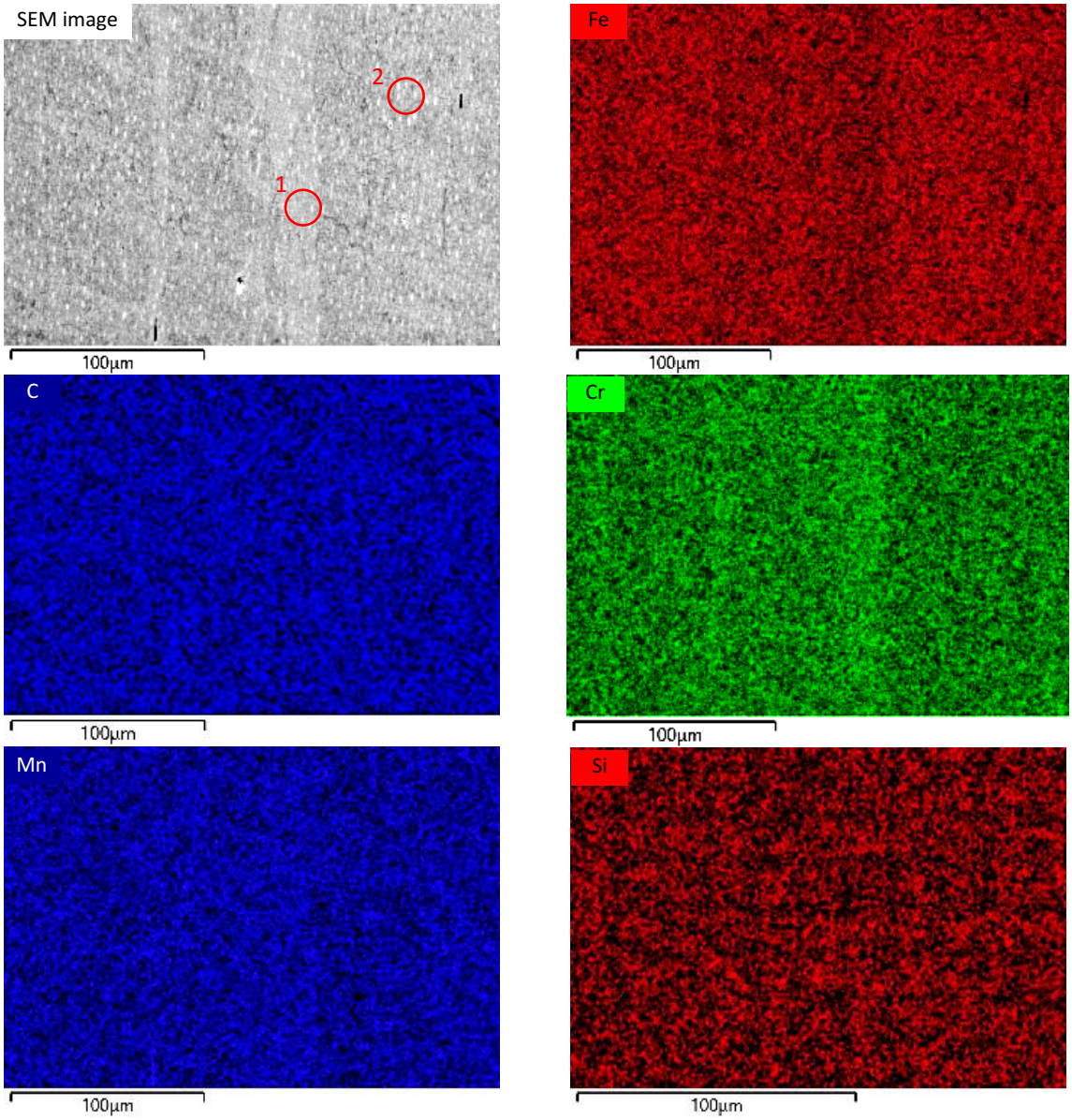

Figure 5-2. EDS elemental maps of banded microstructure present in the as-received alloy 420ma. Point 1 and Point 2 correspond to the analyzed areas inside and outside the band, respectively, and those results are shown in Table 5-1.

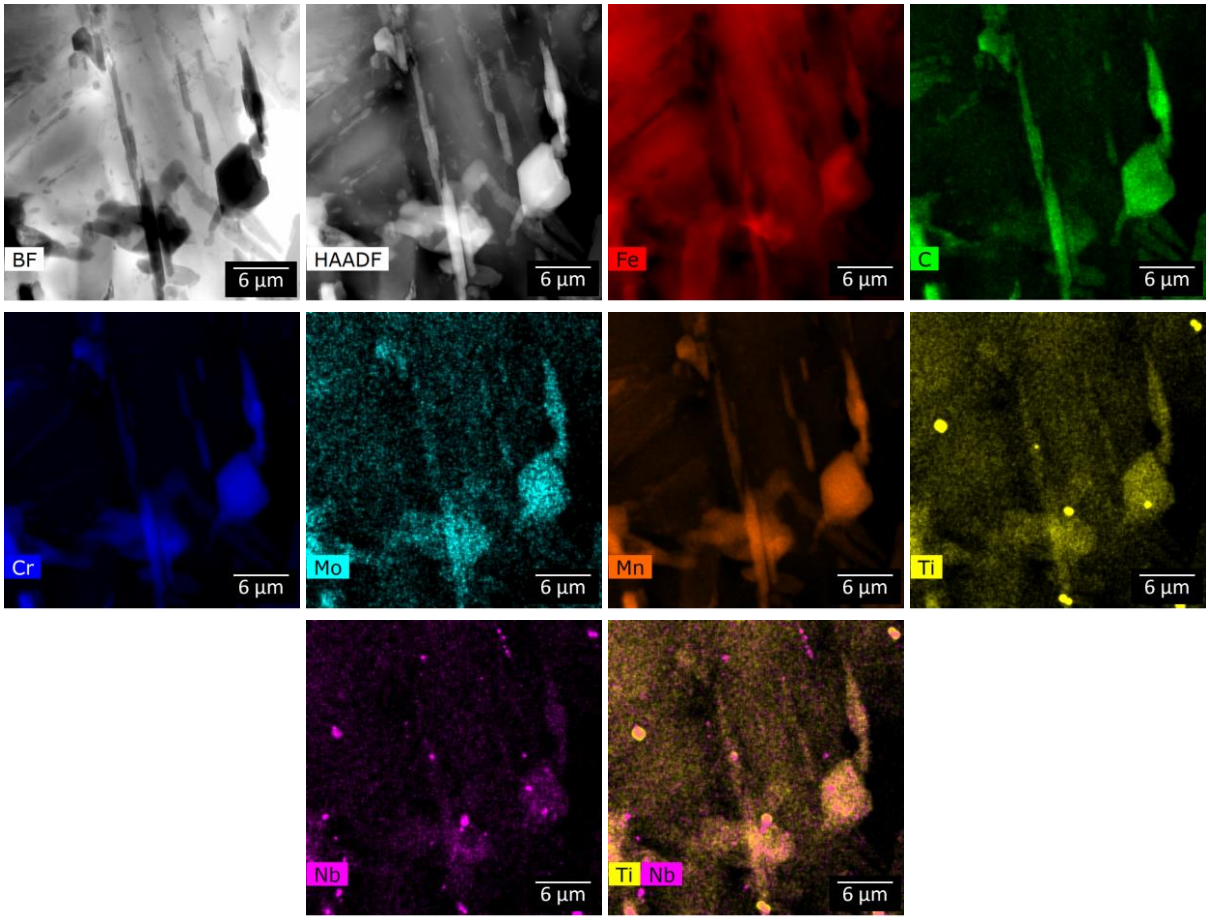

Figure 5-3. Bright field (BF) and high-angle annular dark field (HAADF) TEM images with corresponding elemental maps of as-received alloy 420ma.

5.1.2. Microstructure of samples after physical simulation of Q&P process

The experimental work begins with the microstructural characterization of the samples Q&P-treated using the thermo-mechanical simulator GLEEBLE 3800. Figure 5-4 illustrates typical EBSD band contrast maps overlaid by an IPF map for retained austenite grains and corresponding KAM maps of these GLEEBLE-treated samples. The alloys/conditions showing the highest (Figure 5-4c), average (Figure 5-4a) and lowest (Figure 5-4b) local volume fractions of retained austenite are presented. The retained austenite grains are homogeneously distributed over the microstructure of all studied samples. Two morphologies of retained austenite can be noted: blocky morphology (relatively large equiaxed grains having a size of ≥ 1 µm) and interlath (finer elongated grains). Retained austenite grains do not show any preferred crystallographic orientation (Figure 5-4). The lath structure of the martensitic matrix is also clearly seen. The KAM maps (Figure 5-4) demonstrate that the interior of martensite lath has nearly zero misorientation, whereas the martensite lath boundaries show higher misorientation of 1 – 1.5°. Some ultra-fine non-indexed areas on the maps (white pixels on the KAM maps, Figure 5-4) may correspond to fresh martensite, which could not be indexed, as the high carbon content results in high lattice distortion [57], [78]. They are usually adjacent to retained austenite grains. Also, the grain, packet, block and lath boundaries cannot be indexed due to overlapping patterns.

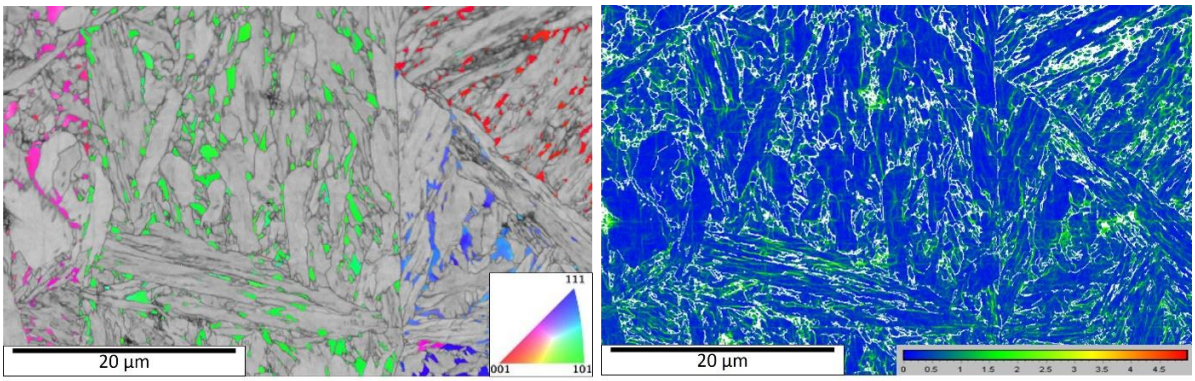

Retained austenite in IPF Z overlay *KAM*

a) 410-OQT-450-5 (Average local volume fraction of retained austenite, 9.6 %)

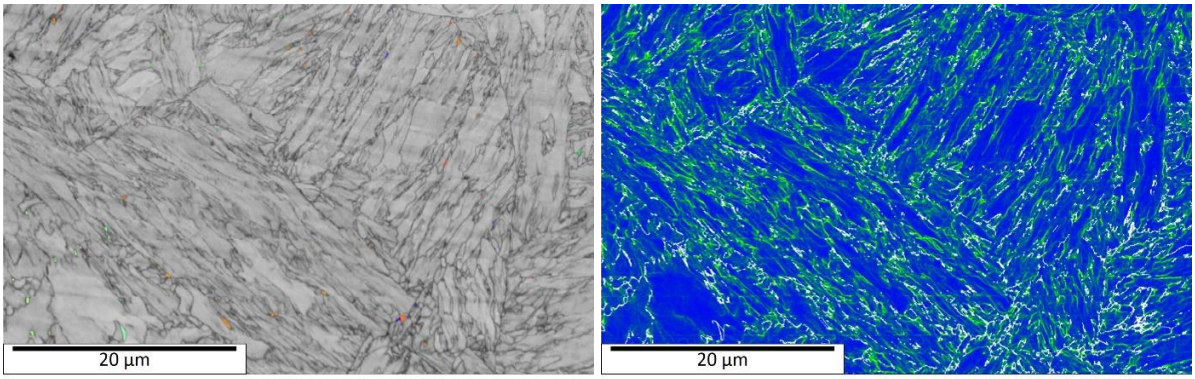

Retained austenite in IPF Z overlay *KAM*

b) 420-RTQ-450-5 (Lowest local volume fraction of retained austenite, 0.4 %)

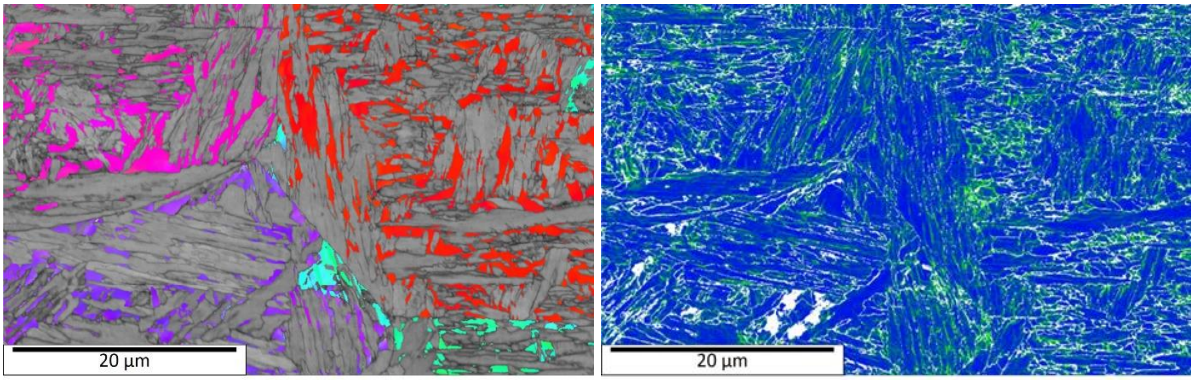

Retained austenite in IPF Z overlay *KAM*

c) 420ma-OQT-450-5 (Highest local volume fraction of retained austenite, 15.5 %)

Figure 5-4. Typical microstructures of the Q&P-treated samples in the GLEEBLE system. Left: EBSD band contrast map overlaid by retained austenite IPF Z map; Right: KAM map of the corresponding area.

The local volume fractions of the microstructural constituents and their size after different Q&P treatments applied to the studied alloys are listed in Table 5-2 and Table 5-3, respectively. The histograms of grain size distribution for retained austenite are compared in Figure 5-6. It is seen that the increase of the partitioning temperature and time is beneficial for the 410 alloy, as the local volume fraction of retained austenite increases from 6.7 % to 9.6 % (Table 5-2). There is no significant effect of the Q&P parameters on the retained austenite grain size (Table 5-3). The matrix microstructure in all materials exhibits a typical lath martensite structure which is schematically shown in Figure 5-5. As is well known, it is characterized by a hierarchical sub-grain structures comprising packets, blocks and laths of particular crystallography [14]. Prior austenite grains are divided into several packets, each of which consists of blocks. These microstructural constituents of the martensitic matrix in all studied alloys vary widely in size and do not show a clear dependence on the applied Q&P treatment parameters (Table 5-3).

Table 5-2. Local volume fractions of the individual microstructural constituents measured by EBSD.

Alloy	Sample	Local volume fractions of microstructural constituents [%]			Non-indexed pixels [%]
		Retained austenite	Tempered martensite	Fresh martensite	
410	410-OQT-400-5	6.7	74.7	2.6	16.0
	410-OQT-450-2	6.7	77.3	5.3	10.7
	410-OQT-450-5	9.6	74.8	3.3	12.3
420	420-OQT-450-5	9.7	75.6	2.3	12.4
	420-RTQ-450-5	0.4	86.3	5.7	7.6
420ma	420ma-OQT-450-5	15.5	61.1	4.4	19
	420ma-RTQ-450-5	14.5	67.3	3.6	14.6

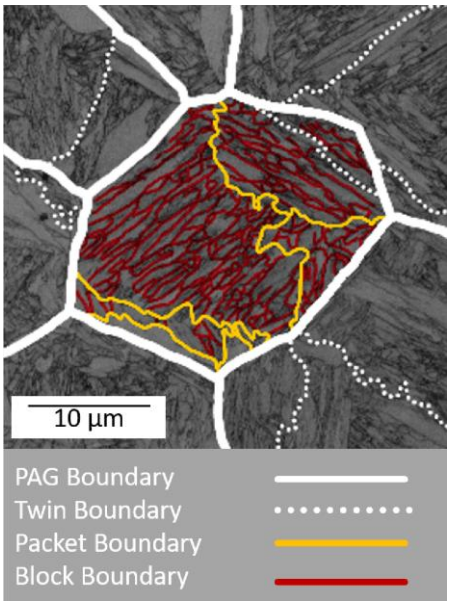

Figure 5-5. A fragment of EBSD band contrast map illustrating prior austenite grain (PAG) boundaries, martensite packet boundaries and block boundaries (in the central grain) in the Q&P-treated 420ma alloy.

Table 5-3. Size of the individual microstructural constituents measured by EBSD.

Sample	Microstructural parameters [μm]					
	Retained austenite grain size	Martensite packet size	Martensite block size	Martensite lath width	Fresh martensite size	Prior austenite grain size
410-OQT-400-5	0.6 ± 0.2	17.5 ± 8.2	3.1 ± 1.3	0.9 ± 1.2	0.4 ± 0.09	
410-OQT-450-2	0.6 ± 0.2	12.3 ± 7.8	3.3 ± 1.9	0.6 ± 0.8	0.4 ± 0.04	37.7 ± 9.7
410-OQT-450-5	0.7 ± 0.3	11.3 ± 4.8	2.9 ± 0.7	0.7 ± 1.0	0.6 ± 0.11	
420-OQT-450-5	0.7 ± 0.4	13.2 ± 2.0	2.4 ± 0.4	0.5 ± 0.9	0.4 ± 0.01	36.2 ± 16.7
420-RTQ-450-5	0.5 ± 0.1	16.2 ± 5.3	2.8 ± 0.9	0.9 ± 1.0	0.4 ± 0.03	
420ma-OQT-450-5	0.8 ± 0.5	9.9 ± 5.1	2.8 ± 0.7	0.7 ± 0.9	0.5 ± 0.16	21.7 ± 4.1
420ma-RTQ-450-5	0.8 ± 0.5	11.0 ± 3.4	2.5 ± 0.8	0.7 ± 1.1	0.4 ± 0.01	

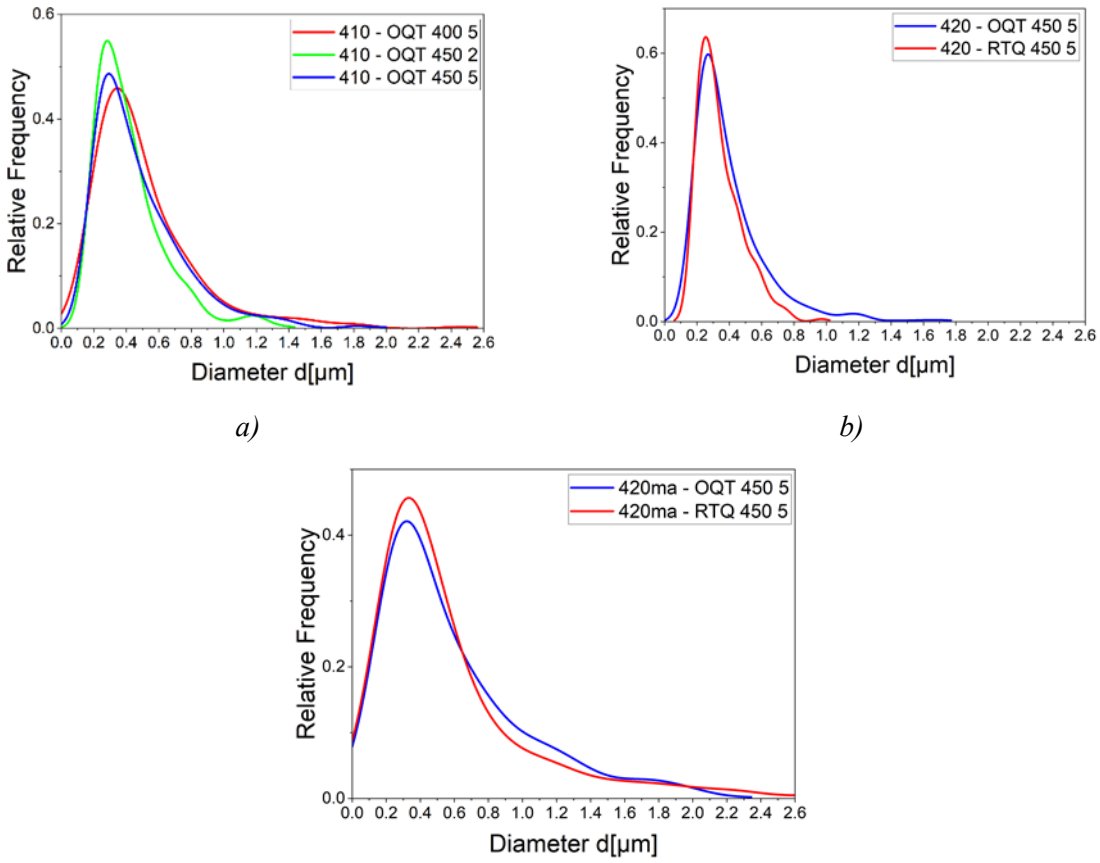

Figure 5-6. Histograms of grain size distribution for retained austenite in the Q&P-treated: a) alloy 410, b) alloy 420, and c) alloy 420ma.

There is a dramatic effect of quenching temperature on the microstructure of the 420 alloy. The local volume fraction of retained austenite measured by EBSD drops significantly from 9.7 % to 0.4 % with decreasing quenching temperature (Figure 5-4b, Table 5-2), and the formation of retained austenite grains with a size above 0.8 μm is suppressed (Figure 5-4b, Figure 5-6b). The increase of Mn content and additional microalloying by Nb and Ti (alloy 420ma, Table 3-1) benefits the volume fraction of retained austenite, which increases to 14.5–15.5 % (Table 5-2). This is related to the additional stabilization of retained austenite by Mn [79]. Also, microalloying by Nb and Ti results in the formation of nanoscale NbC and TiC particles in the alloy 420ma (Figure 5-7). They are typically formed during hot rolling of such steels and characterized by very high thermal stability [80], [81]. They have a spherical shape with the average size of 81 ± 26 nm and 43 ± 16 nm, respectively (Figure 5-7). The NbC nanoprecipitates tend to decorate TiC nanoprecipitates. Therefore, henceforth, they will be referred to as complex (Ti,Nb)C nanocarbides. According to the thermodynamic analysis carried out in the earlier works, the formation of such complex precipitates is the result of the precipitation sequence of particles, TiC followed by NbC, where a newly formed NbC particle precipitates on the habit plane of a pre-existing TiC particle [82]. The habit plane is the interface with the lowest misfit between the secondary NbC particle and the pre-existing TiC particle. The Q&P treatment parameters do not affect the morphology and size of complex (Ti,Nb)C nanoparticles.

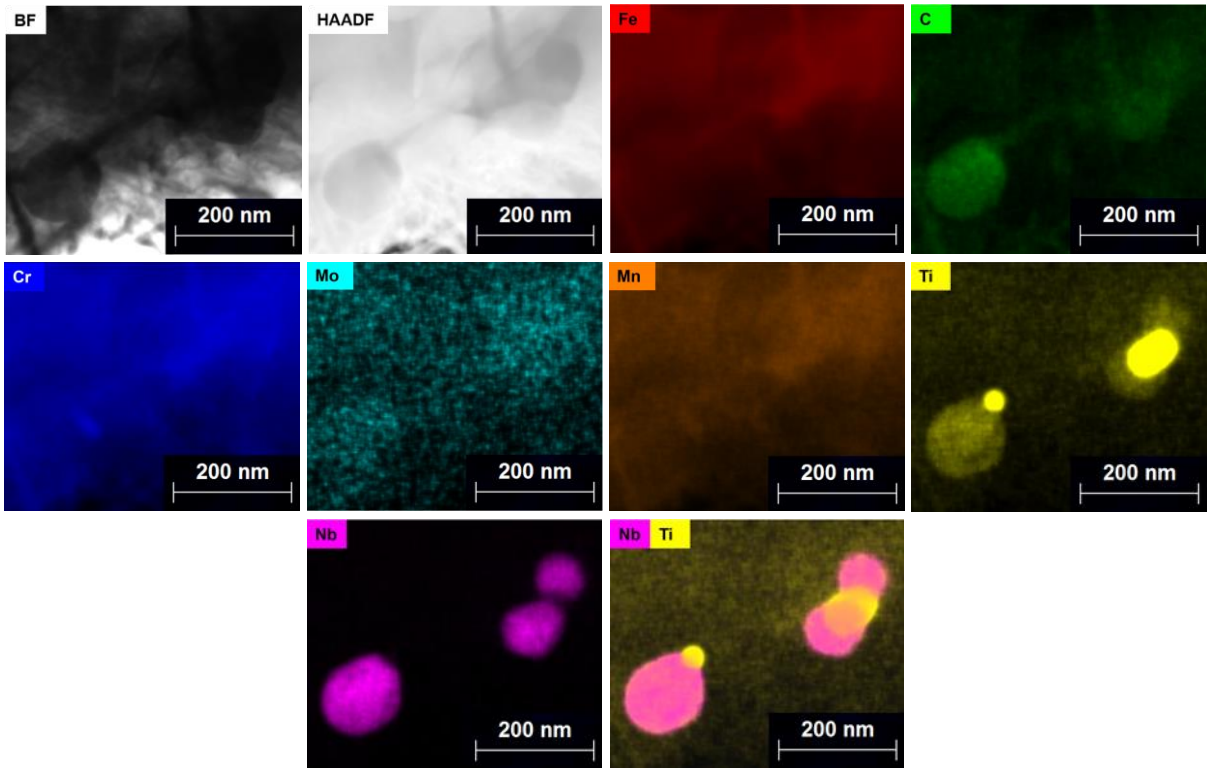

Figure 5-7. BF and HAADF TEM images with corresponding elemental maps of the sample 420ma-OQT-450-5.

It has been well known that both NbC and TiC nanocarbides effectively pin grain boundaries thus refining the microstructure during thermo-mechanical processing [80], [81]. Indeed, the prior austenite grains in the 420ma alloy are smaller (21.7 µm) compared to those in the 410 and 420 alloys (37.7 µm and 36.2 µm, respectively) (Table 5-3). The finer prior austenite grain size in the 420ma alloy results in the finer martensite packet size (Table 5-3) [83]. It should be noted that the finer prior austenite grains could be an additional factor leading to the enhanced volume fraction of retained austenite in the Q&P-treated 420ma alloy. In [51], Celada-Casero et al. demonstrated that provided the sufficient volume fraction of primary martensite, and that the partitioning conditions ensure the partitioning of all carbon to the surrounding austenite, finer prior austenite grain sizes result in a faster and more efficient carbon partitioning process than coarser microstructures through the formation of smaller and more homogeneously distributed phases during the first quench. Similar effect of finer prior austenite grain size on the volume fraction of retained austenite was also recently reported in another recent work [78].

5.1.2.1. Volume fraction of retained austenite measured using different characterization techniques

XRD and magnetometry techniques have been additionally employed to measure the volume fraction of retained austenite in the studied materials. The XRD technique provided higher fractions of retained austenite for all studied alloys compared to the EBSD method (Table 5-4). There are two main reasons for this observation. First, the interlath retained austenite grains having thickness well below the step size used in the EBSD measurements (100 nm) [84] and film-type retained austenite having a thickness less than 50 nm [85] cannot be detected by EBSD analysis. Second, using the XRD technique we measure the volume fraction of retained austenite on a larger area of ~1 mm^2, and it also includes the sub-surface volume. Meanwhile, EBSD measurements are limited to a surface area having a size of ~ 50 µm x 30 µm (Figure

5-4). It should be noted that the fractions of finest interlath retained austenite and film-like retained austenite can vary in different alloys, thus resulting in varying difference between volume fractions of retained austenite measured by XRD and EBSD. Nevertheless, there is a good correlation between the outcomes of the EBSD and XRD analyses (Table 5-4).

Table 5-4. Volume fraction of retained austenite measured by XRD and magnetometry, and comparison with the EBSD data.

Sample	Volume fractions of retained austenite [%]		
	EBSD	XRD	Magnetometry
410-OQT-400-5	6.7	15.6	19.9
410-OQT-450-2	6.7	14.6	17.9
410-OQT-450-5	9.6	17.1	12.6
420-OQT-450-5	9.7	11.3	26.6
420-RTQ-450-5	0.4	1.0	7.4
420ma-OQT-450-5	15.5	19.0	34.6
420ma-RTQ-450-5	14.5	19.5	18.8

The results from magnetometry measurements are also presented in Table 5-4. For this technique, a bulk specimen of the treated alloy is measured using a magnetometer which theoretically should provide the most comprehensive measurement of retained austenite. In this case, there is no evident correlation between the values obtained via magnetometry and the other two techniques. In most cases, the magnetometry value surpasses even the XRD value. Nevertheless, there are instances where this pattern does not hold, and the magnetometry values are lower than those obtained via XRD. Several factors could account for these discrepancies:

- Chemical composition. The presence of alloying elements has various effects on the magnetic properties of steels, and amongst them the interstitial elements (such as C) have the largest effect [86]. Oxley et al. observed a decrease of the magnetization saturation with the increase of Cr content [87].
- Grain size. The density of grain boundaries directly influences the coercive force of the steel, making it less susceptible to the magnetic field, and thus increasing the magnetization saturation [86]. The studied alloys have different prior austenite grain size (Table 5-3).

It is well known that measuring retained austenite volume fraction is a not an easy task and there is no unique technique which would provide accurate information on all the aspects (size, volume fraction, morphology, spatial distribution, etc.) [88]. One of the objectives of this work was to study the effect of plastic deformation on microstructure evolution and the crack propagation across the complex microstructure containing retained austenite, which is expected to transform within plastic zone. The EBSD technique is the only technique which provides a quantitative information on the local volume fraction of retained austenite and size of retained austenite grains. Therefore, for the consistency of this work, the outcomes of EBSD analysis are used to analyze the alloy-process-microstructure-property relationship in the studied steels.

5.1.2.2. Carbon content determination results from XRD measurements

The acquired spectra from the XRD measurements are employed to calculate the lattice parameter of the austenite by applying the Nelson-Riley equation (see Section 3.3.3). These results are compiled in Table 5-5. Using the determined lattice parameter, it is feasible to estimate the carbon content within the retained austenite using the Dyson-Holmes equation [89]. An important note to make at this stage is that the Dyson-Holmes equation is derived empirically and it has been fitted in multiple occasions [89]–[93]. In the original paper by Dyson and Holmes [90], a complete linear regression model is derived (Eq. 5.1). However, the parameters of this law are given with confidence intervals, and if they are minimized (Eq. 5.2) or maximized (Eq. 5.3), the results change drastically as compared in Table 5-6. This analysis is expanded with equations from recent articles by Van Dijk et al. [89] (Eq. 5.4), Ghosh et al. [91] (Eq. 5.5), Denand et al. [92] (Eq. 5.6), and a simplified formulation (Eq. 5.7) presented in [93].

Table 5-5. Lattice parameter of retained austenite in the GLEEBLE Q&P-treated samples.

Sample	Volume fractions of retained austenite (XRD) [%]	Lattice parameter [Å]
410-OQT-400-5	15.6	3.590
410-OQT-450-2	14.6	3.593
410-OQT-450-5	17.1	3.600
420-OQT-450-5	11.3	3.595
420-RTQ-450-5	1.0	3.601
420ma-OQT-450-5	19.0	3.592
420ma-RTQ-450-5	19.5	3.593

$$a = 3.578 + 0.033C + 0.00095Mn - 0.0002Ni + 0.0006Cr + 0.022N + 0.0056Al \quad \textit{(Eq. 5.1)}$$

$$a = 3.578 + 0.022C + 0.0008Mn - 0.00024Ni + 0.0003Cr + 0.0186N + 0.0049Al \quad \textit{(Eq. 5.2)}$$

$$a = 3.578 + 0.044C + 0.0011Mn - 0.00016Ni + 0.0009Cr + 0.0254N + 0.0063Al \quad \textit{(Eq. 5.3)}$$

$$a = 3.556 + 0.0453C + 0.00095Mn + 0.0056Al \quad \textit{(Eq. 5.4)}$$

$$a = 3.556 + 0.0453C + 0.00095Mn + 0.0006Cr + 0.0056Al \quad \textit{(Eq. 5.5)}$$

$$a = 3.5847 + 0.033C + 0.00095Mn - 0.0002Ni + 0.0006Cr + 0.0015Cu \quad \textit{(Eq. 5.6)}$$

$$a = 3.578 + 0.033C \quad \textit{(Eq. 5.7)}$$

Table 5-6. Results of carbon content determination using different equations.

Sample	(Eq. 5.1)	(Eq. 5.2)	(Eq. 5.3)	(Eq. 5.4)	(Eq. 5.5)	(Eq. 5.6)	(Eq. 5.7)
410-OQT-400-5	0.10	0.34	-0.01	0.58	0.74	-0.08	0.61
410-OQT-450-2	0.18	0.46	0.05	0.63	0.80	0.00	0.69
410-OQT-450-5	0.41	0.79	0.21	0.79	0.96	0.22	0.92
420-OQT-450-5	0.25	0.56	0.09	0.68	0.85	0.07	0.77
420-RTQ-450-5	0.42	0.82	0.22	0.81	0.98	0.24	0.94
420ma-OQT-450-5	0.09	0.34	-0.03	0.57	0.74	-0.09	0.68
420ma-RTQ-450-5	0.10	0.36	-0.02	0.57	0.75	-0.08	0.69

It is evident that the numerical results exhibit significant scatter although the general trends are maintained. Hence, the analysis available with this technique has to be viewed qualitatively rather than quantitatively. For example, in alloy 410, the carbon content in retained austenite tends to increase with the increasing partitioning temperature and time, due to the higher amount of carbon atoms diffused into retained austenite [51]. In addition, a significant drop of austenite content in the 420 alloy with the decreasing quenching temperature leads to a noticeable increase of carbon content therein. In the 420-RTQ-450-5 sample, a very high fraction of tempered martensite (i.e., a very low fraction of retained austenite) provides a significant amount of carbon to the austenite, thus resulting in the increased carbon content [51]. The exact determination of the carbon content in the austenite phase remains inconclusive with this technique.

5.1.2.3. Selection of optimum Q&P parameters for processing large sheets

Based on the results presented in this section, the partitioning parameters leading to the most optimal microstructure are a partitioning temperature of 450 °C and a partitioning time of 5 minutes. These specific parameters result in the highest fraction of retained austenite, with 9.6 % for 410-OQT-450-5, compared to 6.7 % observed in the other two conditions (Table 5-2). Furthermore, these partitioning parameters do not significantly influence the sizes of the microstructural constituents (Table 5-3).

For selection of the optimum partitioning parameters, the resulting tensile properties have to be contemplated as well. These properties are presented and discussed in Section 5.2.1. The following optimum Q&P parameters have been selected:

- **Alloy 410, OQT = 160 °C, PT = 450 °C, Pt = 5 min.** These Q&P parameters lead to the highest volume fraction of retained austenite in the material (Table 5-2). Additionally, they result in the highest combination of ultimate tensile strength and elongation to fracture (σ_{UTS} x ε_t), while ultimate tensile strength of the material (1335

MPa) remains well above the target UTS (Table 5-9). The uniform elongation of 16.5 % suggests that the elongation to fracture target will be met in full size specimens.

- **Alloy 420, OQT = 99 °C, PT = 450 °C, Pt = 5 min.** From the two studied quenching routes contemplated, this one (OQT = 99 °C) leads to the highest volume fraction of retained austenite (9.7 %, Table 5-2), ultimate tensile strength (1655 MPa), uniform elongation (18.1 %) and elongation to fracture (24.2 %, Table 5-9). The room temperature quench strategy results in a similar ultimate tensile strength (1605 MPa), although its uniform elongation is below the target (7.2 %), and thus it is discarded.
- **Alloy 420ma, RTQ = 30 °C, PT = 450 °C, Pt = 5 min.** Although the OQT condition leads to slightly higher volume fractions of retained austenite (15.5 %, Table 5-2) and uniform elongation (17.1 %, Table 5-9), the uniform elongation achieved with the room temperature quenching route is also above the target (15.2 %, Table 5-9). The ultimate tensile strength in both cases is 1524 MPa, and both of them fulfill the target. Then, this route is selected since, from an industrial and economic point of view, a room temperature quench (water quench) is more beneficial than a furnace quench (more cost-effective implementation and less energy consumed).

The defined parameters for each alloy are implemented in the Q&P treatment of the large sheets (Section 3.2.2). These cycles are all expected to lead to the targets being eventually met on the large sheets (σ_{UTS} > 1200 MPa and ε_t (50 mm gauge) > 10%).

5.1.3. Microstructure of large Q&P-treated sheets

In this section, the results of the microstructural characterization of the large Q&P-treated sheets are presented. Typical EBSD band contrast maps overlaid by corresponding IPF maps for retained austenite grains and corresponding KAM maps are shown in Figure 5-8. The microstructures of the large Q&P-treated sheets appear to be very similar to the microstructures of their GLEEBLE Q&P-treated counterparts. In all large Q&P-treated sheets, the retained austenite grains are evenly distributed over the martensitic matrix. Two morphologies of retained austenite are observed: relatively coarse blocky retained austenite having equiaxed shape with a grain size of ≥ 1 μm and finer elongated interlath-lamellar retained austenite located between martensite laths. There is no pronounced crystallographic texture of retained austenite (Figure 5-8). Its volume fraction tends to increase from 9.7 % in 410 alloy to 15.7 % in 420 alloy to 18.7 % in the 420ma alloy (Table 5-7). This observation can be related to the increasing content of austenite-stabilizing alloying elements, carbon and manganese (Table 3-1) [94], [95]. There is no significant effect of chemistry on the average grain size of retained austenite (Table 5-8).

The interior of martensite laths has nearly zero local misorientations, whereas the martensite lath boundaries show higher local misorientations of 1 – 1.5° (Figure 5-8). The non-indexed pixels (white pixels on KAM maps) correspond to prior austenite grain/packet/block boundaries. Ultra-fine non-indexed areas on the KAM maps (white pixel areas, Figure 5-8) correspond to fresh martensite, which could not be indexed due to high lattice distortion [57], [78]. Its volume fraction tends to slightly increase with the increasing content of alloying elements.

The average sizes of the microstructural constituents measured by a line interception method are listed in Table 5-8. It is seen that the microalloying by Nb and Ti noticeably reduces prior austenite grain size from 38.3 μm in alloy 410 down to 20.4 μm in alloy 420ma. The finer prior austenite grains result in finer martensite packet size (Table 5-8) [83]. This microstructural

refinement in alloy 420 ma is related to the formation of NbC and TiC nanoparticles in the grade 420ma (Figure 5-9.b), which are homogeneously distributed over the microstructure of the Q&P-treated alloy 420-ma. They have a spherical shape with average sizes of 67.4 ± 14.7 nm and 44.1 ± 18.5 nm, respectively (Figure 5-9). The NbC nanoprecipitates tend to decorate TiC nanoprecipitates, in a similar manner as observed in the GLEEBLE-treated samples (Figure 5-7). These complex (Ti,Nb)C nanocarbides effectively pin grain boundaries thus refining the microstructure during thermo-mechanical processing and austenitization [81]. In all Q&P-treated steels, elongated nanoscale Fe_3C carbides are detected. Their length is 50–250 nm and width is 10–15 nm. They are homogeneously distributed over the microstructure. TEM images (Figure 5-9.a) clearly illustrate their presence in the interior of martensite lath of the 410 alloy. These TEM images are provided by RINA Consulting – Centro Sviluppo Materiali, our collaborator.

Table 5-7. Microstructural constituents identified using EBSD analysis and their local volume fractions in the large Q&P-treated sheets.

Alloy	Retained austenite (FCC) [%]	Martensite (BCC) [%]			Non-indexed [%]
		BCC phase total	Tempered martensite	Fresh martensite	
410	9.7	79.5	75.1	4.4	10.8
420	15.7	69.5	63.4	6.1	14.8
420ma	18.7	66.6	60.6	6.0	14.7

Table 5-8. Size of the microstructural constituents in the large Q&P-treated sheets determined using EBSD analysis.

Alloy	Retained austenite	Martensite				Prior austenite grain size [μm]
		Tempered martensitic matrix			Fresh martensite size [μm]	
	Grain size [μm]	Packet size [μm]	Block size [μm]	Lath width [μm]		
410	0.7 ± 0.3	21.6 ± 11.7	3.8 ± 1.5	1.2 ± 1.2	0.50 ± 0.04	38.3 ± 2.9
420	0.9 ± 0.6	11.9 ± 4.3	3.5± 0.9	0.9 ± 0.8	0.40 ± 0.08	29.4 ± 15.7
420ma	0.8 ± 0.6	8.4 ± 1.9	2.7± 0.9	0.9 ± 0.8	0.50 ± 0.20	20.4 ± 7.0

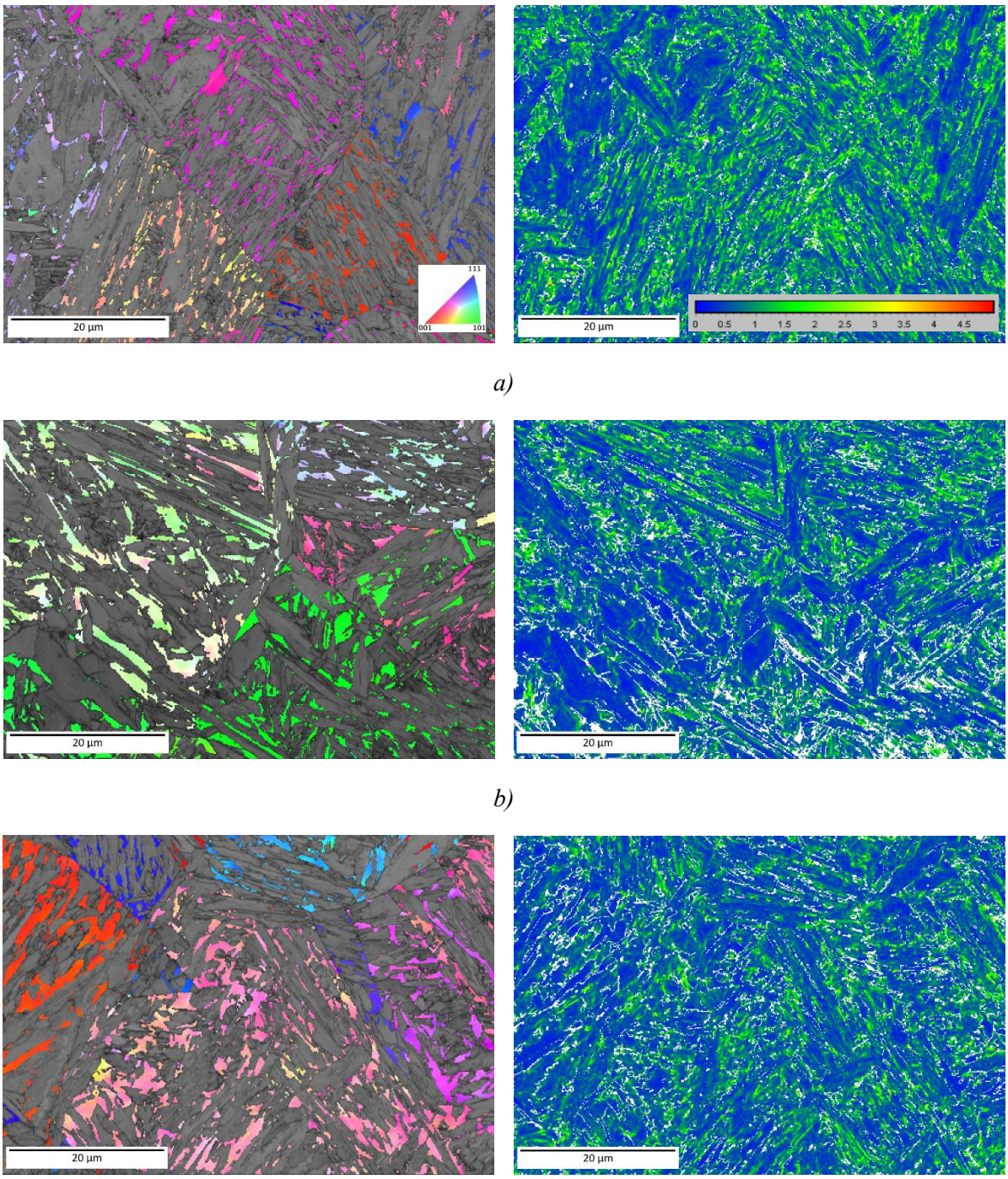

Figure 5-8. Typical microstructures of the large Q&P-treated sheets: a) alloy 410; b) alloy 420; c) alloy 420ma. Left: EBSD band contrast map overlaid by retained austenite IPF map; Right: KAM map of the corresponding area.

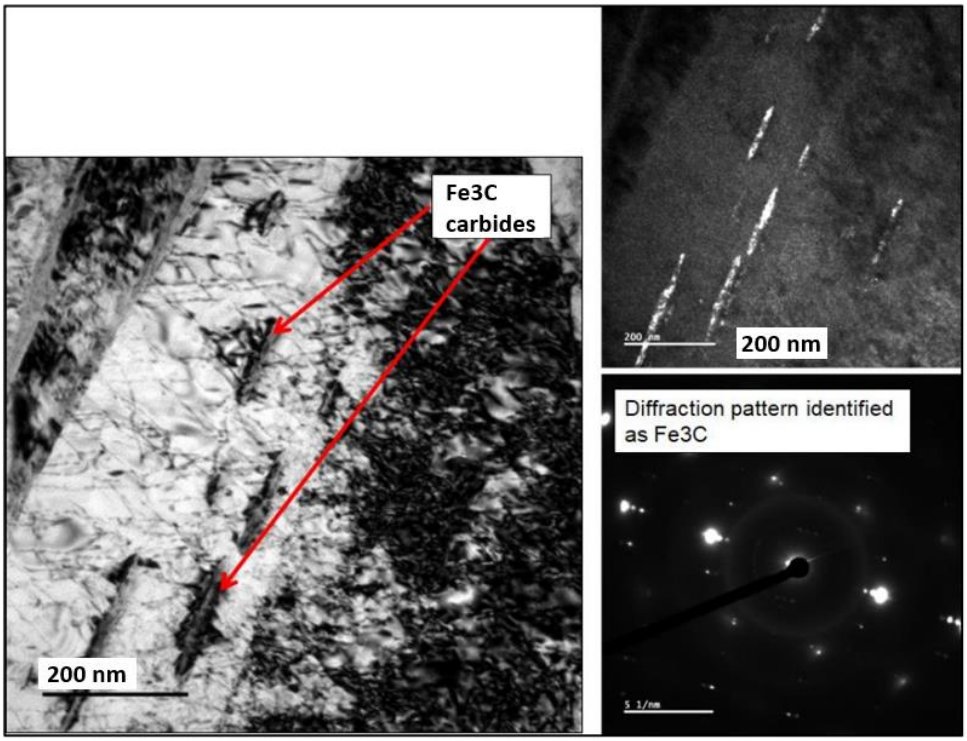

a)

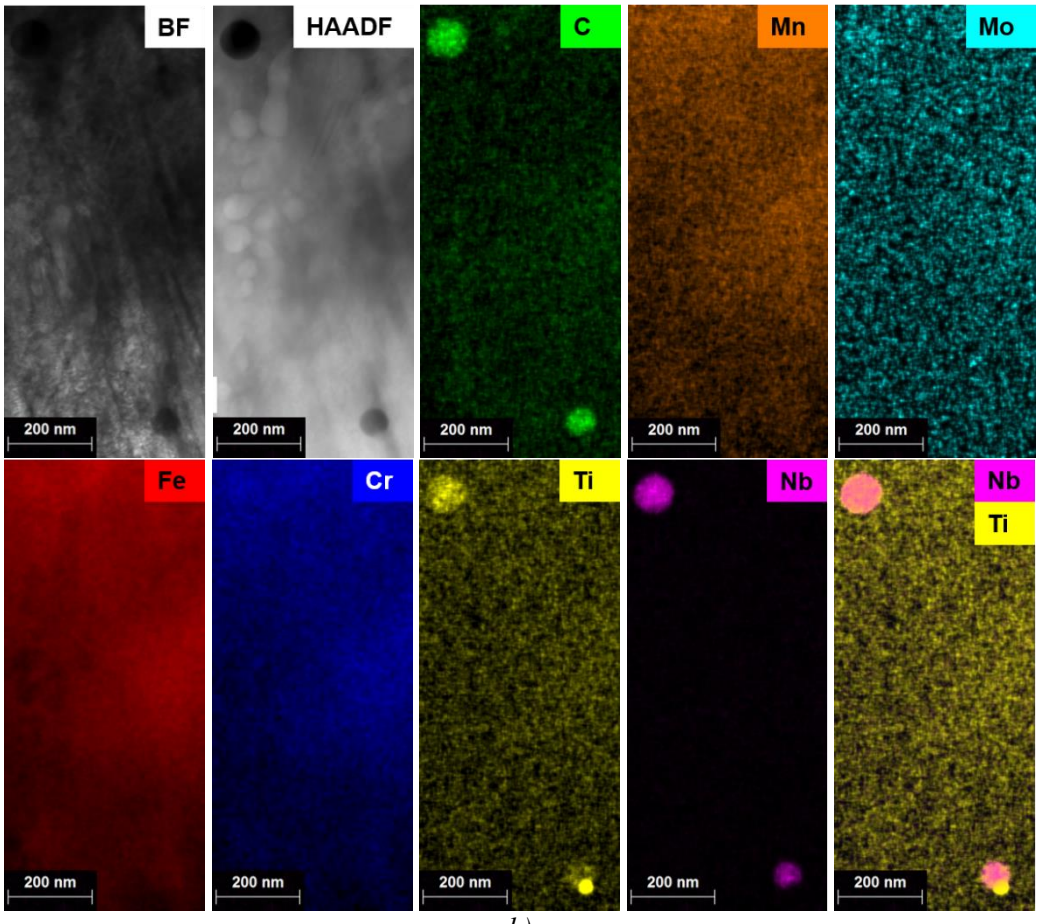

b)

Figure 5-9. a) Appearance of Fe_3C nanoscale carbides in the Q&P-treated 410 steel; b) appearance of complex (Ti,Nb)C nanocarbides in the large Q&P-treated sheets of 420ma alloy.

5.1.4. Conclusions to Section 5.1

From the microstructural characterization of the Q&P-treated martensitic stainless steels the following conclusions can be drawn:

- Alloy chemistry and Q&P parameters (quenching temperature, partitioning temperature and partitioning time) significantly affect the microstructure of the Q&P-treated martensitic stainless steels.
- The volume fraction of retained austenite tends to increase with increasing partitioning temperature (from 400 °C to 450 °C) and partitioning time (from 2 min to 5 min) in alloy 410.
- The volume fraction of retained austenite tends to increase with the increasing C content (from 0.2 wt.% to 0.3 wt.%) and Mn content (from 0.7 wt.% to 3 wt.%) from 9.7 % (alloy 410) to 18.7 % (alloy 420ma) in the GLEEBLE-treated samples.
- Microalloying with Nb and Ti noticeably reduces the prior austenite grain size due to the formation of complex nanoscale (Ti,Nb)C precipitates that suppress grain growth during austenitization. The average martensite packet and block size correlate with the prior austenite grain size in the studied steels.
- Based on the outcomes of the physical simulation, the following optimum Q&P parameters were selected:
    - QT = 160 °C, PT = 450 °C, Pt = 5 min for alloy 410;
    - QT = 90 °C, PT = 450 °C, Pt = 5 min for alloy 420;
    - QT = 30 °C, PT = 450 °C, Pt = 5 min for alloy 420 ma.
- Physical simulation enables the determination of optimum Q&P parameters and is able to predict the microstructure of the samples processed on large scale. Minor deviations in the predictions can be related to inability to perfectly control Q&P treatment parameters (heating rates, cooling rates) during the processing of large sheets.
- The existing methodologies to estimate the carbon content in retained austenite of Q&P-treated martensitic stainless steels using XRD results are not reliable. A better experimental methodology needs to be developed.

5.2. Effect of Q&P treatment on tensile properties

5.2.1. Tensile behavior of sub-size samples from physical simulation experiments

5.2.1.1. Tensile properties of sub-size specimens from physical simulation experiments

Figure 5-10 presents engineering stress – engineering strain curves from tensile testing of the Q&P-treated alloys using the GLEEBLE 3800 system (Section 3.2.1). The basic tensile mechanical properties and strain hardening exponent n were determined from the curves and summarized in Table 5-9. The following observations can be noted.

All Q&P-treated alloys show ultimate tensile strength (σ_{UTS}) well above 1300 MPa and elongation to fracture above 19 %. In alloy 410, the yield strength ($\sigma_{0.2}$), uniform elongation

(ε_u) and elongation to fracture (ε_t) tend to increase with the increasing partitioning temperature and time, whereas ultimate tensile strength and strain hardening exponent show an opposite trend. The Q&P-treated alloy 420 shows better mechanical strength compared to the 410 alloy. There is no significant effect of quenching temperature on the strength properties of the 420 alloy, whereas its elongation to fracture and average n-values decrease, and uniform elongation dramatically drops with the decreasing quenching temperature. Despite significant strain hardening at the early stage of plastic deformation of the 420-RQT-450-5 (Figure 5-10), the necking onsets at the plastic strain of 7.2 %. The microalloyed alloy 420ma shows intermediate σ_{UTS} value (1524 MPa) compared to other two alloys, combined with sufficient uniform elongation values (15.2 – 17.1 %). The yield strength of the 420ma alloy increases with decreasing quenching temperature (OQT vs. RTQ), whereas its elongation to fracture exhibits

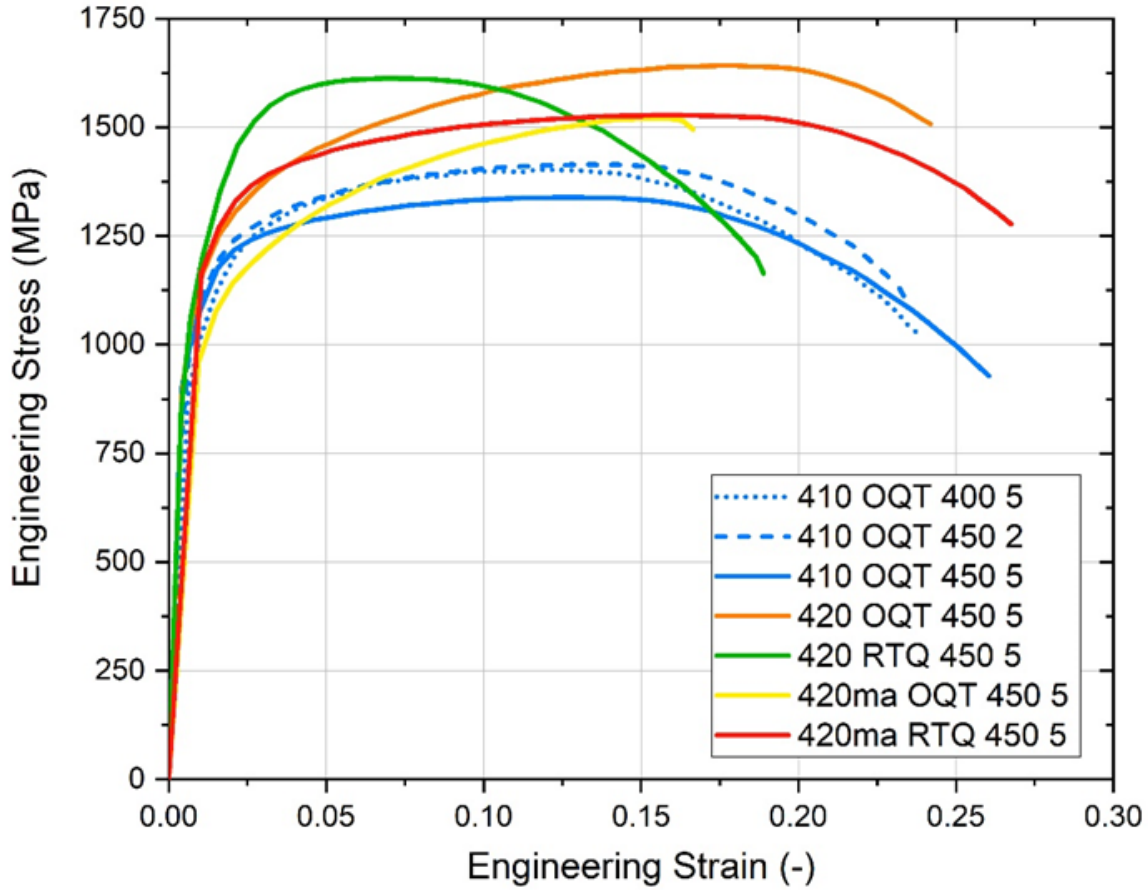

Figure 5-10. Typical engineering stress – engineering strain curves for the Q&P-treated alloys in the GLEEBLE 3800 system.

the opposite trend.

Table 5-9. Basic tensile mechanical properties of the GLEEBLE Q&P-treated martensitic stainless steels and their conventional quenched and tempered counterparts.

Alloy	Condition	$\sigma_{0.2}$ [MPa]	σ_{UTS} [MPa]	ε_u [%]	ε_t [%]	n	Ref.
410	410-OQT-400-5	880	1403	11	23.3	0.13	This work
	410-OQT-450-2	950	1388	12.5	25.6	0.11	
	410-OQT-450-5	1007	1335	16.5	28.4	0.10	
420	420-OQT-450-5	1120	1655	18.1	24.2	0.15	
	420-RTQ-450-5	1152	1605	7.2	19.4	0.12	
420ma	420ma-OQT-450-5	943	1524	17.1	19.3	0.18	
	420ma-RTQ-450-5	1059	1524	15.2	26.5	0.12	
AISI 410	Quenched and tempered at relatively low temperature	620	830	-	12	-	ASTM standard [22]
AISI 410	Quenched and tempered at relatively high temperature	550	690	-	12	-	
AISI 420	Quenched and tempered at relatively low temperature	1360	1600	-	12	-	
AISI 420	Quenched and tempered at relatively high temperature	810	1035	-	18	-	

Data on mechanical properties of conventional quenched and tempered martensitic stainless steels have also been added in Table 5-9 for comparison. It is seen that the Q&P-processed 410 alloy shows much better strength and ductility compared to the conventional quenched and tempered 410 alloy. Meanwhile, both GLEEBLE Q&P-treated 420 and 420ma alloys demonstrate similar level of strength as the conventional counterpart quenched and tempered at low temperatures.

The results compiled in Table 5-9 demonstrate a significant impact of the Q&P-treated microstructure on the tensile mechanical properties. The mechanical behavior of martensitic stainless steels containing retained austenite is determined by the interplay of several factors, which are discussed below.

It is well known, that the volume fraction, size and stability of retained austenite grains play a key role in the mechanical behavior of AHSS [28]–[30], [79], [94]. A positive effect of the enhanced volume fraction of retained austenite (Table 5-2) on the uniform elongation values (Table 5-9) can be noted for all studied GLEEBLE Q&P-treated alloys. For example, the

uniform elongation of the alloy 420 increases from 7.2 % to 18.1 % with the increasing local volume fraction of retained austenite from 0.4 % to 9.7 % (Table 5-2, Table 5-4). Earlier *in situ* studies of strain partitioning between phases in carbon steels showed that blocky retained austenite accommodates much higher local plastic strains compared to the martensitic matrix before its transformation [96], [97]. Transformation of plastically deformed metastable blocky and interlath retained austenite grains under applied loading provides additional ductility due to the TRIP effect [79], [94], as shown in Section 5.2.1.2 below.

5.2.1.2. Effect of tensile deformation on the microstructure of the GLEEBLE Q&P-treated sub-size samples

EBSD analysis of the GLEEBLE Q&P-treated samples after tensile testing of the five selected conditions revealed dramatic reduction of the volume fraction of retained austenite in all steels (Figure 5-11, Table 5-10). Histograms of blocky and interlath retained austenite size distribution before and after tensile deformation of the selected conditions are compared in Figure 5-12. It is seen that the austenite grains remaining after plastic deformation are much finer compared to those present in the microstructure before testing. Most blocky and larger interlath retained austenite grains transformed into martensite (Table 5-10). This is related to the higher stability of the fine interlath retained austenite grains [79]. Carbon content in retained austenite grains plays another important role. The higher is the carbon content, the higher is the stability of retained austenite [79]. From Table 5-6, it is seen that the increasing partitioning temperature and partitioning time in the alloy 410 leads to the higher carbon content in retained austenite [98], which, in turn, promotes its stability during plastic deformation [79]. Gradual transformation of retained austenite during tensile deformation maintains steady strain hardening, thus delaying the onset of necking [99], [100].

It is known that metastable retained austenite grains with different crystallographic orientations have different stability during uniaxial tensile loading [79], [101]. However, from the IPF maps, it is seen that the remaining retained austenite grains do not show any preferred crystallographic orientation (Figure 5-11c). It can be suggested that the stress partitioning between martensite and austenite along with the constraining effect of the martensitic lath minimizes this effect. Indeed, a number of articles reported that crystallographic orientation plays a secondary role in affecting the austenite stability compared to its grain size [102] and chemical composition [103].

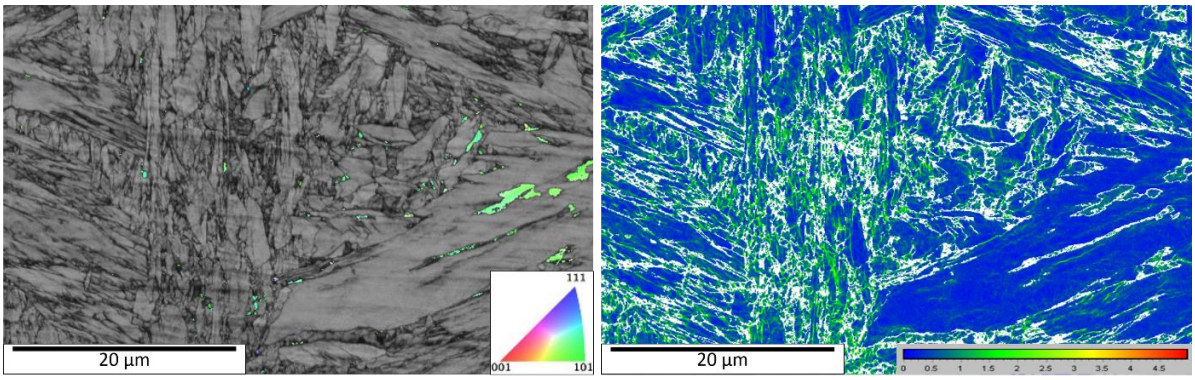

Retained austenite in IPF Z overlay *KAM*

a) 410-OQT-450-5 (Average local volume fraction of retained austenite, 9.6 % – After tensile test, 0.8 %)

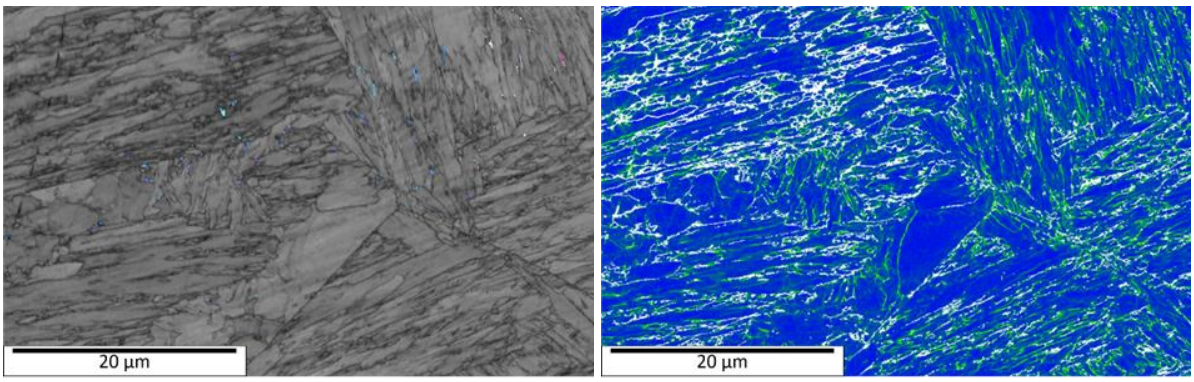

Retained austenite in IPF Z overlay *KAM*

b) 420-RTQ-450-5 (Lowest local volume fraction of retained austenite, 0.4 %) – After tensile test, 0.2 %)

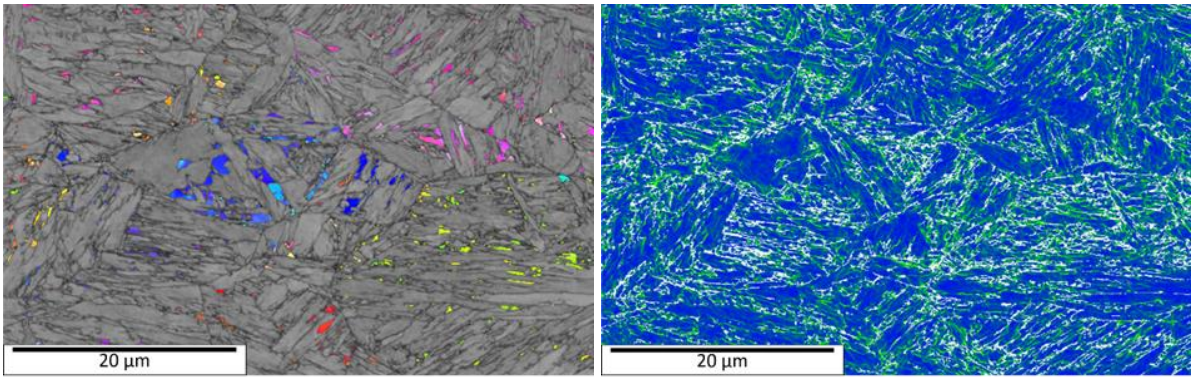

Retained austenite in IPF Z overlay *KAM*

c) 420ma-OQT-450-5 (Highest local volume fraction of retained austenite, 15.5 % – After tensile test, 2.9 %)

Figure 5-11. Typical microstructures of the GLEEBLE Q&P-treated samples after tensile testing. Left: EBSD band contrast map overlaid by retained austenite IPF map; Right: KAM map of the corresponding area.

Despite the 420ma alloy has the higher Mn content and is additionally microalloyed by Nb and Ti, its strength is surprisingly lower compared to the alloy 420 independently on the applied quenching temperature (Table 5-9). This observation can be rationalized based on the much higher volume fraction of blocky retained austenite in 420ma alloy compared to the 420 alloy (Table 5-10). The 420ma-RTQ-450-5 sample contains 10.3 % of blocky retained austenite, whereas the latter is absent in the 420-RTQ-450-5 sample (Table 5-10). Plastic deformation begins with localized plastic flow in the soft blocky retained austenite grains, spreading to martensitic matrix due to dislocation hardening and/or austenite-martensite phase transformation at the later stage of plastic deformation [96], [97]. An increasing fraction of the blocky retained austenite in the microstructure of the 420ma alloy leads to softening of the material and to the lower $\sigma_{0.2}$ and σ_{UTS} values. Meanwhile, the complex (Ti,Nb)C nanocarbides do not provide significant strengthening effect [104].

There is a significant body of experimental research showing the relationship between microstructural parameters of the martensite and mechanical properties. The martensite packet and block sizes play a key role in controlling yield strength and ductile-brittle transition temperature (DBTT) [105]. The finer it is, the higher the yield strength and the lower the DBTT are. This effect, however, cannot be analyzed in our steels due to the minor variation in martensite packet and block sizes with Q&P parameters in the given alloy (Table 5-3).

The ability of the martensitic matrix to accumulate plastic deformation without its localization is an important factor determining ductility of the Q&P-treated steels [78], [106]. Qualitative analysis of the KAM maps before (Figure 5-4) and after tensile deformation (Figure 5-11) clearly shows increased misorientations in both the martensitic matrix and remaining retained austenite grains of the deformed material, which indicates high density of geometrically necessary dislocations (GNDs) accumulated in the microstructure [107]. Also, the higher fraction of fresh martensite in the deformed material further increases the fraction of the non-indexed pixels. Histograms of the local misorientation distribution in the Q&P-treated steels before and after tensile deformation are compared in Figure 5-13. It is clearly seen that plastic deformation shifts the histograms towards higher misorientation values. This shift is especially pronounced in the 420ma alloy (Figure 5-13d,e) showing the highest uniform elongation values (Table 5-9). On the contrary, no increase in misorientation values is demonstrated by the 420-RTQ-450-5 alloy (Figure 5-13c) which has the lowest uniform elongation (Table 5-9).

Table 5-10. Volume fraction (V_{total}^{RA}) and grain size (d_{total}^{RA}) of retained austenite before and after tensile deformation of the selected conditions. Data on volume fraction and grain size of blocky retained austenite (V_{blocky}^{RA} and d_{blocky}^{RA}, respectively) and interlath retained austenite (V_{il}^{RA} and d_{il}^{RA}, respectively) are also provided.

	Before testing						After testing					
	Volume fraction of retained austenite [%]			Grain size of retained austenite [μm]			Volume fraction of retained austenite [%]			Grain size of retained austenite [μm]		
Sample	V_{total}^{RA}	V_{blocky}^{RA}	V_{il}^{RA}	d_{total}^{RA}	d_{blocky}^{RA}	d_{il}^{RA}	f_{total}^{RA}	f_{blocky}^{RA}	f_{il}^{RA}	d_{total}^{RA}	d_{blocky}^{RA}	d_{il}^{RA}
410-OQT-450-5	9.6	3.0	6.6	0.7 ± 0.3	1.3 ± 0.2	0.4 ± 0.2	0.8	0.5	0.3	0.4 ± 0.3	1.6 ± 0.7	0.3 ± 0.2
420-OQT-450-5	9.7	2.5	7.2	0.7 ± 0.4	1.3 ± 0.1	0.4 ± 0.2	3.8	0.6	3.2	0.4 ± 0.2	1.3 ± 0.1	0.4 ± 0.2
420-RTQ-450-5	0.4	0	0.4	0.5 ± 0.1	-	0.5 ± 0.1	0.2	0	0.2	0.3 ± 0.1	-	0.3 ± 0.1
420ma-OQT-450-5	15.5	10.8	4.7	0.8 ± 0.5	1.5 ± 0.6	0.4 ± 0.2	2.9	0.6	2.3	0.4 ± 0.2	1.2 ± 0.2	0.3 ± 0.2
420ma-RTQ-450-5	14.5	10.3	4.2	0.8 ± 0.5	1.6 ± 0.6	0.4 ± 0.2	1.5	0.1	1.4	0.4 ± 0.2	1.3	0.4 ± 0.2

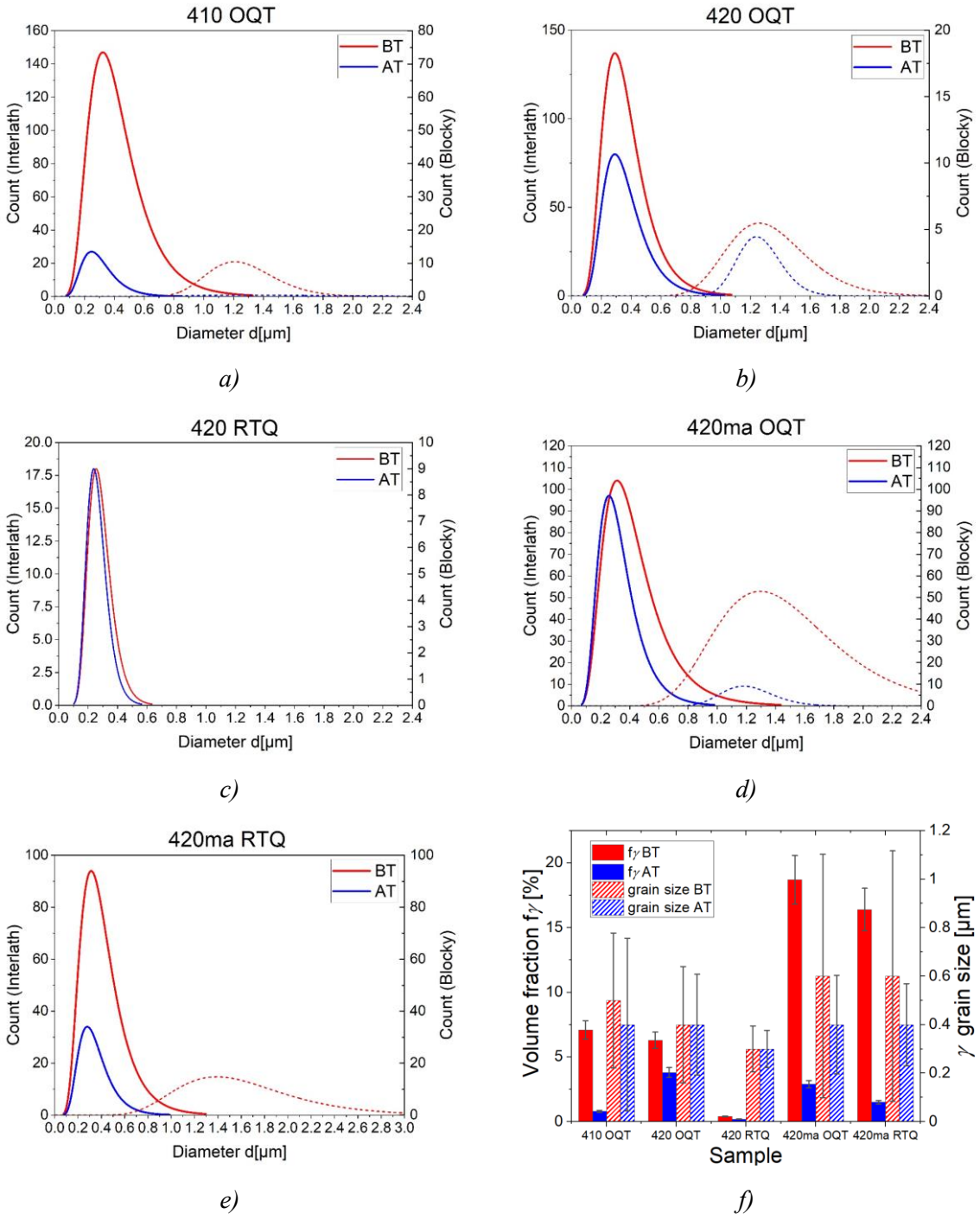

Figure 5-12. Histograms of the size distribution of blocky retained austenite (dashed lines) and interlath retained austenite (solid lines) before testing (BT) and after testing (AT) of GLEEBLE Q&P-treated samples: a) 410-OQT-450-5 alloy, b) 420-OQT-450-5 alloy, c) 420-RTQ-450-5 alloy, d) 420ma-OQT-450-5 alloy, e) 420ma-RTQ-450-5 alloy; f) a comparison of total volume fraction (f_γ) and grain size of retained austenite before testing (BT) and after testing (AT) in all studied samples.

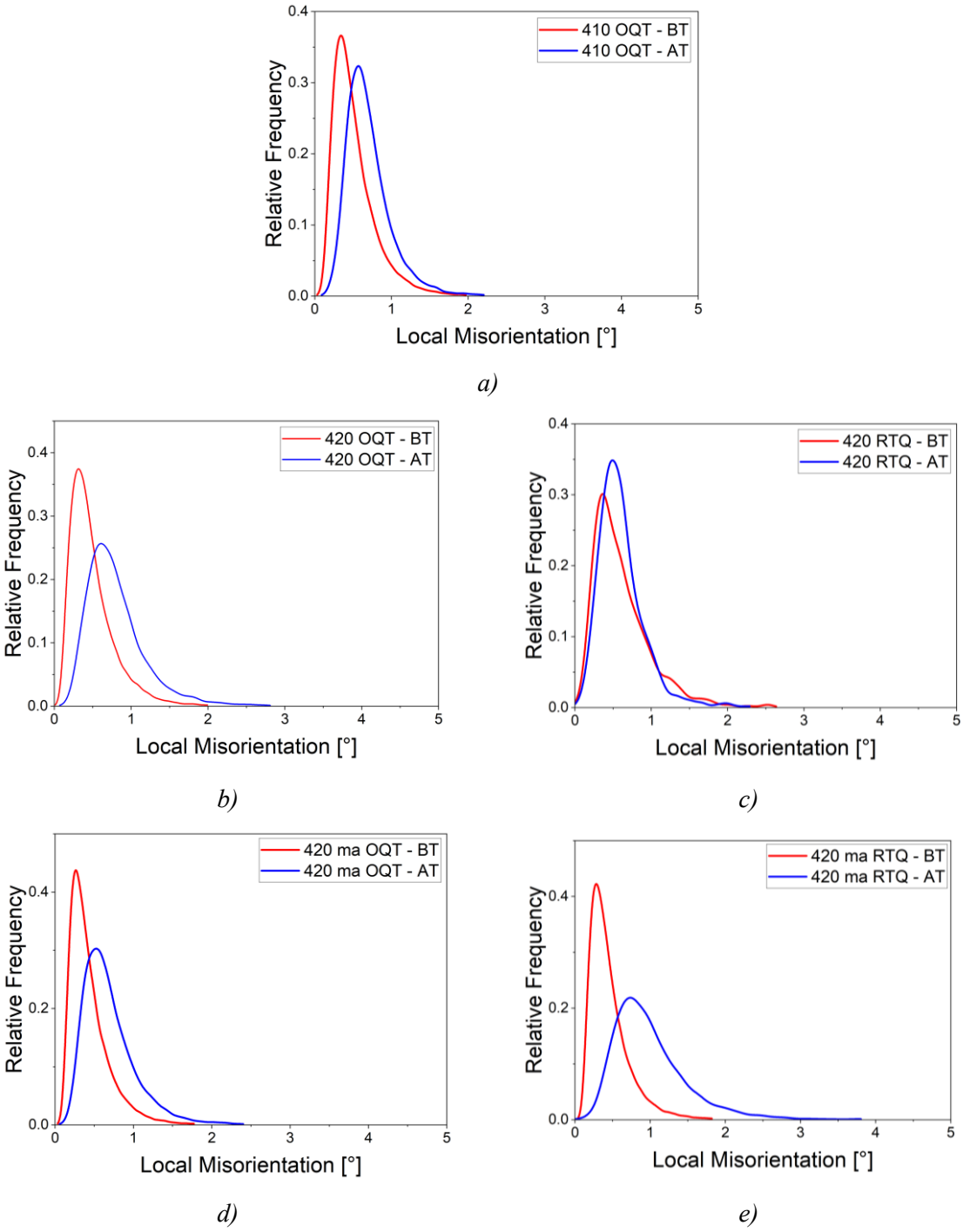

Figure 5-13. Histograms of the local misorientation distribution before testing (BT) and after testing (AT) of GLEEBLE Q&P-treated samples: a) 410-OQT-450-5 alloy; b) 420-OQT-450-5 alloy; c) 420-RTQ-450-5 alloy; d) 420ma-OQT-450-5 alloy; e) 420ma-RTQ-450-5 alloy.

5.2.2. Tensile behavior of large Q&P-treated sheets

Standard tensile specimens are machined from the large sheets produced by Q&P treatment with optimum parameters determined in Section 5.1.2.3. Table 5-11 summarizes the tensile properties measured for the studied steel grades. All alloys exhibit a high strength with an ultimate tensile strength (σ_{UTS}) value above 1200 MPa and sufficient tensile ductility with elongation to fracture values above 10%. The optimal combination of tensile strength and ductility is shown by the 420 alloy. Despite having a higher Mn content (Table 3-1) and the presence of complex (Ti,Nb)C nanocarbides (Figure 5-9), the 420ma alloy shows tensile properties similar to those of the 420 alloy. Earlier studies have shown that the strengthening effect of TiC and NbC nanocarbides is very low [108]. Additionally, the 420ma alloy shows a higher volume fraction of retained austenite and, particularly, blocky retained austenite compared to the 420 alloy (Figure 5-8b-c, Table 5-7), which provides an additional softening effect [104].

Table 5-11. Data from tensile testing of the standard samples of the Q&P-treated large sheets.

Material	Tensile testing		
	$\sigma_{0.2}$ [MPa]	σ_{UTS} [MPa]	ε_t [%]
410	936 ± 3	1276 ± 20	11.4 ± 2.4
420	1089 ± 11	1472 ± 43	14.0 ± 1.3
420ma	1082 ± 46	1451 ± 62	10.3 ± 0.7

Upon comparing these results with the tensile properties measured in the sub-size specimens machined from the GLEEBLE-treated samples under the same conditions (Table 5-9), a slight decrease in the yield strength and ultimate tensile strength can be observed in the larger geometry samples. Most notably, the elongation to fracture (ε_t) experiences a significant reduction in these larger samples. These observations can be rationalized based on:

- The size and volume fractions of the microstructural constituents in the GLEEBLE-treated samples and large processed sheets are somewhat different (volume fractions: Table 5-2 vs Table 5-7; sizes: Table 5-3 vs Table 5-8). This is related to the fact that the heat treatment parameters (heating and cooling rates, austenitization and quenching temperatures) cannot be precisely controlled during heat treatment of large sheets, as it can be done in the GLEEBLE system.
- It is well known that size effect can play a significant role in the mechanical behavior. Particularly, sub-size samples generally tend to demonstrate higher ductility compared to standard large samples .

5.2.3. Conclusions to Section 5.2

From the results obtained from tensile testing of the Q&P-treated martensitic stainless steels, the following conclusions can be drawn:

- The Q&P-treated martensitic stainless steels show a good combination of enhanced strength and sufficient tensile ductility (for GLEEBLE Q&P-treated sub-size tensile

samples σ_{UTS} > 1300 MPa and ε_t > 18 %; and for large Q&P-treated sheets and standard tensile samples, σ_{UTS} > 1200 MPa and ε_t > 10 %).

- Optimum Q&P parameters lead even to better combinations, such as σ_{UTS} = 1472 MPa and ε_t = 14.0 % (large Q&P-treated sheets and standard tensile samples of 420 alloy).
- Standard tensile samples from large Q&P-treated sheets tend to show lower strength and ductility compared to sub-size tensile samples from GLEEBLE Q&P-treated coupons due to lesser precision in control of Q&P parameters during processing large sheets resulting in somewhat different microstructure and size effect.
- In all studied alloys, the uniform elongation increases with the increasing volume fraction of retained austenite due to the TRIP effect. The majority of coarser blocky retained austenite grains transform to martensite during plastic deformation, whereas fine interlath retained austenite grains tend to remain in the microstructure due to their higher stability.
- EBSD analysis did not reveal any important role of crystallographic orientation in transformation stability of retained austenite during uniaxial tensile loading. Significant increase of the local misorientation values in KAM maps of the deformed samples indicates high ability of tempered martensitic matrix to accumulate plastic deformation.
- Q&P-treated studied materials show similar or better tensile behavior compared to their quenched and tempered counterparts due to high volume fraction of retained austenite and TRIP effect during plastic deformation.

5.3. High-cycle fatigue behavior of Q&P-treated large sheets

This section focuses on the characterization of the fatigue behavior of large Q&P-treated sheets. Samples from the Q&P-treated alloys 410, 420 and 420ma underwent high-cycle fatigue testing to determine their fatigue limits and the underlying mechanisms governing their cyclic behavior. Additionally, an EBSD analysis was conducted on samples from alloy 420ma to study the characteristics of fatigue crack growth.

5.3.1. Fatigue performance

The S-N curves obtained from high-cycle fatigue testing of the studied materials are presented in Figure 5-14. The experimental points for the three tested alloys overlap above 440 MPa of stress amplitude. The number of cycles that the sample can endure tends to increase with decreasing stress amplitude. The S-N curves become horizontal after 10^7 cycles, which is referred to as the material's fatigue limit σ_f [109]. Alloy 420ma presents the lowest fatigue limit at the stress amplitude σ_a = 270 MPa. Slightly better results are shown by alloy 410, with a fatigue limit of 300 MPa. The best fatigue limit is achieved for the alloy 420ma, reaching a fatigue limit of 320 MPa.

As it is common with fatigue testing, the results exhibit noticeable scatter at any given stress amplitude. As an illustrative case, two samples of alloy 410 tested at σ_a= 300 MPa lasted for a different number of cycles. One of them reached the fatigue limit ($1.2\text{x}10^7$ cycles), while the other one only endured for $1.6\text{x}10^5$ cycles (marked in Figure 5-14 by a red cross). SEM analysis of the fracture surface from this prematurely broken sample reveals fatigue crack initiation at a surface rolling defect. Such points are excluded from further consideration.

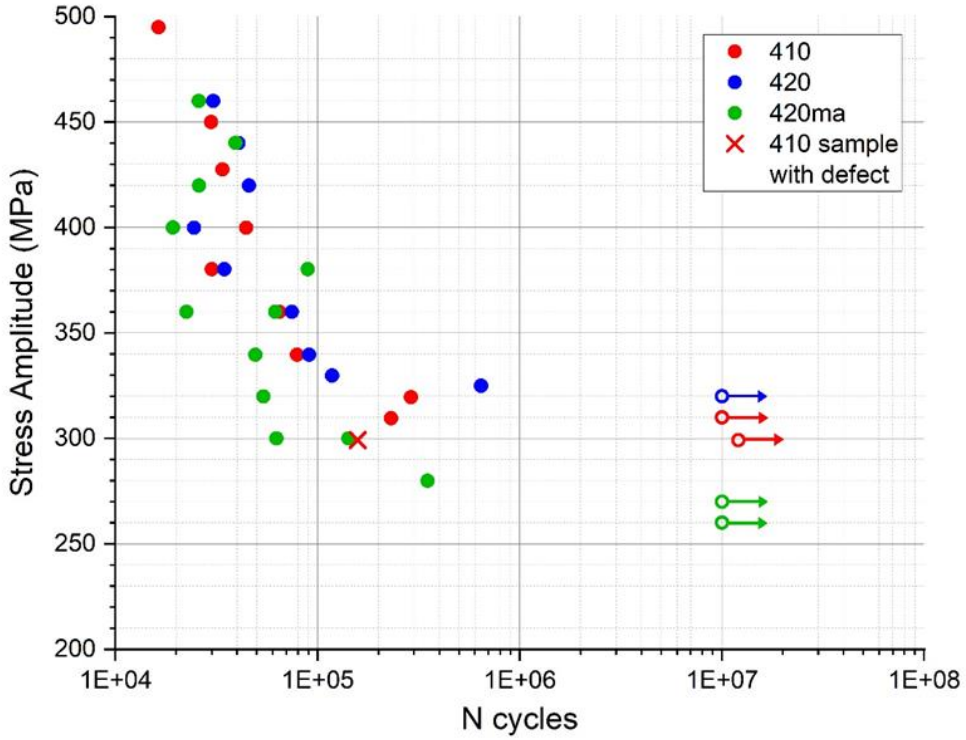

Figure 5-14. The S-N curves obtained from high-cycle fatigue testing of the Q&P-treated large sheets. One sample with fatigue crack initiated at surface rolling defects is marked by a cross (x).

Analyzing the results presented in Figure 5-14, the best fatigue limit σ_f is observed in alloy 420 (320 MPa), followed by alloy 410 (300 MPa) and then alloy 420ma (270 MPa). However, the fatigue limit is usually considered as a ratio with the ultimate tensile strength (σ_f/σ_{UTS}), which is proportional to $\sigma_{max}/\sigma_{UTS}$ when the material is tested with the same R. Recalling the results from tensile testing of standard-size specimens (from Section 5.2.2), Table 5-12 compiles the data to facilitate a comparison. Based on these results, the highest σ_f/σ_{UTS} ratio is achieved by alloy 410 (0.24), followed by alloy 420 (0.22) and lastly alloy 420ma (0.19).

Table 5-12. Data from tensile and fatigue testing of Q&P-treated martensitic stainless steels.

Material	Tensile testing	Fatigue testing		
	σ_{UTS} [MPa]	σ_f [MPa]	$\frac{\sigma_f}{\sigma_{UTS}}$	$\frac{\sigma_{max}}{\sigma_{UTS}}$
410	1276	300	0.24	0.54
420	1472	320	0.22	0.48
420ma	1451	270	0.19	0.41

The diverse fatigue performance of these materials can be attributed to their highly complex microstructures, characterized by a tempered (softened) martensitic matrix with a hierarchical substructure, fresh (hard) martensite and retained austenite, as described in Section 5.1.3. Furthermore, the variations in volume fraction, morphology, size and mechanical stability of these microstructural components among the alloys (Table 5-7, Table 5-8 and Table 5-10) significantly hinders the establishment of a direct correlation between high-cycle fatigue performance and individual microstructural characteristics. Nevertheless, it can be suggested

that the optimal performance of alloy 410 is due to the interplay of several of these microstructural factors. First, this alloy has the largest martensite packets and blocks, leading to the lowest volume fraction of martensite packet and block boundaries acting as sites for the fatigue crack initiation (Table 5-8) [110]. Second, it demonstrates the lowest volume fraction of brittle fresh martensite (Table 5-7), which may promote fatigue crack initiation.

As is well known, fatigue properties strongly depend on testing conditions, including the type of loading (e.g., tensile/compressive, torsional), the testing frequency, the stress ratio applied, as well as the surface quality [111]. Even small changes in test or specimen conditions can significantly affect fatigue behavior. The variability of fatigue testing methods and testing parameters used in the literature makes it difficult to compare the results from different studies. Nevertheless, in Table 5-13, the outcomes of the present study are compared with the earlier results of other authors from axial fatigue testing of martensitic stainless steels with stress ratios in the range of R = 0 – 0.5 [112]–[114]. A noticeable difference in the σ_f, σ_f/σ_{UTS} and $\sigma_{max}/\sigma_{UTS}$ values of the studied Q&P-treated alloys and conventional martensitic stainless steels can be rationalized based on the above explanation. The fatigue limit and σ_f/σ_{UTS} values of the Q&P-treated steels are higher compared to those of their counterparts tested with the higher stress ratio R, whereas the $\sigma_{max}/\sigma_{UTS}$ value shows an opposite trend. However, all three parameters present similar values when compared to the conventional martensitic stainless steel SS420 tested with similar R [114]. Overall, it can be concluded that the fatigue performance of the Q&P-treated martensitic stainless steels is comparable to that reported for conventional martensitic stainless steels.

Table 5-13. Comparison of the fatigue limit data for martensitic stainless steels.

Material	σ_{UTS} [MPa]	Fatigue testing parameters	σ_f [MPa]	σ_a [MPa]	$\frac{\sigma_f}{\sigma_{UTS}}$	$\frac{\sigma_{max}}{\sigma_{UTS}}$	Reference
410	1276	R=0.1	300	667	0.24	0.54	This work
420	1472	R=0.1	320	711	0.22	0.48	This work
420ma	1451	R=0.1	270	600	0.19	0.41	This work
AISI 422	880	R=0.5, stepped loading	132.1	528.4	0.15	0.60	[112]
X4CRNIMO16-5-1	850	R=0.5, stepped loading	151.7	606.8	0.18	0.71	[112]
A182F6NM	650	R=0.5, stepped loading	138.9	555.6	0.21	0.85	[112]
17-4 PH	1365	R=0.5, stepped loading	205	820	0.15	0.60	[112]
X20CrMoVI21	-	R=0	~320	-	-	-	[113]
SS 420	1515	R=0.1	306	680	0.20	0.45	[114]

5.3.2. Analysis of mechanisms governing fatigue behavior

The fatigue fracture surfaces of the broken samples are thoroughly analyzed. As is well known, there are three stages of fatigue failure: crack initiation, stable crack propagation and unstable crack growth followed by rupture [111]. The areas corresponding to each stage can be easily recognized in all analyzed samples. In the vast majority of samples, regardless of the alloy and applied stress amplitude, the fatigue cracks form at the sample surface by transgranular cracking (i.e. through prior austenite grains), and the morphology of their fatigue fracture surfaces looks very similar. Figure 5-15 presents SEM images of the fatigue crack initiation and propagation areas of the 410 alloy tested with σ_a = 320 MPa (289263 cycles to failure). The fatigue crack initiation area is marked by a white arrow (Figure 5-15a). Its size is approximately 30 μm (Figure 5-15b). Figure 5-16 illustrates the only case of fatigue crack formation via intergranular cracking observed in the 420ma alloy tested with the stress amplitude σ_a = 300 MPa (62619 cycles to failure). Grain boundaries can be easily seen, and grain size matches well with the prior austenite grain size of the 420ma alloy (Table 5-8).

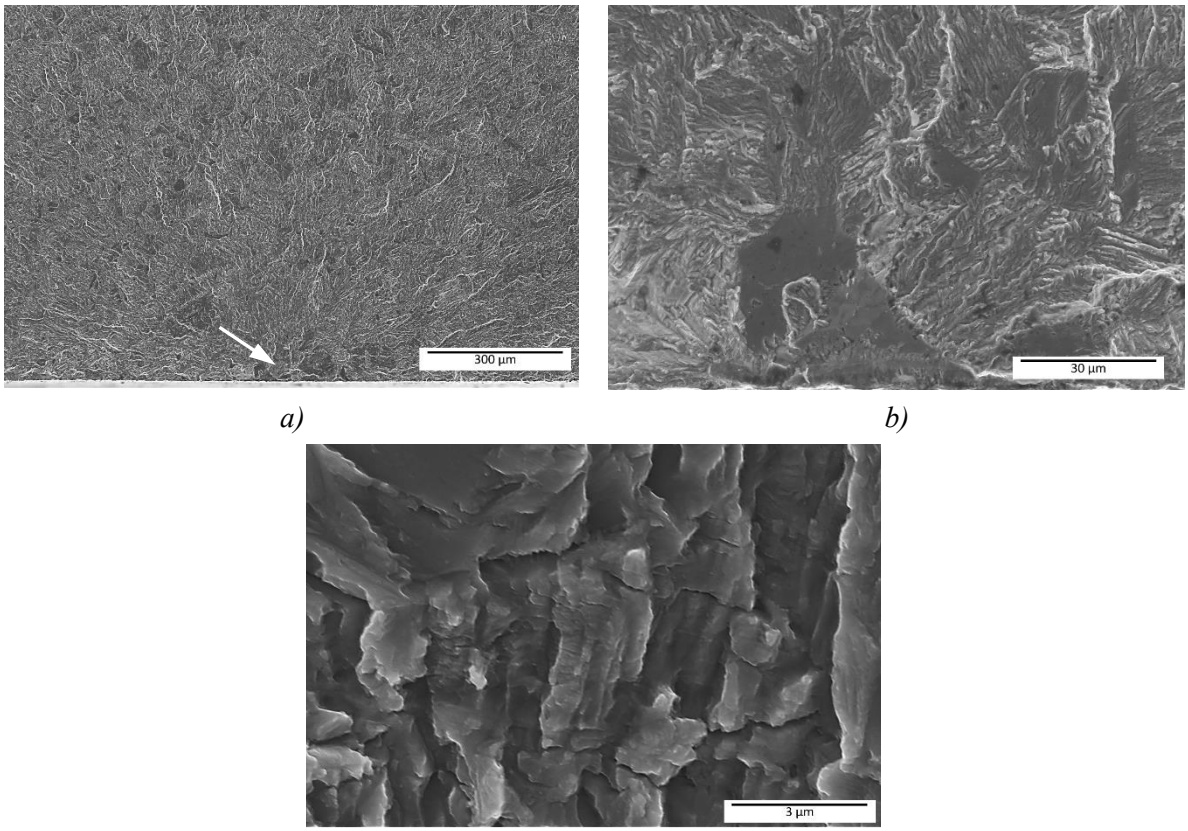

a) *b)*

c)

Figure 5-15. SEM images of fatigue fracture surface shown by 410 alloy tested with σ_a = 320 MPa (289263 cycles to failure): a) fatigue crack initiation (marked by white arrow) and propagation areas; b) fatigue crack initiation area shown at higher magnification; c) fatigue crack striations seen on the fatigue crack propagation area.

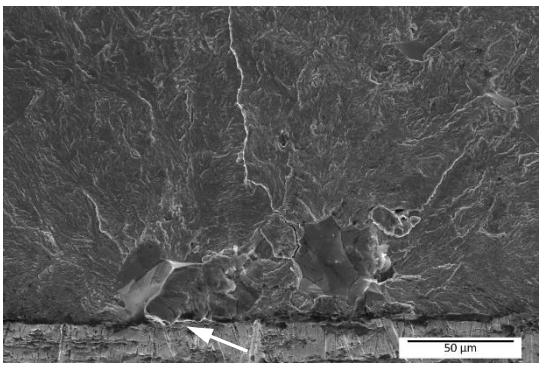

Figure 5-16. SEM image of fatigue fracture surface shown by 420ma alloy tested with σ_a = 300 MPa (62619 cycles to failure): fatigue crack initiation (marked by white arrow) by intergranular cracking (the only case observed in this work).

Fatigue crack propagation occurs also predominantly in transgranular mode. Fatigue crack striations are observed over the fatigue crack propagation area of all samples. Their typical appearance is illustrated on Figure 5-15c and Figure 5-17a. Such striations represent local crack-growth increments and have been hypothesized to occur via a mechanism of opening and blunting of the crack tip on loading, followed by resharpening of the tip on unloading [115]. Figure 5-17b shows a spot of local crack propagation along prior austenite grain boundaries observed on the surface of the 420 alloy tested with σ_a = 325 MPa (644000 cycles to failure). It should be noted that the size of such spots does not exceed 100 µm and their surface fraction

is negligibly low. MnS inclusions debonded from the martensitic matrix can be clearly seen over the crack propagation areas of all tested samples (Figure 5-17a). It should be noted that one sample (420ma alloy tested with σ_a = 460 MPa) showed a MnS inclusion on the fatigue crack initiation area (Figure 5-18b). This is also confirmed by the outcomes of the EDS analysis (Figure 5-18c), which rule out a possibility of fatigue crack formation at a corrosion pit, as no oxygen is detected.

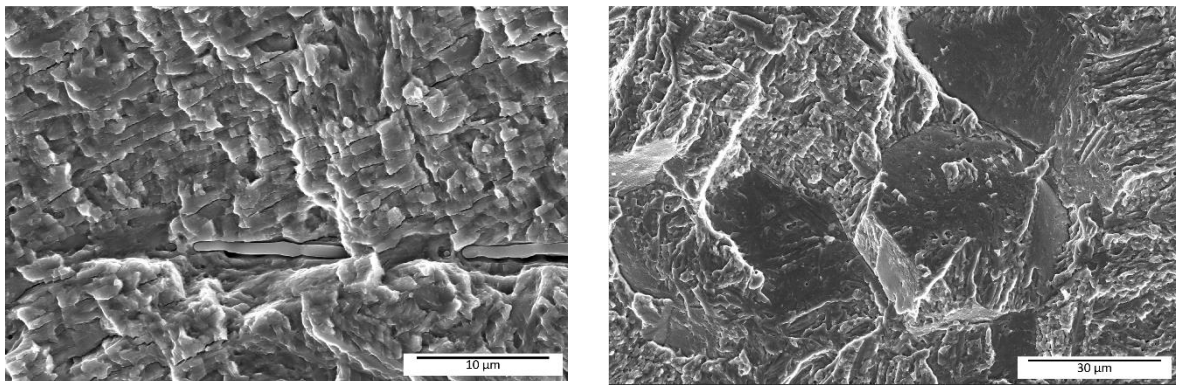

a) *b)*

Figure 5-17. SEM images of fatigue fracture surface shown by 420 alloy tested with σ_a = 325 MPa (644000 cycles to failure): a) MnS inclusion debonded from the martensitic matrix in the fatigue crack propagation area, fatigue crack striations are seen; b) local crack propagation in the intergranular mode.

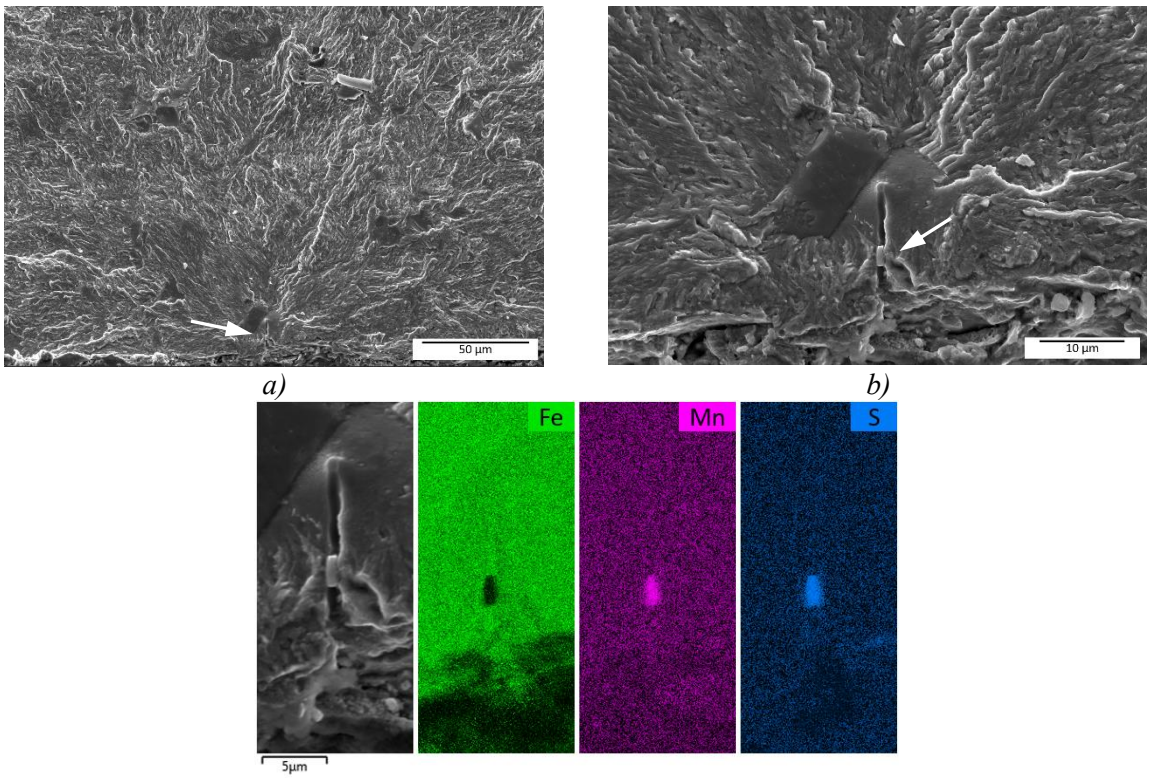

a) *b)*

c)

Figure 5-18. SEM images of fatigue fracture surface shown by 420ma alloy tested with σ_a = 460 MPa (25804 cycles to failure): a) fatigue crack initiation (marked by white arrow) and propagation areas; b) fatigue crack initiation area shown at higher magnification (fragment of a broken MnS inclusion is seen); c) the outcomes of the EDX analysis performed on the area of fatigue crack initiation confirming the presence of MnS inclusion.

5.3.3. Interaction of fatigue crack with microstructural constituents

In the high-cycle fatigue regime, the fatigue life of metallic materials is determined by fatigue crack initiation [111]. The fatigue fracture surface analyses clearly show that intergranular fatigue crack initiation and propagation is dominating in the Q&P-treated martensitic stainless steels (Figure 5-15 – Figure 5-18). As is well known, lath martensite has a complex hierarchical structure characterized by a large amount of internal subgrain/substructure (e.g., packets and blocks), as demonstrated in Figure 5-5. To gain a deeper insight into fatigue crack initiation and propagation mechanisms in the Q&P-treated martensitic stainless steels, EBSD mapping of both halves of the fractured sample in the corresponding regions of the fatigue crack initiation and propagation are performed.

The outcomes of the EBSD characterization shows that fatigue crack initiation and propagation occur along martensite packet or block boundaries. This is clearly demonstrated in Figure 5-19 for the fatigue crack initiation area and Figure 5-20 for the fatigue crack propagation area. From the EBSD maps, it is seen that the crack grows partially along martensite packet boundaries (packets are painted in different colors in Figure 5-19a and Figure 5-20a). In the areas where the fatigue crack crosses the packet, it propagates along the block boundaries (martensite variants V are painted in different colors on Figure 5-19b and Figure 5-20b). In the latter case, the propagation of the fatigue crack was detected between V7 and V13, V7 and V15, V21 and V7, V1 and V21, V4 and V24, V7 and V24, V13 and V11, V9 and V20 for the initiation area; and between V18 and V18, V16 and V15, V23 and V19, V23 and V22, V18 and V17 for the propagation area. Each martensite variant in each pair belongs to different martensite blocks within the same martensite packet. These observations can be rationalized based on the incompatibility between plastic strains at the packet and block boundaries due to significant differences in the maximum Schmid factors [16], [116].

The prior austenite grain boundaries play a minor role in the fatigue crack initiation and propagation. Only one sample out of the 36 demonstrated intergranular cracking on the fatigue crack initiation area (Figure 5-16). This could be related to the potential local grain boundary embrittlement as a result of local nanosegregations of embrittling elements, such as phosphorus or hydrogen [117]. The surface fraction of crack growth along prior austenite grain boundaries is negligible in all analyzed samples. For the crack initiation EBSD map, no instances of this phenomenon are found (Figure 5-19). The only secondary crack growing along prior austenite grain boundaries was detected on the crack propagation EBSD map (marked by a white arrow on Figure 5-20c), and its depth was less than 10 μm.

There is a noticeable transformation of retained austenite grains into martensite in the subsurface at the fatigue crack initiation spot (Figure 5-19d), and the local volume fraction of retained austenite decreases from 18.7 % to 8.2 % (Table 5-14). Crack subsurface regions in the fatigue crack propagation area have a significantly reduced volume fraction of retained austenite, 3.1 % (Table 5-14, Figure 5-20d). The depth of the analyzed subsurface regions with significantly reduced volume fraction of retained austenite is ~ 10 μm. A comparison of the local KAM distribution histograms (Figure 5-21) clearly shows that the local KAM values of the subsurface regions (e.g., areas under the crack path) are noticeably higher than those away from the crack. This indicates high density of GNDs [107] accumulated locally under the subsurface due to the plastic zone at the tip of the propagating crack.

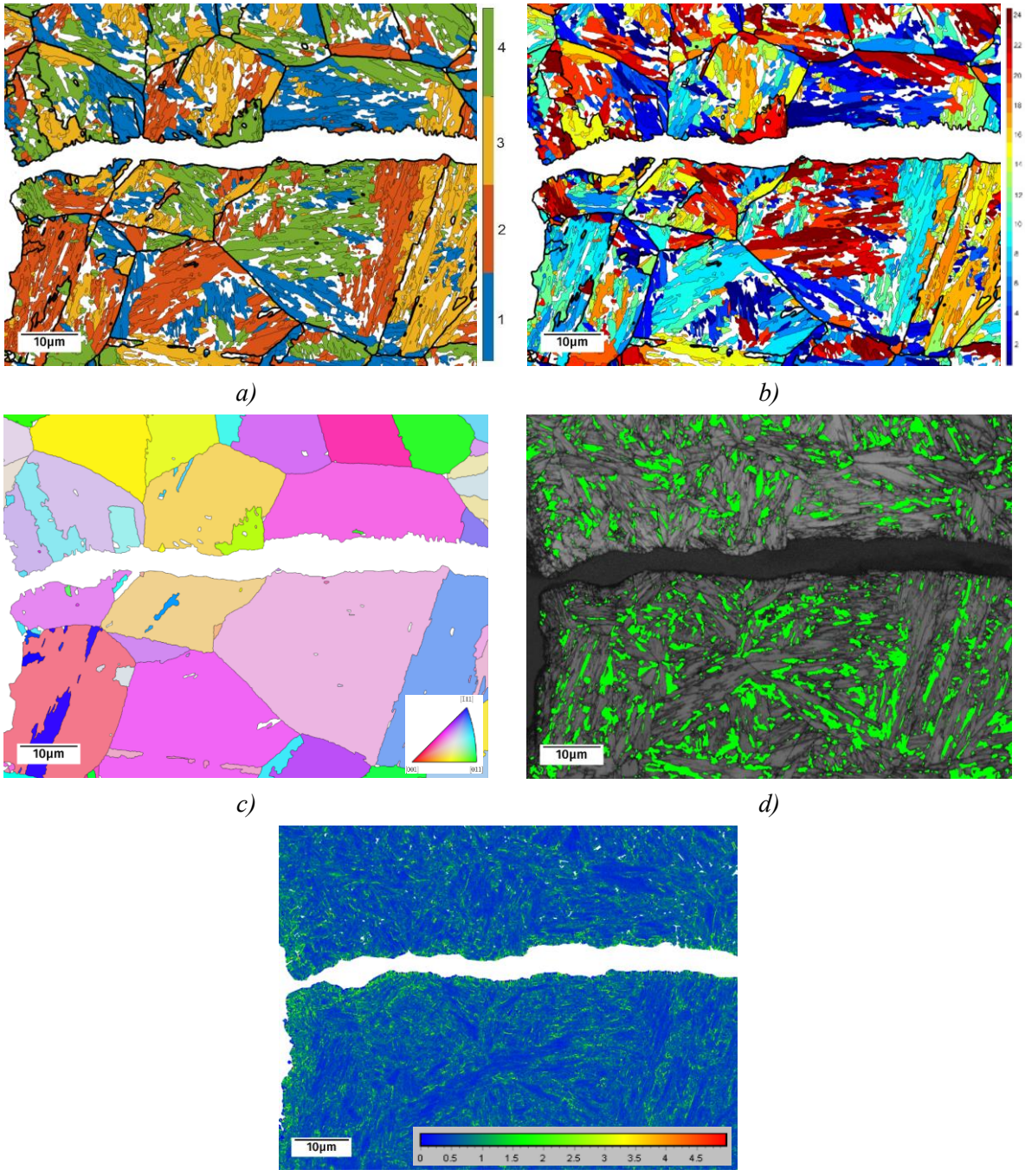

Figure 5-19. Results of EBSD analysis of the fatigue crack initiation area (left edge): a) map of martensite packets, b) map of martensite variants, c) map of prior austenite grains, d) band contrast map with retained austenite colored in green, e) KAM map. Black lines represent PAG boundaries along with the twin boundaries.

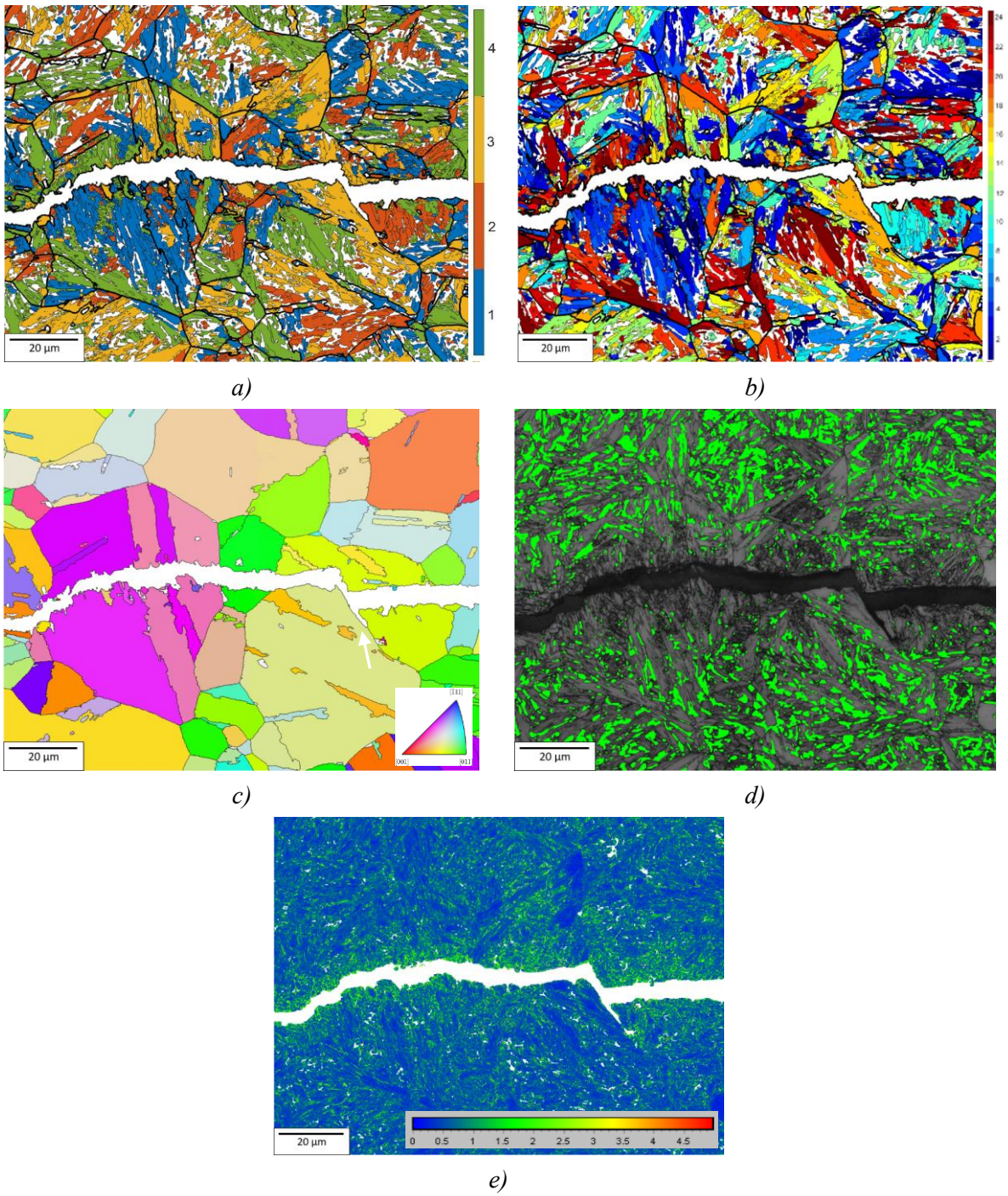

a) *b)*

c) *d)*

e)

Figure 5-20. Results of EBSD analysis of the fatigue crack propagation area (at ~350 µm from the fatigue crack initiation spot): a) map of martensite packets, b) map of martensite variants, c) map of prior austenite grains, d) band contrast map with retained austenite colored in green, e) KAM map. Black lines represent PAG boundaries along with the twin boundaries and the white arrow indicates the secondary crack along a prior austenite grain boundary.

Table 5-14. Local volume fractions of interlath and blocky retained austenite measured on the EBSD maps taken from the areas of the fatigue crack initiation and propagation.

		Total	Interlath retained austenite (IL-RA)				Blocky retained austenite (B-RA)			
		V_{RA} [%]	V_{il}^{RA} [%]	Average grain size [µm]	Min-max values [µm]	N grains	V_{blocky}^{RA} [%]	Average grain size [µm]	Min-max values [µm]	N grains
Before Fatigue	Bulk	18.7	2.5	0.56 ± 0.17	0.36-0.99	972	16.2	2.11 ± 1.44	1.00-10.39	336
After Fatigue	Init. Sub-surf.	8.2	2.8	0.41 ± 0.18	0.21-0.98	395	5.4	1.76 ± 0.70	1.02-3.69	44
	Prop. Sub-surf.	3.1	0.9	0.53 ± 0.17	0.34-0.99	308	2.2	1.7 ± 0.88	1.00-6.49	68

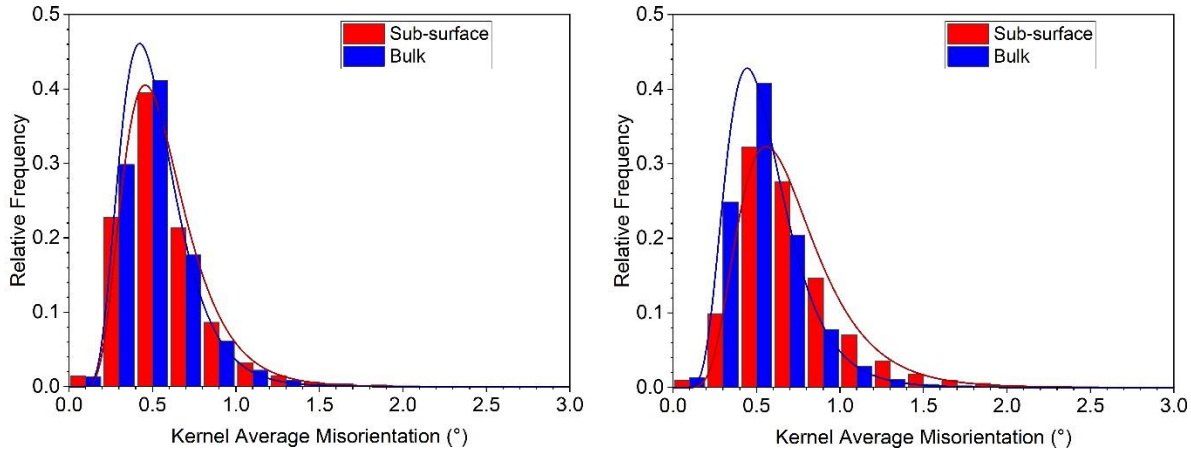

a) *b)*

Figure 5-21. Histograms of the local misorientation distribution of the Q&P-treated 420ma alloy after fatigue testing with stress amplitude σ_a = 460 MPa: a) area of the fatigue crack initiation; b) area of the fatigue crack propagation at the distance of ~ 350 µm from the fatigue crack initiation area. Local misorientations of the tested sample were measured on the subsurface area (≤ 2 µm) from the fatigue fracture surface and the remaining area of the tested sample (bulk).

The size of the plastic zone is determined by a range of parameters including applied global stress and crack length. The radius of the plastic zone at the tip of the propagating fatigue crack can be calculated using the stress intensity factor K_I. Newman and Raju [118] proposed a solution for K_I in the case of a surface crack in a sample subjected to remote tension or bending loads. The stress-intensity factors used to develop these equations were obtained from three-dimensional finite-element analyses of these crack configurations. The equations give stress intensity factors as a function of parametric angle, crack depth, crack length, plate thickness, and, where applicable, crack radius. The Newman and Raju solution for a plate with a crack surface subjected to remote tension load is expressed in the following form [118]:

$$K_I = \sigma \sqrt{\frac{\pi a}{Q}} F\left(\frac{a}{t}, \frac{a}{c}, \frac{c}{W}, \phi\right) \quad \textit{(Eq. 5.8)}$$

where σ is the remote tensile stress, a the depth of the crack, c the half-length of crack, t the width of the sample, and W the thickness of the sample. The parameter Q in (Eq. 5.8) is calculated as

$$Q = 1 + 1.464 \left(\frac{a}{c}\right)^{1.65} \quad \textit{(Eq. 5.9)}$$

The parameter F is calculated as

$$F = \left[M_1 + M_2 \left(\frac{a}{t}\right)^2 + M_3 \left(\frac{a}{t}\right)^4\right] f_\phi f_\omega g \quad \textit{(Eq. 5.10)}$$

where

$$M_1 = 1.13 - 0.09 \left(\frac{a}{c}\right) \quad \textit{(Eq. 5.11)}$$

$$M_2 = -0.54 + \frac{0.89}{0.2 + \left(\frac{a}{c}\right)} \quad \textit{(Eq. 5.12)}$$

$$M_3 = 0.5 - \frac{1.0}{0.65 + \left(\frac{a}{c}\right)} + 14 \left(1.0 - \frac{a}{c}\right)^{24} \quad \textit{(Eq. 5.13)}$$

$$f_\phi = \left[\left(\frac{a}{c}\right)^2 \cos^2 \phi + \sin^2 \phi\right]^{\frac{1}{4}} \quad \textit{(Eq. 5.14)}$$

$$f_\omega = \left[\sec\left(\frac{\pi c}{2W} \sqrt{\frac{a}{t}}\right)\right]^{-\frac{1}{2}} \quad \textit{(Eq. 5.15)}$$

$$g = 1 + \left[0.1 + 0.35 \left(\frac{a}{t}\right)^2\right] (1 - \sin \phi)^2 \quad \textit{(Eq. 5.16)}$$

In (Eq. 5.14) and (Eq. 5.16), ϕ is the parametric angle (deg). The parameters used in the calculation are listed in Table 5-15. It should be noted that the maximum stress during fatigue testing was used as the remote tensile stress σ.

Table 5-15 Parameters used to calculate the radius of plastic zone at the tip of the fatigue crack.

a	$3.43 \cdot 10^{-4}$ m
c	$3.43 \cdot 10^{-4}$ m
W	$7.5 \cdot 10^{-4}$ m
t	$1 \cdot 10^{-2}$ m
σ	1022 MPa
ϕ	90°
$\sigma_{0.2}$	1082 MPa

To calculate the radius of the plastic zone r_p at the crack tip, (Eq. 5.17) proposed for plane strain is used:

$$r_p = \frac{1}{4\pi}\left(\frac{K_I}{\sigma_{0.2}}\right)^2 \left[(1-2\nu)^2(1+\cos\theta) + \frac{3}{2}\sin^2\theta\right] \qquad \textit{(Eq. 5.17)}$$

where σ_{YS} is the yield strength, ν is the Poisson's ratio, and θ is the angle in polar coordinates ($\theta = 0$ °). The estimated radius of plastic zone for the given case was 67.8 µm, which is in a good accordance with the depth of the subsurface area with the increased KAM values on the EBSD map (Figure 5-20e). Microplastic deformation within this plastic zone promotes transformation of metastable retained austenite grains into martensite. This turns out in the significantly reduced local volume fraction of retained austenite in the subsurface volume compared to the areas away from the crack (Table 5-14). Similar observations were reported earlier for a TRIP 700 steel subjected to high cycle fatigue [119] and 18CrNiMo7-6 high strength steel after fatigue crack propagation testing [120].

The outcomes of this analysis are in a good agreement with the results recently presented by Okada et al. in [16]. It was shown that the vast majority of surface crack initiation and propagation in an 8Ni-0.1C martensitic steel occurred along martensite block boundaries, whereas the fraction of the fatigue cracks initiated along prior austenite grain boundaries did not exceed 4 %. Similar observations were also reported by Ueki et al. [116] for an ultralow carbon (0.0026 wt. %C) martensitic steel subjected to fatigue crack growth testing, though the authors did not observe any crack propagation along prior austenite grain boundaries in the latter work.

Fatigue fracture surface analysis performed in this study clearly shows that the MnS inclusions do not promote any fatigue crack initiation, as only one sample out of 36 presented a MnS inclusion on the fatigue crack initiation spot (Figure 5-18). The analysis performed by Murakami in his book [121] showed that MnS inclusions lower fatigue strength of steels if the value of their $\sqrt{area}$ is sufficiently large. The experimental study performed by Findley and colleagues on quenched and tempered martensitic steels in [122] has shown that the allowable stress to avoid the fatigue crack initiation at the MnS inclusions dramatically increases with decreasing $\sqrt{area}$. They observed fatigue crack formation at MnS inclusions (i.e. their detrimental effect on fatigue performance) for MnS inclusions having $\sqrt{area}$ = 10-30 µm (Figure 5-22). The MnS inclusions present in our studied materials have, in average, a diameter of 0.9 µm and a length of 8.2 µm (Figure 5-17a, Figure 5-18). So, their cross-section area is

7.38 μm^2, resulting in $\sqrt{area}$ = 2.72 μm. According to calculations in [122], the maximum allowable stress to avoid fatigue crack formation in our studied steels would be well above 2 GPa, and the MnS $\sqrt{area}$ in our materials is much smaller compared to the critical inclusion sizes leading to fatigue crack initiation ($\sqrt{area} = 10 - 30$ μm in [122]). Therefore, it can be concluded that the MnS inclusions in the steels studied in this work do not affect the high cycle fatigue behavior due to small size. Likewise, neither Fe_3C nor complex (Ti, Nb)C nanocarbides appear to exert a significant influence, likely due to their small size.

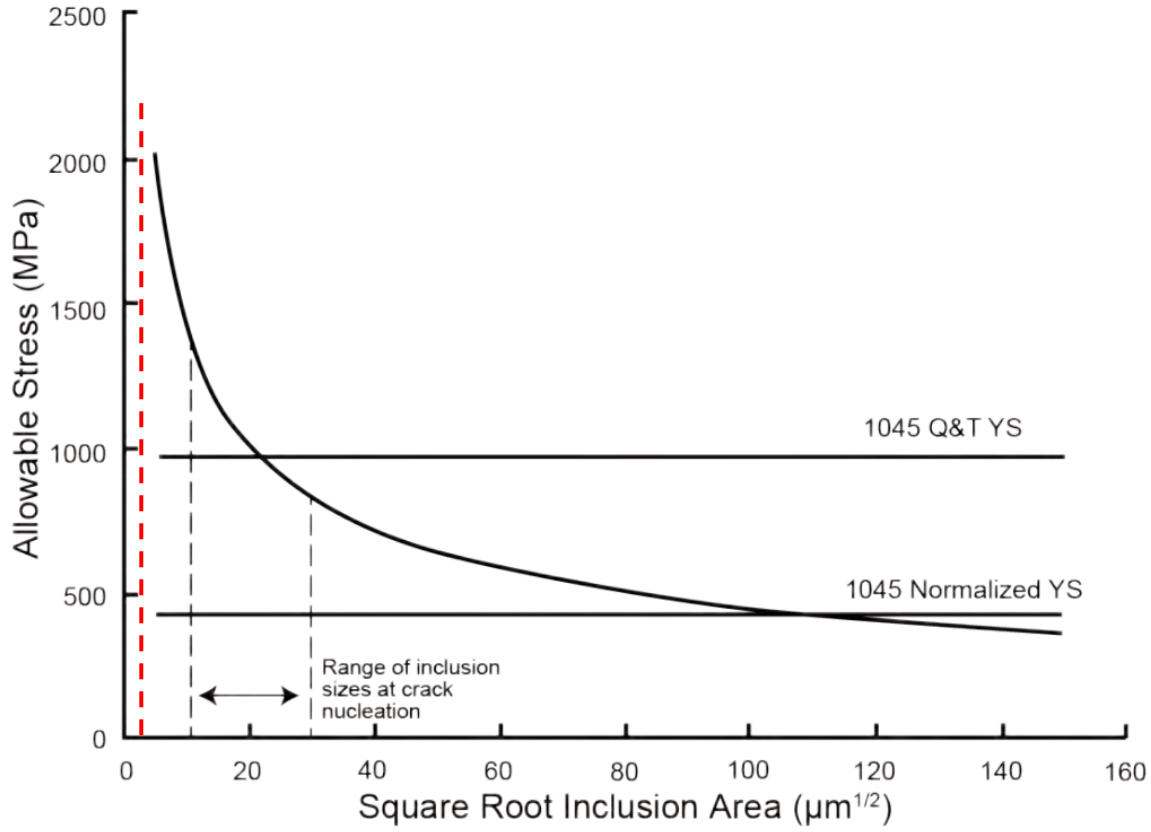

Figure 5-22. Plot showing the critical inclusion sizes for 1045 normalized and quenched and tempered bar steels along with experimentally observed inclusion sizes at the crack nucleation site in the core microstructure of induction-hardened 1045 quenched and tempered steel, from [122]. *The red dashed line marks the* $\sqrt{area}$ *= 2.72 μm inclusion size of the present work.*

Debonding of MnS inclusions from the martensitic matrix during fatigue crack growth (Figure 5-17a) can be related to the plastic zone at the tip of the propagating crack resulting in local failure when the local inclusion/matrix interfacial stress reaches the critical value [123]. Also, the MnS inclusions neither deviate the fatigue crack from its growth direction nor promote its bifurcation (Figure 5-17a). Therefore, it can be concluded that their influence on the fatigue performance is negligible, which is in a good agreement with earlier reports [124].

As is well known, the low cycle fatigue life of metallic materials is controlled by the material's resistance to fatigue crack propagation [111], [125]. This study clearly shows the transformation of retained austenite in the plastic zone during fatigue crack growth (Figure 5-20d). Previous studies have shown that the enhanced volume fraction of retained austenite in Q&P-treated carbon steels can noticeably improve their fatigue crack growth resistance and ΔK_{th} value when tested with relatively low ΔK values [126]. Similarly, the retained austenite

improved the low cycle fatigue life of a ferritic-martensitic steel when tested with low strain fatigue due to the energy absorption by transformed austenite during crack propagation [127]. Therefore, it can be hypothesized that Q&P processed martensitic stainless steels may demonstrate better low cycle fatigue performance compared to their conventional counterparts. The low cycle fatigue behavior and fatigue crack growth behavior in the Q&P-treated martensitic stainless steels are very interesting topics for further research.

5.3.4. Conclusions to Section 5.3.

The high-cycle fatigue performance of the Q&P-treated sheets of martensitic stainless steels was explored. The role of their complex hierarchic microstructure in high-cycle fatigue behavior was studied. The following conclusions can be drawn based on the outcomes of this work.

- Alloy 420 showed the highest fatigue limit σ_f -value (320 MPa), followed by alloy 410 (300 MPa) and alloy 420ma (270 MPa). However, the highest σ_f/σ_{UTS} -ratio is demonstrated by alloy 410 (0.24) followed by alloy 420 (0.22) and alloy 420ma (0.19). Therefore, it can be concluded that alloy 410 shows the best fatigue performance compared to other studied Q&P treated alloys. Overall, the Q&P-treated martensitic stainless steels show a satisfactory fatigue performance when compared to their conventional counterparts.
- Fatigue crack initiation occurs at the surface in a transgranular mode along martensite packet or block boundaries. There is no effect of MnS inclusions, Fe_3C or complex (Ti,Nb)C nanocarbides on the fatigue crack initiation process due to their small size. The fatigue crack grows predominantly in a transgranular mode along martensite packet or block boundaries, leaving fatigue crack striations on the surface of the tested samples. The fatigue crack growth is also accompanied by debonding of the elongated MnS inclusions from the martensitic matrix.
- Microplastic deformation within the plastic zone at the tip of the propagating fatigue crack leads to enhanced local KAM values and local transformation of retained austenite grains. It is hypothesized that the local TRIP effect may lead to improved low cycle fatigue performance of the Q&P-treated martensitic stainless steels when compared to their conventional counterparts.

5.4. Formability of the Q&P-treated large sheets

5.4.1. Results of Nakajima testing

Figure 5-23 illustrates typical appearance of Nakajima samples after testing. These tests are stopped once a crack formed on top of the dome of sample The major and minor stresses measured using DIC on the grid pattern are listed in Table 5-16. Forming limit diagrams (FLD) are constructed for each alloy using the major and minor stresses (Figure 5-24), and for reference, the curves for commercial DP600 and TRIP700 grades have been included [128], [129]. As can be seen in the graph, martensitic stainless steels show some formability thanks to the Q&P heat treatment. However, the formability of Q&P-treated martensitic stainless steels is still limited. The formability of alloy 420ma may have been reduced because of the higher

volume fractions of brittle fresh martensite (Table 5-7) and blocky retained austenite characterized by lower stability (Table 5-10) [78].

Figure 5-23. Typical appearance of tested Nakajima samples.

Table 5-16. Major and minor stresses for each of the tested samples.

Alloy	410		420		420ma	
	Minor Strain	Major Strain	Minor Strain	Major Strain	Minor Strain	Major Strain
Sample 1	-0.0961	0.2661	0.2467	-0.0804	-0.1	0.2
Sample 2	-0.0135	0.1631	0.1855	-0.0149	-0.0124	0.1645
Sample 3	-0.005	0.1598	0.1806	-0.0068	0.0133	0.1728
Sample 4	0.0192	0.1891	0.1855	0.0435	0.0339	0.1828
Sample 5	0.1735	0.2553	0.2092	0.1075	0.1509	0.1948

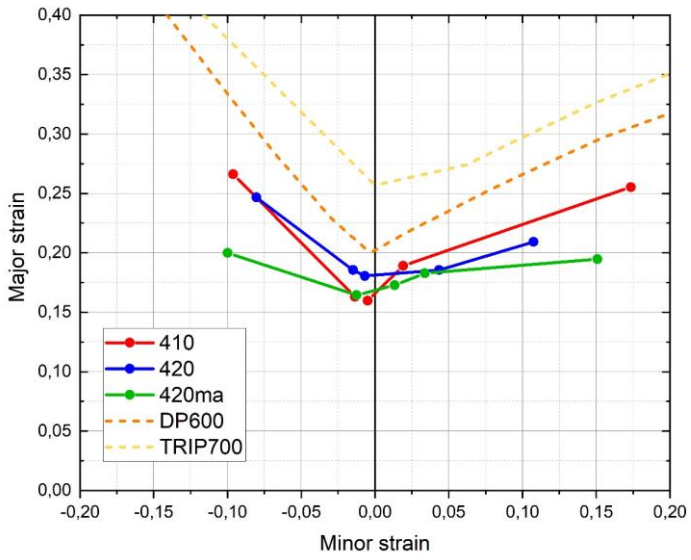

Figure 5-24. Forming limit diagrams.

The microstructure of tested samples (geometries 1, 3, and 5) are analyzed for 410 and 420ma alloys, as well as the undeformed microstructure. The studied samples belong to areas at the top of the deformed dome, where the accumulated local plastic strain was the highest. The corresponding phase maps and KAM maps are represented for said geometries (Figure 5-25 and Figure 5-26, respectively). The quantitative data extracted from these EBSD maps are collected in Table 5-17. The local plastic strain is also shown in Table 5-17. It was calculated as $\varepsilon_{pl} = \ln\left(\frac{t_0}{t_f}\right)$, being t_0 and t_f initial and final thickness, respectively, and measured at the area where the microstructure was obtained from. The stress triaxiality values are calculated, being 0.341, 0.655, and 0.666 for geometries 1, 3 and 5, respectively. Geometries with increasing stress triaxiality values resulted in higher local plastic strain.

The microstructure of the undeformed samples is the same as the ones reported in Section 5.1.3, since they have been machined from the large Q&P-treated sheets. The volume fraction of retained austenite in both alloys decreases significantly from the undeformed samples to the tested ones. In the case of alloy 410, a drop from 9.7 % to 0.75-0.2 % is observed, while for alloy 420ma, the phase content decreases from 18.7 % to 8.9-6.4 % (Table 5-17). This reduction is directly related to the value of local plastic strain accumulated in each sample. The metastable retained austenite transforms into fresh martensite during plastic deformation, and the progress of this transformation is controlled by many factors, where stability plays a major role [33], [130]. However, sample 410 – geometry 3 does not follow this general trend, as seen by the slightly superior content of retained austenite than the other two geometries. This observation can be rationalized based on the local character of the EBSD technique.

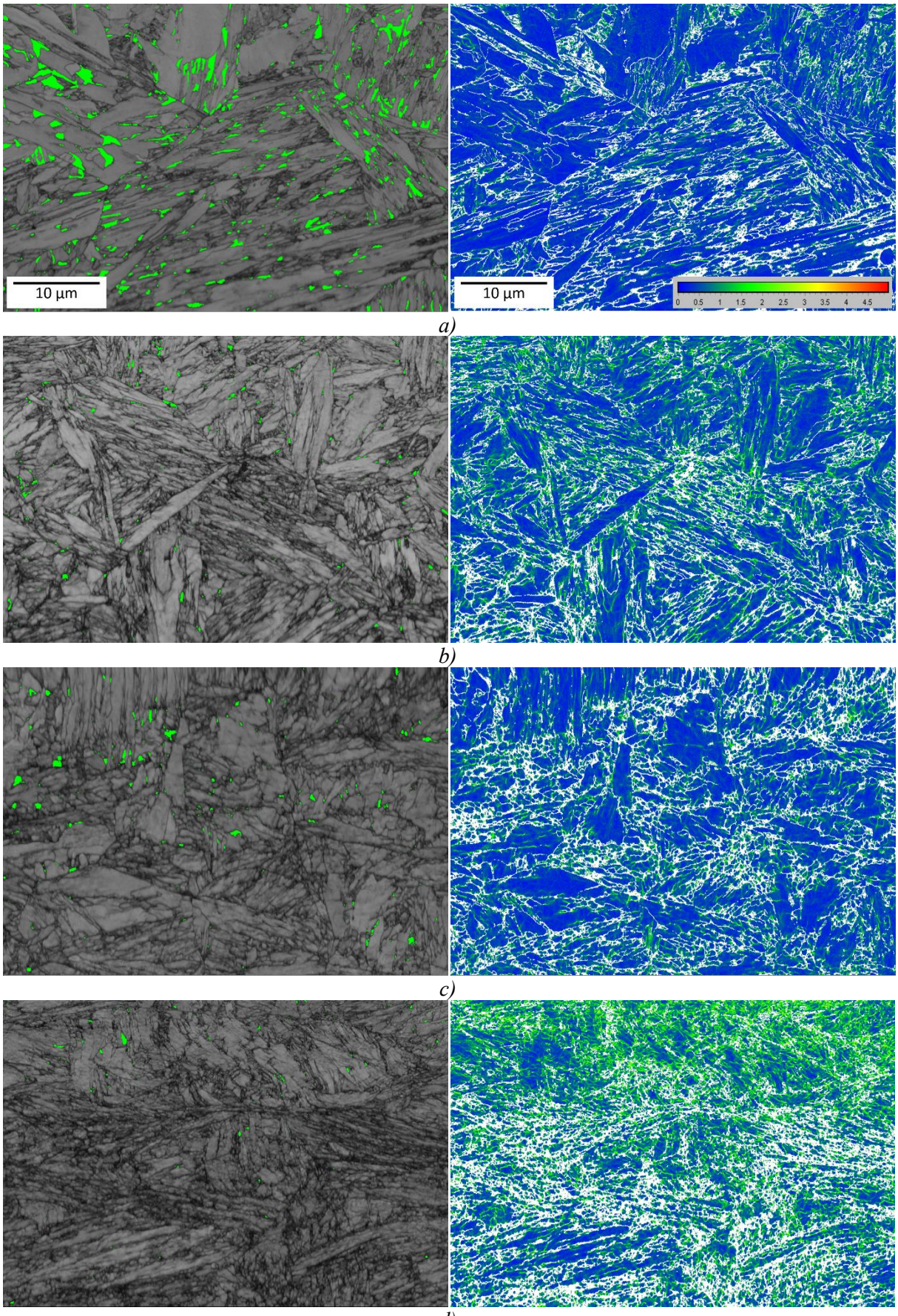

Figure 5-25. EBSD maps of Nakajima samples from alloy 410: a) undeformed sample, b) geometry 1, c) geometry 3, d) geometry 5.

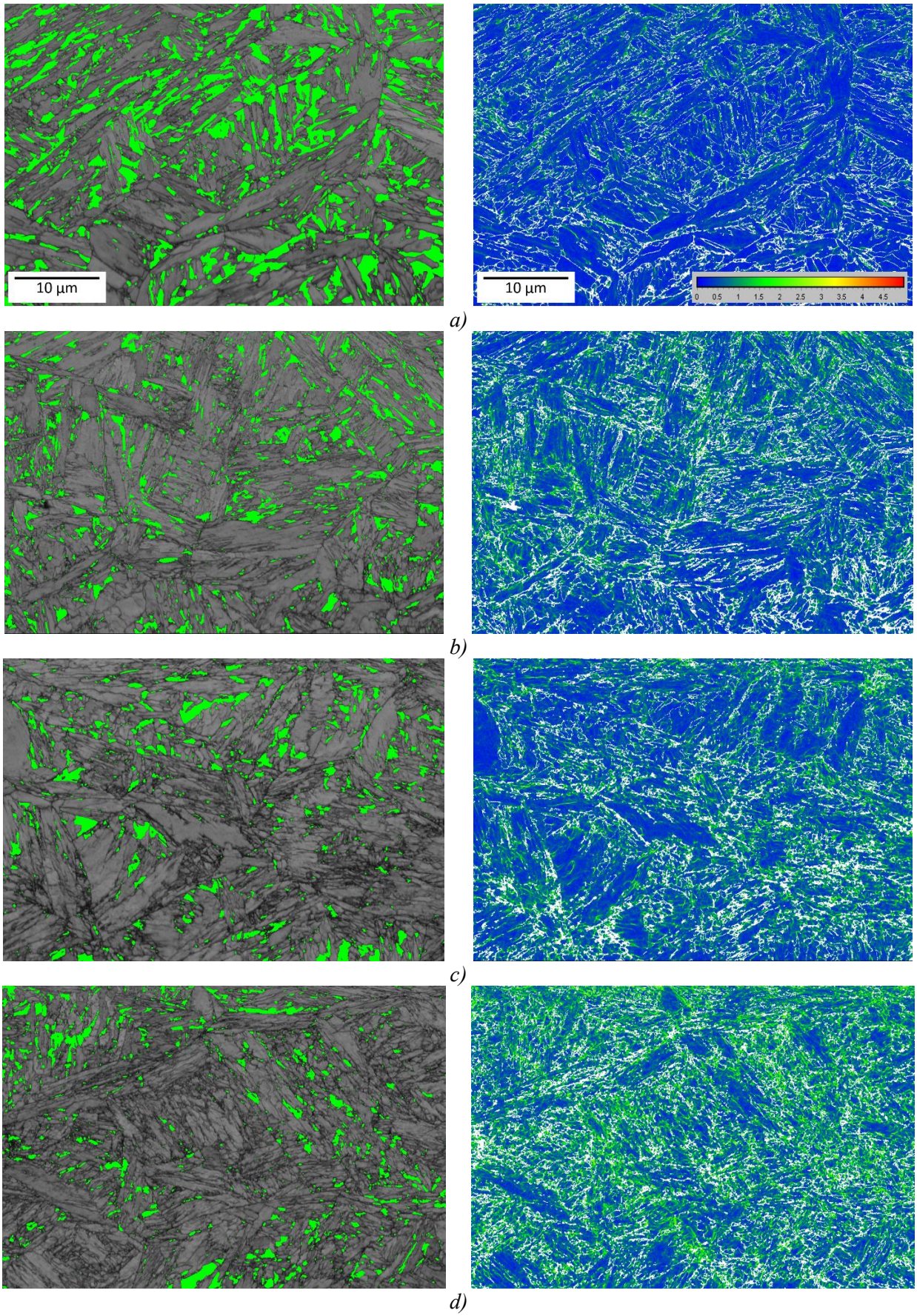

Figure 5-26. EBSD maps of Nakajima samples from alloy 420ma: a) undeformed sample, b) geometry 1, c) geometry 3, d) geometry 5.

Table 5-17. Microstructural data from EBSD characterization of samples after Nakajima testing.

Alloy	Geometry	Retained Austenite			Fresh Martensite	Non-Indexing rate [%]	Local plastic strain [%]
		V_{RA} [%]	d_{RA} [µm]	RA aspect ratio [-]	V_{FM} [%]		
410	1	0.6	0.3 ± 0.1	2.4 ± 1.2	7.4	18.9	15.9
	3	0.75	0.3 ± 0.2	2.6 ± 1.4	8.9	20.1	23.5
	5	0.2	0.3 ± 0.1	2.5 ± 1.3	10.9	32.5	45.4
420ma	1	8.9	0.4 ± 0.3	2.7 ± 1.4	11.5	19.7	13.5
	3	6.8	0.4 ± 0.4	2.4 ± 1.1	12.3	17.2	23.8
	5	6.4	0.4 ± 0.3	2.3 ± 1.1	17.8	21.3	26.5

Lastly, the histograms of the local misorientation of the martensite phase are plotted for all studied formability samples of both alloys (Figure 5-27). As it can be observed in both graphs, there is an increase of the peak value of the distribution from the undeformed state to the higher stress triaxiality samples. In both cases, this value increases from 0.33° to 0.57°. Moreover, also the distribution changes with the increasing stress triaxiality, becoming more uniform (broader and shorter peaks).

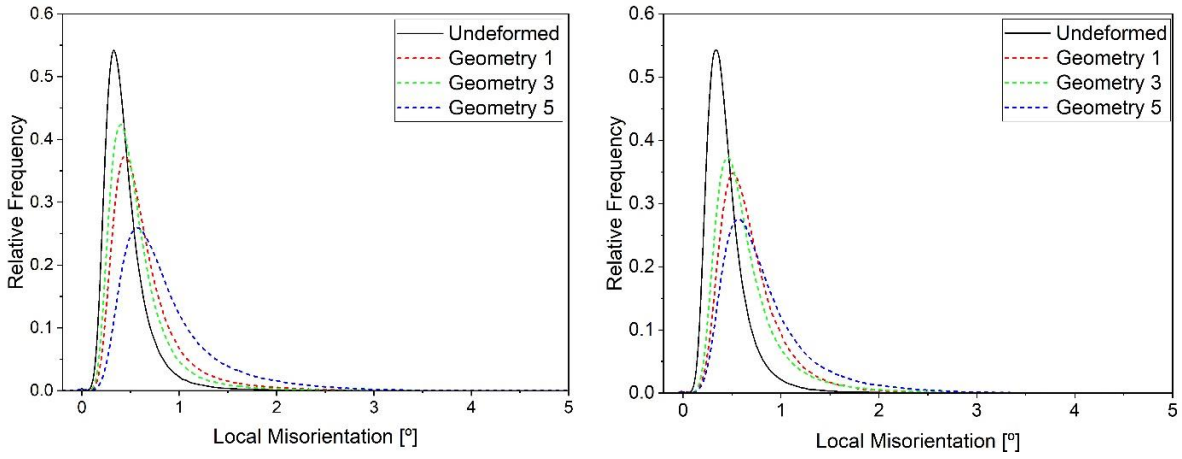

a) *b)*

Figure 5-27. Distribution of local misorientation in the martensitic matrix for a) alloy 410 and b) alloy 420ma.

5.4.2. Validation of the developed model

In this section, the results derived from the simulations developed aiming at replicating the Nakajima experiments computationally are shown and discussed, specifically with a focus on the different theoretical procedures applied and the outcome arising from them.

5.4.2.1. Approach to plasticity simulation: Johnson-Cook vs. traditional stress-strain curves

Two different approaches are initially considered when dealing with the method to simulate the plastic behavior of the material for the different Nakajima experiments that needed to be replicated numerically. Namely, these are the use of stress-strain curves extracted from the initial tensile tests and the utilization of the J-C model, which implies the additional finding of the corresponding material parameters to describe the characteristics of the martensitic stainless steel properly.

More in detail, when the first of them is employed, the tensile stress-strain data points taken from the quasistatic tensile tests are introduced as the plastic model within the ABAQUS models. After running the Nakajima test models, the simulated force vs. displacement curves can be obtained and compared with those recorded during the actual tests. This way, it is observed that depending on the sample shape, and therefore, on the different stress states occurring during the tests, the fitting accuracy of the numerical data with respect to the actual data can notably vary, getting relative error percentages between the different curves in the range of 5 - 150 %. When trying to apply scaling factors to the stress-strain data to try to reduce the higher errors, the smaller ones are increased, not being able to improve the overall results.

Thus, a different approach has to be taken into account if the Nakajima tests are to be replicated with high fidelity. In particular, ABAQUS offers a variety of constitutive material models, including the J-C equation. Therefore, this relation has been chosen to appropriately simulate metals subjected to plastic deformation. It is worth noting that other models such as the Zerilli-Armstrong model or Arrhenius-type equations could also be considered for similar purposes. As a result of its use, each element stress state of the simulated Nakajima samples can be calculated in each simulation time step with a significantly higher precision than in the more rudimentary case of employing a tabulated relation of points uniquely taken from uniaxial tensile tests, which do not represent either the actual complex state and varying triaxiality occurring during the tests. This leads to the achievement of a better match between the experimental and simulated force-displacement curves obtained.

To enable usage, the determination of various material parameters is essential. This involves a procedure as the one presented in [76]. Unfortunately, as only quasi-static tests at room temperature are available, only the A, B and n parameters can be calculated. The remaining C and m parameters must be fixed, and for this, standard values from the literature are adopted, considering them to be the same for the three different materials, based on their similar chemical compositions [131]. In any case, neither high strain rates nor high temperatures are expected to take place during the industrial processes aimed at being simulated, therefore no major importance is considered to lie upon these values.

Table 5-18. Parameters in J-C model used for simulations.

Alloy	A	B	n	C	m	$\dot{\varepsilon_{p_0}}$	θ_{room}	θ_{melt}
410	985 MPa	523.2 MPa	0.282	0.02	0.8	0.001 s^{-1}	20 °C	1495 °C
420	1020 MPa	715.2 MPa	0.599	0.02	0.8	0.001 s^{-1}	20 °C	1495 °C
420ma	1030 MPa	424.6 MPa	0.287	0.02	0.8	0.001 s^{-1}	20 °C	1495 °C

Once fixed, all three alloys are simulated under the Nakajima test procedure, performing first the comparison between the force vs. displacement data extracted from them, employing both the J-C and the FLD curves as strength and fracture constitutive methods, and the actual data from the experiments.

In Figure 5-28, the latter comparison is shown for the extreme cases of stress state, taking place when samples 1 and 5 are simulated (see Figure 4-1), having then uniaxial tension and equibiaxial tension conditions, respectively. It can be observed how the errors in both displacement to fracture and force exerted during the tests are relatively limited and even in all cases. In particular, the global average errors found are 11.7 % and 14.9 %, respectively. It must be remarked that since the displacement to fracture has been assessed as very lowly dependent on the work absorbed by the samples during the simulations, only the maximum force, and not the whole loading curve, has been considered for the calculation of the latter error.

Analyzing these results, the error of 11.7 % obtained when simulating the displacement to fracture for all samples can tentatively be considered a success. The cracking phenomenon is highly complex, and errors within similar ranges are typically encountered when attempting to simulate such intricate physical processes. Regarding the error of 14.9% obtained when simulating the maximum force exerted during the tests, it has been assessed that the significance of this factor for simulating a material's ductility is not as high as the importance of the displacement to fracture. Therefore, the consequences of this result are not considered to have a major impact on the simulations. This will be proved with the aid of the simulations in the next section (Section 5.4.2.2), where in spite of the fact of having observed higher maximum forces in the Nakajima numerical models, as shown in Figure 5-28, the simulated FLD curves obtained are more conservative than those extracted from the real tests.

Bearing this analysis in mind, the previous results can be initially considered good enough to be able to assess the simulations as successful, provided that these are further on the basis of subsequent and more complex tests.

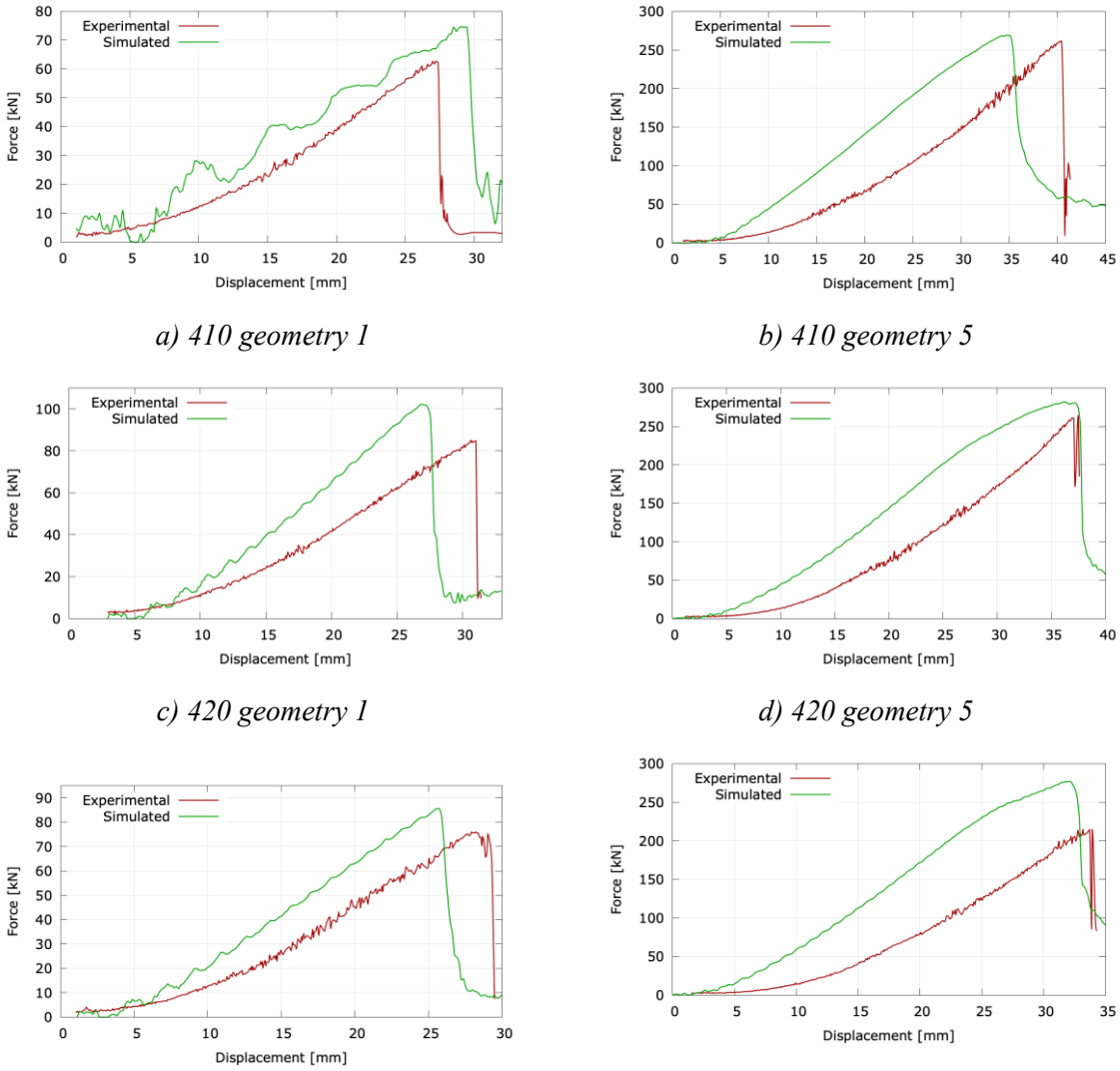

a) 410 geometry 1

b) 410 geometry 5

c) 420 geometry 1

d) 420 geometry 5

e) 420ma geometry 1

f) 420ma geometry 5

Figure 5-28. Nakajima force vs. displacement data comparison between simulated and experimental tests for alloy 410 (a, b), 420 (c, d) and 420ma (e, f).

5.4.2.2. Plastic strain distribution and FLD curves comparison in the Nakajima tested samples

After the previously demonstrated initial validation of the constitutive model for simulating the strength and fracture behavior of the different alloys (Section 5.4.2.1), a more comprehensive comparison is conducted. This comparison focuses on the key data extracted from the Nakajima experiments, with the aim of fully validating the computational models. Specifically, the two considered QoI are the plastic equivalent strain (ε_p) prior to the fracture point as well as the FLD curves, which are considered as the most critical criteria for predicting the material's ability to withstand damage during forming processes. Therefore, its validation in the computational case attains considerable importance to employ these models as future useful tools.

More specifically, for the validation of the simulated ε_p, the same procedure as the one used to extract the experimental data is employed in the simulations, taking the highest value registered in any of the sample's mesh elements after the fracture of the material has occurred.

Once checked all the comparative values for every test (e.g., Figure 5-29), it has been calculated that the global average error when considering the 15 cases for every alloy and sample shape is 32.7 %. It might be regarded as too large taking into consideration that the attainment of a high-fidelity model is one of the main goals of this work. However, it must be taken into account that the computational model tends to increase excessively the value of plastic strain in those elements close to the fractured ones, distorting in an artificial manner the extracted values of ε_p. This comparison raises concerns about the suitability of using this approach to validate the model due to the presence of this undesirable numerical side effect. On the other hand, a second path is explored when comparing now the experimental and simulated FLD curves.

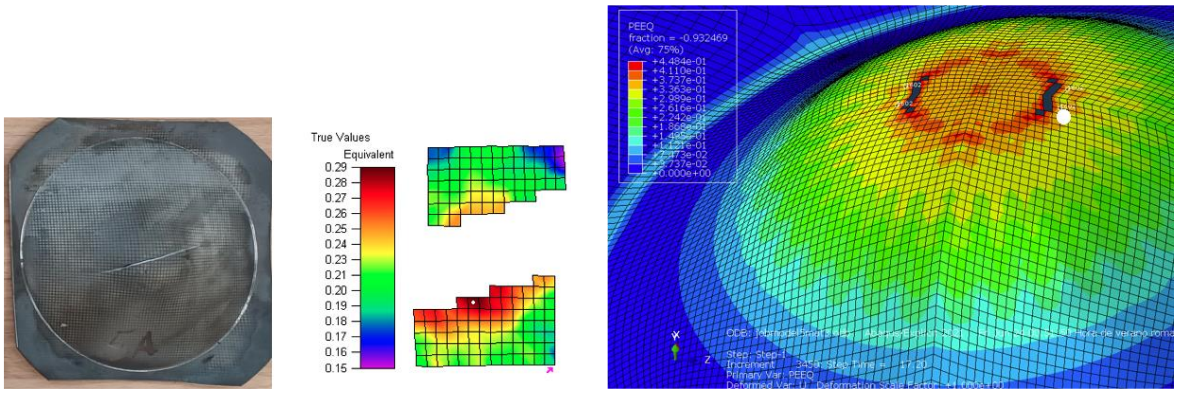

Figure 5-29. Nakajima test comparison for ε_p, showing experimental (a) vs. computational (b) results, with maximum values of 0.29 and 0.343 marked with a white dot, respectively. The data are provided by RINA Consulting – Centro Sviluppo Materiali.

Again, the standard criteria established in ISO 12004-2 [75], is replicated to find the latter. In this specific case, complexity arises as capturing both major and minor principal strain values in each simulation requires extracting these values from the deformed node elements that are perpendicular to the fracture zone. Then, both series of data, experimental and simulated, are approximated by a second-degree equation employing the least squares minimization technique. Finally, the relevant data pair of each simulation test is taken as the greatest and lowest values of both maximum and minimum strain approximated curves, which should ideally take place in the same element node.

By performing this procedure and comparing the experimental and the simulated data, the FLD error results can be found. The pairs of curves are shown in Figure 5-30.

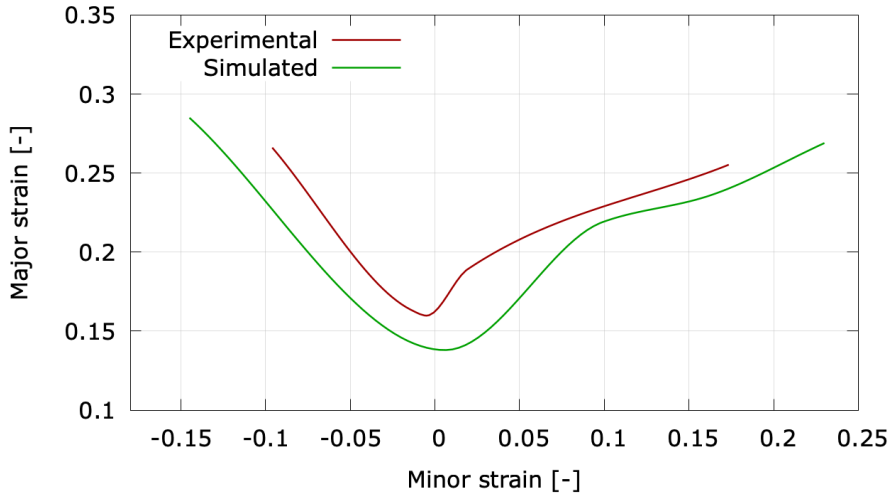

a)

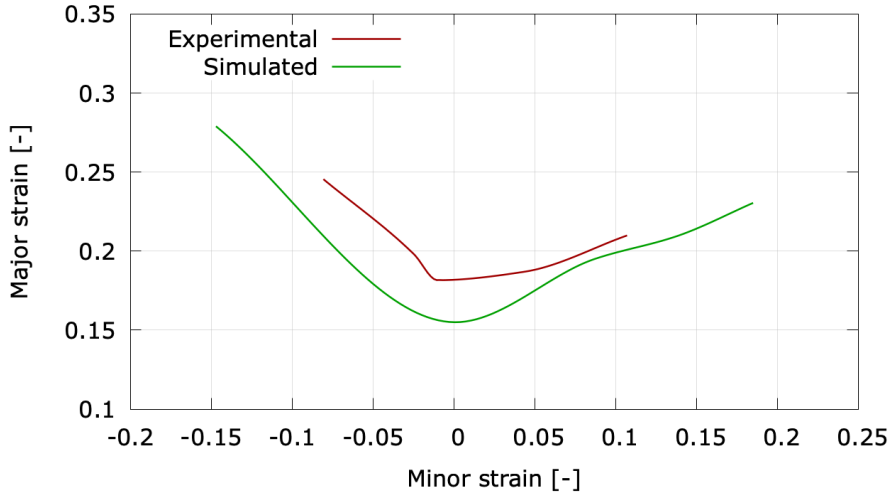

b)

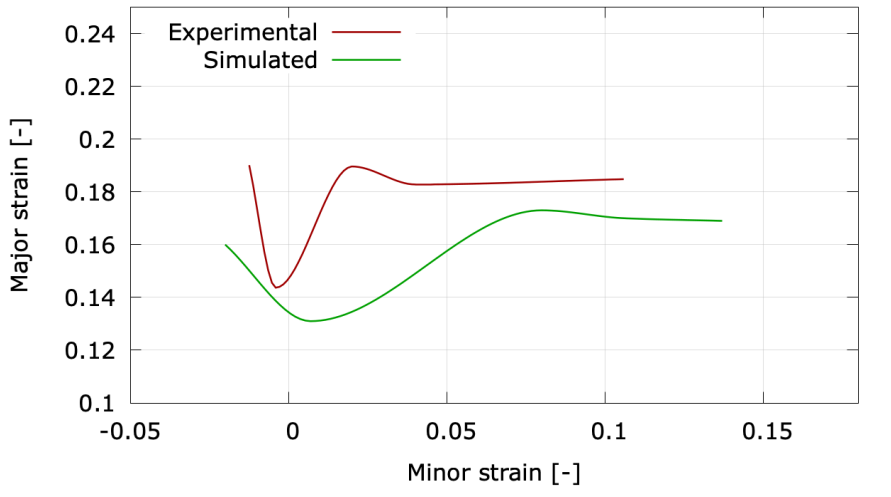

c)

Figure 5-30. Comparison of experimental and simulated FLD curves for alloy 410 (a), alloy 420 (b) and alloy 420ma (c).

On the whole, upon examining these results, they can be considered partially successful, as there is generally a good agreement between the pairs of data. There is, however, a notable

discrepancy in the case of alloy 420ma, where a significant gap exists between the simulated and the experimental curves. This mismatch is likely due to the absence of simulated data in the minor strain range from 0.0 to 0.08, which results in a loss of information regarding the actual fracture behavior of the material in that zone. When the global average error considering the three alloys is calculated, the outcome results in 13.9 %. This result has been notably affected by the large error found for alloy 3 (18.5 %), as previously explained, in contrast to those achieved for alloys 410 and 420 (12.4 % and 10.9 %, respectively), which are in a more common and acceptable range, considering the complex features of the ductile fracture phenomena aimed at being simulated in this paper. Also, it must be noted that the FLD curves found are, in theory, more conservative than the experimental ones. Nonetheless, it has been observed in posterior experimental testing that the experimental curves are, in some cases, too optimistic, finding that the fracture tends to occur before reaching the limits they predict. This would support the agreement of the simulated curves with the real behavior of the material.

In any case, the latter errors are considerably lower than the previous error found for the QoI ε_p comparison. This is probably due to the fact that not only a single point is taken to extract the given computational result but rather a set of them. This has a balancing effect on the numerical inaccuracies produced during the simulations. Consequently, it can be considered that the simulated models are, on the whole, validated at the sight of the latter findings.

5.4.2.3. FLSD vs FLD: improving fracture modeling

FLD ductile fracture criterion has been widely used for the simulation of forming processes in order to predict the onset of necking or fracture occurrence. Nonetheless, as pointed out by works such as [132], [133] or [134], some disagreements between these limit curves and the actual fracture behavior of metallic materials have been identified. Thus, these findings provide support for considering the use of the FLSD criterion based on stress as a relatively more favorable alternative. This criterion has been proved to bring some advantages, as the invariance of the limit curves themselves with respect to the thickness of the alloy sheets in comparison to the FLD criterion, or its notable capability to accurately predict necking in forming processes, as shown in [135] or [136], and further investigated in [137] or, also considering other kinds of extended stress-based FLC criteria, in [138].

The FLSD criterion relies on the concept of setting pairs of minor and major stresses shaping a limiting curve, such that if the stress state of the material is under it, the necking or fracture of the material will not happen. The procedure employed to extract these ductile fracture limiting curves is based on computational methods, due to the restriction and complexity of the experimental equipment needed to calculate these values, as explained previously. Alternatively, validated models can be used to find them by taking maximum and minimum in-plane stresses present on the elements at the onset of necking. Thus, once this technique is employed, the values for the FLSD curves for each alloy are found. These are shown in Figure 5-31.

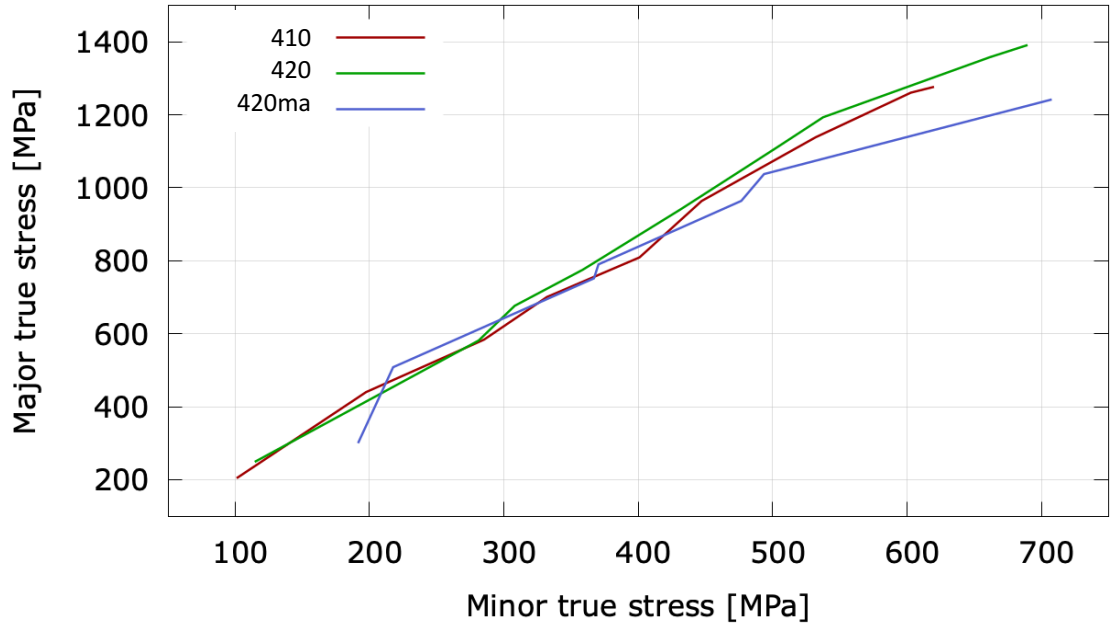

Figure 5-31. FLSD curves calculated for the studied Q&P-treated martensitic stainless steels.

It can be observed that the different Q&P-treated martensitic stainless steels share very similar values for their forming limits, with very few discrepancies observed at high minor stresses. Also, it must be noted that the fluctuations on each of the curves are due to the simulated nature of the extracted data and the numerical variations obtained in each of the elements from which the maximum and minimum values are sampled. Each of the FLSD curves, and consequently, the simulated alloys' forming limits, will undergo computational testing during the numerical tests of sheet cold stamping for manufacturing usual car parts in the next section (Section 5.4.3). This is regarded as a first testing bench for the proper prediction of the industrial procedure feasibility before any actual part gets physically into the assembly line.

5.4.3. Feasibility of the developed grades for stamping automotive parts

Aiming at testing the ductility limits of the material when undergoing cold forming processes, the simulation of the stamping procedure as part of the manufacturing of two different automotive parts has been numerically replicated, namely the B-pillar and the central transmission floor tunnel of a standard car.

As observed in Figure 5-32, the complexity related to the shape of both parts is uneven, since the pillar possesses a surface filled with numerous bends of a small radius and a much more intricate geometry in general in comparison to the tunnel part, subjecting the material to higher strains and stresses during the stamping, which can have critical consequences towards the success of the process. This makes the B-pillar a more challenging geometry for cold stamping, while the tunnel part represents, in relative terms, a moderately difficult one.

For these simulations, all three alloys are employed, making use of the already validated data to set up the ABAQUS models (Figure 5-32). In particular, they consist of a lower rigid die, fixed on the lower part, acting as the base, and an upper rigid die, moving at a standard speed of 1.25 mm/s, whereas the martensitic alloy sheet with 1.25 mm thickness is positioned in

between both at the start of the simulations, counting on approximately 38000 linear-S3R elements. The rest of the setup features for these models are replicated from those already described in Section 4.1.2. No guide pins are considered in the simulation setup, as the misalignment of the sheet during the deformation process is negligible. In the same way, the appearance of wrinkling is practically avoided without any additional parts due to the action of the forces exerted by the dies themselves as the part gets pressed.

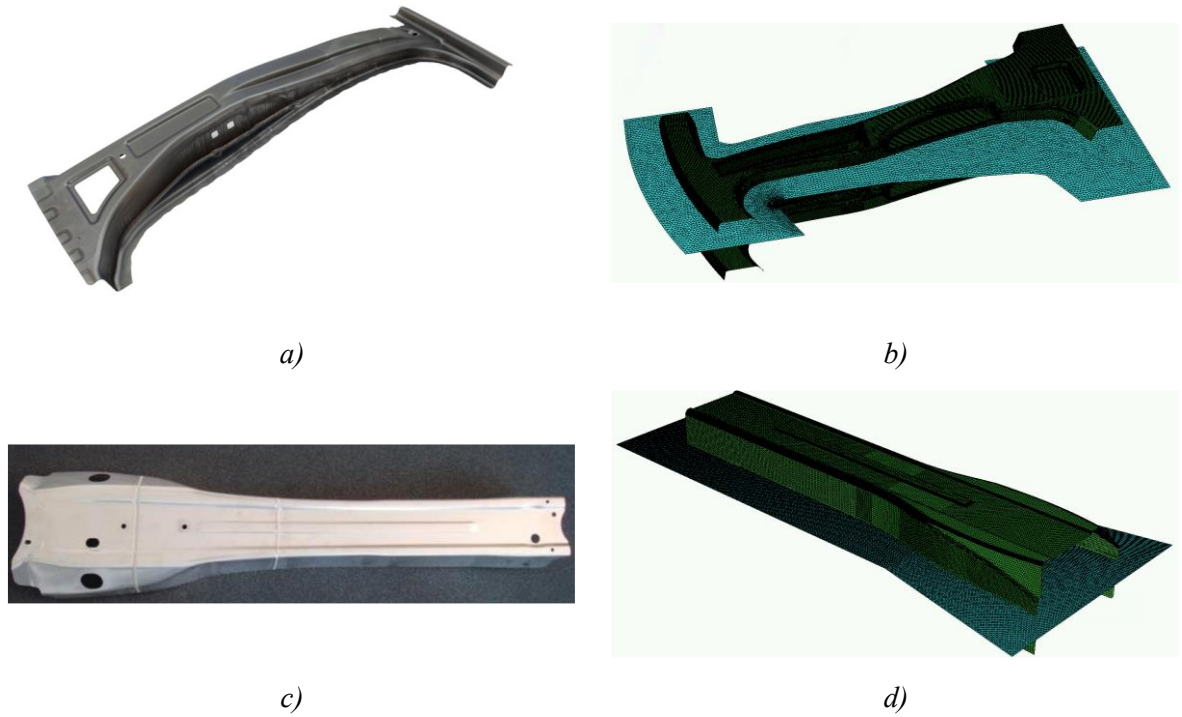

a) *b)*

c) *d)*

Figure 5-32. Actual final shape of the automotive parts whose stamping process is simulated, a) B-pillar and c) tunnel [139]. *Corresponding setup of the ABAQUS simulation models for both parts, b) B-pillar and d) tunnel.*

Representing outcomes for both simulations are collected in Figure 5-33 and Figure 5-35 for the B-pillar, and in Figure 5-34 and Figure 5-36 for the tunnel. No significant differences with regard to the final results considering the different alloys can be reported, as the widespread fracturing occurring in the run of the B-pillar is not avoided for any of the three materials. Likewise, the outcome of the models replicating the stamping process of the tunnel part is quite similar, at least in what concerns the non-onset of cracks in each Q&P martensitic stainless steel, having this already been predicted in view of the similarities observed in the found FLSD curves. Similarly, as expected due to the difference in complexity of the parts, there is a clear contrast between the forming processes of both car pieces, being far from successful in the case of the B-pillar, whereas the tunnel part does not show any fully damaged element. Therefore, according to these outcomes, it could be foreseen that, under the same cold stamping conditions, only the production of one of the latter seems feasible. It is important to notice that the springback issues are relevant during metal forming of stainless steels [140]. This topic has been out of scope of this thesis, since it is impossible to consider all the issues related with metalforming process. However, it should be noted that there is a body of research in the current literature clearly showing the springback effect can be significantly reduced in steel sheets by electrically single-pulsed current [141].

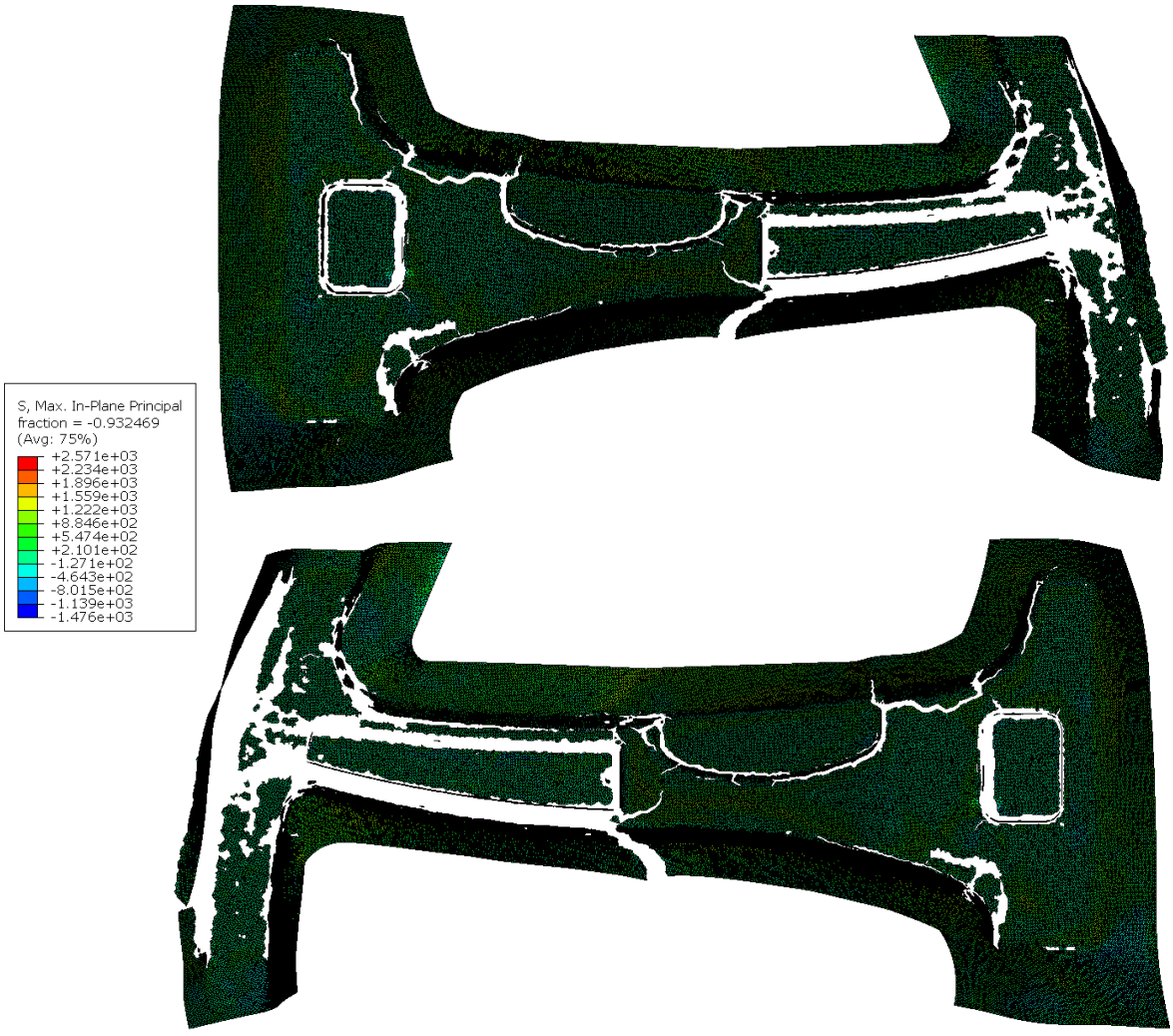

Figure 5-33. Example of final result of B-pillar stamping simulation, in this case for alloy 410.

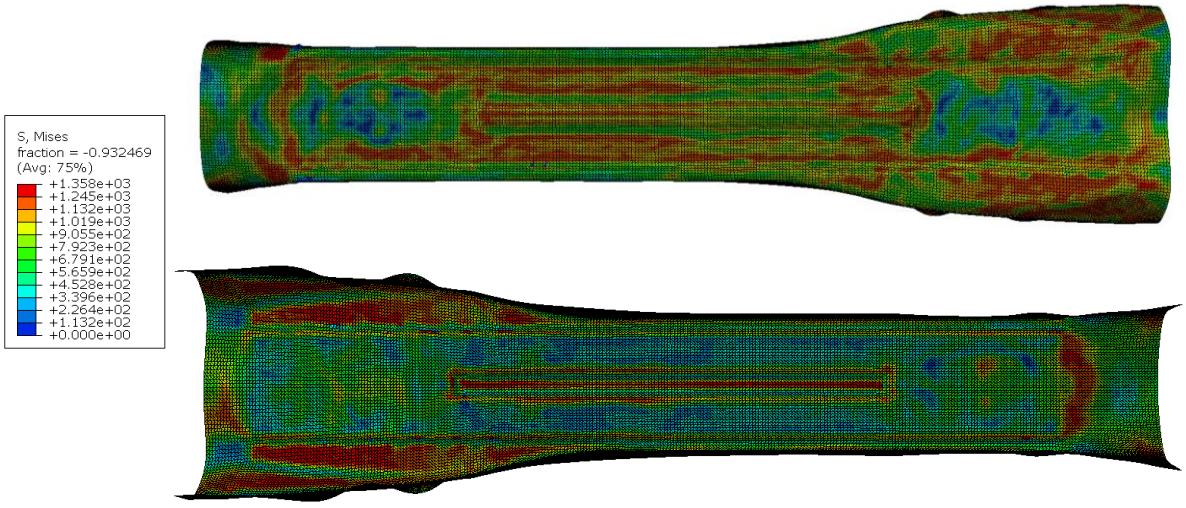

Figure 5-34. Example of final result of tunnel stamping simulation, in this case for alloy 410.

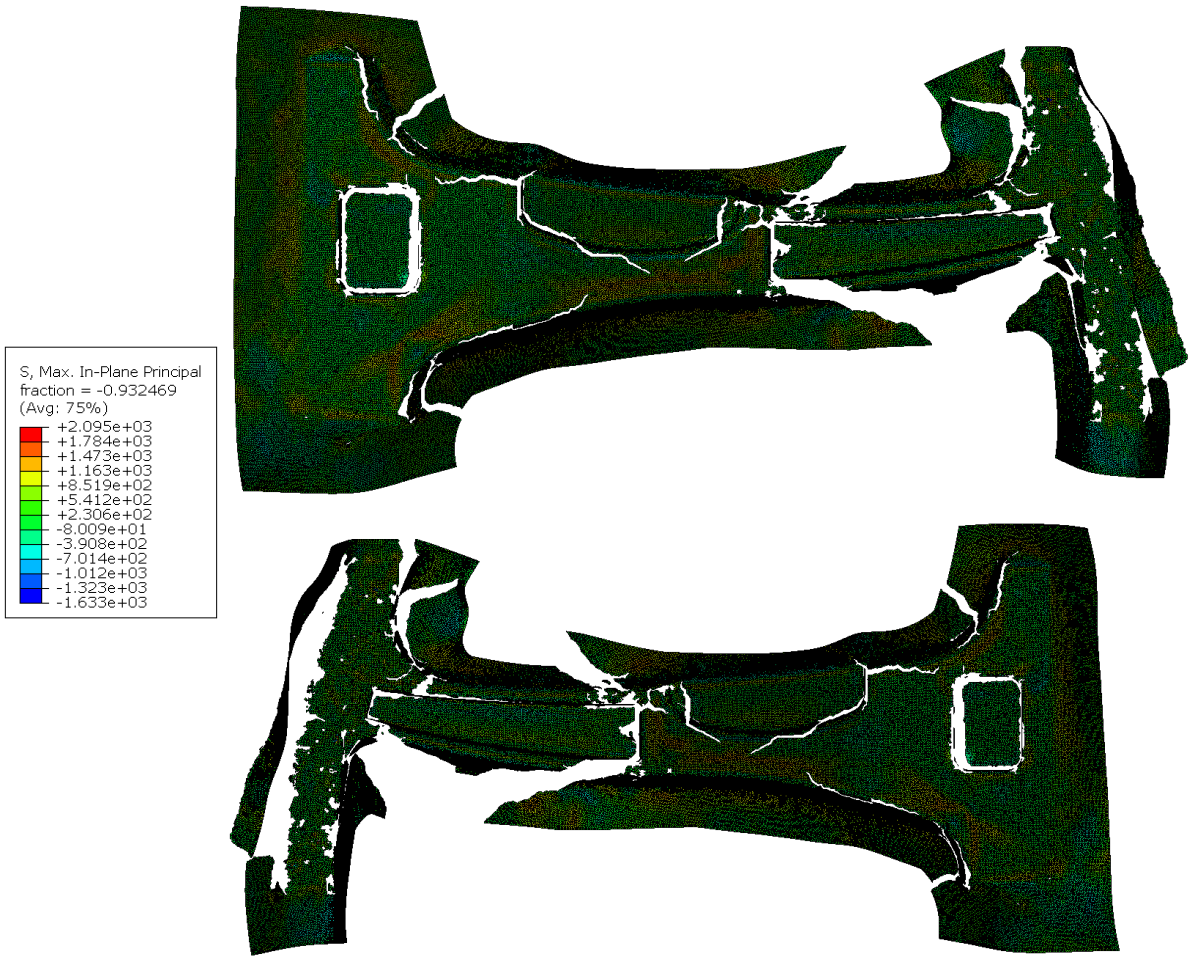

Figure 5-35. Example of final result of B-pillar stamping simulation, in this case for alloy 420ma.

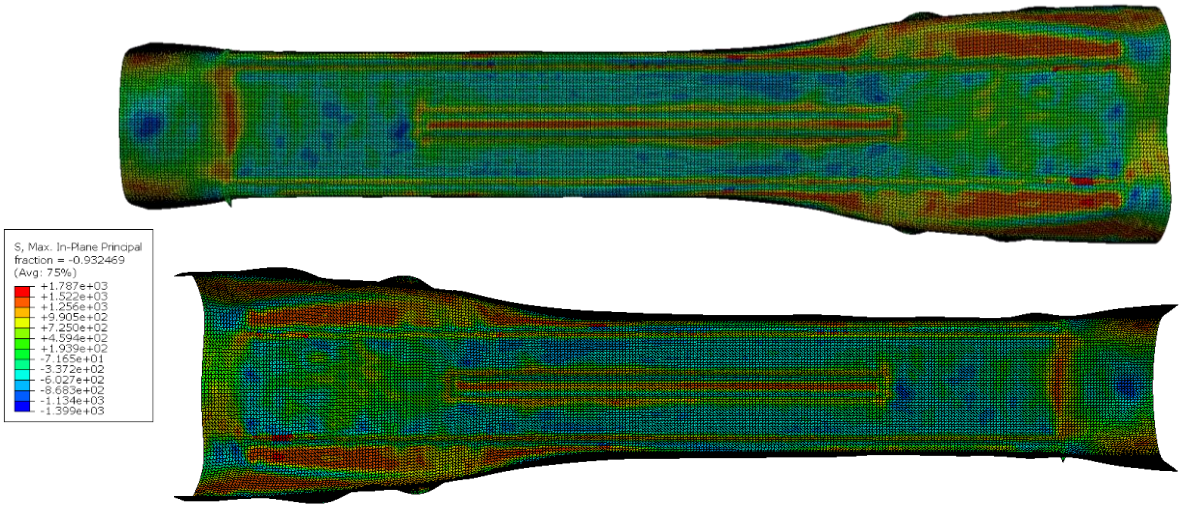

Figure 5-36. Example of final result of tunnel stamping simulation, in this case for alloy 420ma.

5.4.4. Conclusions to Section 5.4

From the formability characterization of the Q&P-treated martensitic stainless steels, both the Nakajima experiments and the computational approach, the following conclusions can be drawn:

- Nakajima experiments demonstrate satisfactory formability of martensitic stainless steels after Q&P treatment, albeit with lower performance compared to DP600 or TRIP700 steels. This acceptable formability is attributed to the increased content of retained austenite and TRIP effect.
- The procedure developed for the computational modelling of the Nakajima experiments consists of the J-C model coupled with FLSD curves. The obtained models are successfully validated with the data obtained from the Nakajima experiments.
- Altogether, the computational procedure is relatively fast and not heavily dependent on experimental data, which is something considered positive since these data must be necessarily extracted from expensive physical tests. Despite this simplification in the procedure, the method employed has been proven to be reliable in comparison to others when examined in previous research work.
- The developed computational procedure was implemented in the cold-forming of two automotive parts. The modeling reveals significant cracking during the cold forming of the complex-shaped B-pillar for all three studied alloys. In contrast, no damage elements were detected in the case of cold forming the simpler tunnel part for any of the three alloys. Therefore, the production of tunnel parts from Q&P-treated martensitic stainless steels appears feasible.
- These expectations align well with the prior experimental assessments of formability for the different alloys observed during the Nakajima tests campaign. Nonetheless, it will be necessary to validate these numerical stamping runs with physical tests to fully confirm the usefulness of the models.
- Finally, the proposed computational approach can be easily applied to predict the formability of other complex shape parts made of Q&P-treated martensitic stainless steels.

6. COST ANALYSIS & FEASABILITY

Stainless steel enjoys a solid and enduring reputation for structural durability, corrosion resistance and visual appeal in a wide range of applications and environments. While it may require an initial higher investment when compared with other materials, stainless steel's unique properties deliver long-term performance and economic benefits, including minimum downtime, reduced maintenance costs and reduced environmental impacts. The latter far outweigh higher initial material costs.

Life cycle cost (LCC) analysis quantifies all the initial and ongoing costs associated with a project or installation. It uses the standard accountancy principle of discounted cash flow to reduce all those costs to present day values. This allows a realistic comparison to be made of the options available and the potential long-term benefits of using stainless steel to be assessed against other material selections. The present-day value represents the amount of money which would have to be invested today in order to meet all the future operating costs – including running costs, maintenance, replacement and production lost through downtime. These are added to the initial costs to give the total LCC. The latter is traditionally calculated using an equation schematically presented in Figure 6-1.

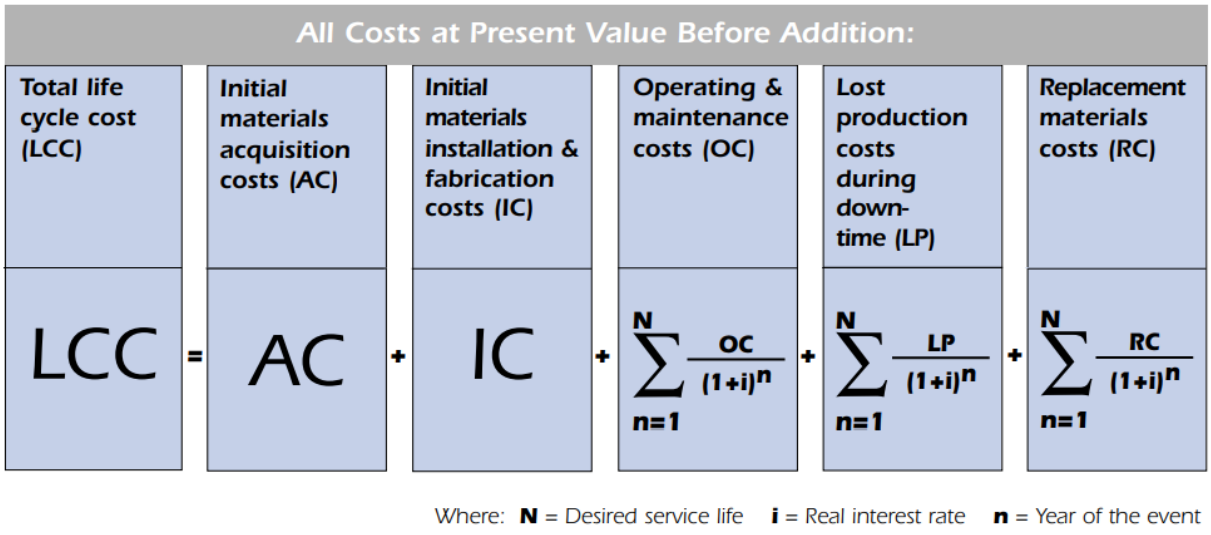

Figure 6-1. Calculation of total life cycle cost (LCC).

The present LCC analysis focuses entirely on the first half of the life cycle of steel and covers initial materials acquisition costs (AC) and initial materials fabrication costs (IC), i.e. the first stages of steel life. The following stages, such as operating and maintenance costs (OC) or replacement materials costs (RC) are not considered in the present analysis.

6.1. Production costs analysis

6.1.1. Initial material acquisition costs

The steel life begins with mining raw materials, which must then be carefully processed to ensure quality finished products that meet specifications. At a steel-making factory, the steel manufacturing process starts with the purchase of raw materials. They often have varying price points, and many variables are at play, causing this. The main contributing factors to the shifting

price of raw materials include sourcing the material, transportation, labor, and disasters (sudden and often devastating events, such as tornadoes, flooding, earthquakes, volcanic eruption, or any other natural phenomenon which can shut down mining and transportation instantly and for an extended period). In this work, three steel grades, with their chemical compositions presented in Table 6-1, have been considered and evaluated. Chemical compositions of other two grades currently manufactured by ACERINOX, austenitic stainless steel 1.4301 and martensitic stainless steel 1.4031, are also provided.

Table 6-1. Chemical composition of the analyzed alloys (in wt.%).

Alloy	C	Mn	Si	Cr	Ni	Al	N	Nb	Ti
410	0.2	0.7	0.35	12.5	0.20	0.01	0.03	-	-
420	0.3	0.7	0.35	13.0	0.20	0.01	0.03	-	-
420ma	0.3	3.0	0.35	13.0	0.20	0.01	0.03	0.05	0.05
1.4310 (AISI 301)	0.12	2.0	0.75	17.0	7.0	-	-	-	-
1.4031 (AISI 420)	0.4	1.0	0.75	13.0	-	0.01	0.08	-	-

The cost of the raw materials (Table 6-2) was estimated based on the data provided by the world centre for trading industrial metals, London Metal Exchange (https://www.lme.com), and it is subject to fluctuations[1].

Table 6-2. Cost of raw materials (€/tonn).

Fe	C	Mn	Si	Cr	Ni	Al	N	Nb	Ti
673	76	2134	2900	9580	25200	2330	490	40200	10650

Cost of the raw materials used for each alloy was estimated using (Eq. 6.1):

$$Cost = \sum_i cost\ of\ raw\ material_i \cdot content\ in\ alloy_i \qquad (Eq.\ 6.1)$$

The outcomes of the calculation are provided in Table 6-3 below. It is seen that the cost of the raw materials in the considered Q&P grades (1852 – 1955 €) is similar to that of the standard martensitic stainless steel (1860 €) and is well below the cost of austenitic stainless steel (4547 €). The alloy 420ma has a slightly higher cost (1955 €) than alloys 410 and 420 due to higher Mn content and microalloying by expensive Nb and Ti.

6.1.2. Cost of steel processing

The cost of steel casting, roughing and hot-rolling is nearly equal for all analyzed 5 grades. This cost is fixed at 477 €/tonn [142]. The energy consumption and carbon emission for all three steels are also equal. The main difference in energy consumption and cost will be at the next stage, the final heat treatments. The final heat treatments are different for all analyzed steels.

[1] The prices correspond to October 2022.

To calculate the energy consumed during the heat treatment of the Q&P grades, it is necessary to account for heat treatments that the grades studied in this work are subjected to after hot rolling and before cold rolling:

- Alloys 410 and 420: subcritical annealing at 740 °C for 24 h
- Alloy 420ma: intercritical annealing at 700 °C for 24 h

Table 6-3. Cost of the raw materials used for making each grade (€/tonn).

Alloy	Cost of raw materials used for making steel [€/tonn]
410	1852
420	1896
420ma	1955
1.4310 (AISI 301)	3949
1.4031 (AISI 420)	1860

These parameters along with the Q&P treatment parameters are summarized in Table 6-4.

Table 6-4. Final heat treatments applied to studied grades.

Alloy #	Annealing		QP treatment parameters				
	Temperature [°C]	Time [h]	Austenitization temperature [°C]	Austenitization time [min]	Quenching Temperature [°C]	Partitioning Temperature [°C]	Partitioning Time [min]
410	740	24	1100	15	160	450	5
420	740	24	1100	15	90	450	5
420ma	700	24	1100	15	20	450	5

The energy spent for heat treatments is determined mainly by heat treatment temperature and time. The maximum power of an average pusher type or beam walking type furnace used by steel manufacturers for annealing at 1200 °C is 636 kW/t [143]. The power at different temperatures can be estimated, assuming a linear dependence of power on temperature. The calculated power values at different considered temperatures are provided in Table 6-5.

The energy spent for the final heat treatments can be estimated using the equation (Eq. 6.2) below.

$$Energy = \sum_i time_i \cdot power\ at\ the\ given\ temperature_i \qquad \text{(Eq. 6.2)}$$

Table 6-5. Power of an average beam-walking furnace used in steel processing at different heat treatment temperatures.

HT temperature [°C]	Power [kW]
1100	593
740	399
700	377
450	243
20	0

The outcomes of the calculation are summarized in Table 6-5. The energy spent for heat treatment of the Q&P grades is nearly the same (9223.3 - 9740.7 kWh/tonn) since they have similar annealing, austenitization and partitioning conditions. The energy required for the final heat treatment of standard austenitic stainless steel is much lower (28.1 kWh/tonn). In comparison, the standard martensitic stainless steel requires a significantly higher amount of energy (11008.7 kWh/tonn) due to multiple long heat treatments. This information on the energy spent for the heat treatments of the standard stainless steels has been graciously supplied by ACERINOX.

The energy cost was taken as 0.1325 €/KWh (Spain). The calculations show that the standard martensitic stainless steel has the highest cost of the final heat treatments (1459 €/tonn), compared to the grades studied in this work (1222 – 1291 €/tonn) and standard austenitic stainless steel (4 €/tonn).

Table 6-6. Data on the energy spent for the final heat treatment and its cost.

Alloy	Q&P treatment is performed by steelmaker (for Q&P grades)		Q&P treatment is performed by end-user (for Q&P grades)	
	Energy spent for final heat treatment [kWh/tonn]	Cost of final heat treatment [€/tonn]	Energy spent for final heat treatment [kWh/tonn]	Cost of final heat treatment [€/tonn]
410	9740.7	1291	9572.3	1269
420	9740.7	1291	9572.3	1269
420ma	9223.3	1222	9054.9	1200
1.4310 (AISI 301)	28.1	4	-	-
1.4031 (AISI 420)	11008.7	1459	-	-

There can be a scenario when the final Q&P treatment of the studied grades is performed by the customer-end user (not the steelmaker). In this case, the energy spent for the final Q&P heat treatment (168.4 kWh/t) and the cost of Q&P treatment (22 €/tonn) must be subtracted. The final data are also presented in Table 6-6.

6.1.3. Other related costs

Other related costs to be taken into account include:

- Equipment maintenance costs: 37.6 €/tonn;
- Ecological taxation: 0.2 €/tonn;
- Waste treatment costs: 8.1 €/tonn.

In total: 45.9 €/tonn

These data are extracted from the ACERINOX annual report 2021 [144].

6.1.4. Summary of production costs analysis

The outcomes of the cost analysis (provided that the steelmaker performs the final Q&P treatment) are summarized in Table 6-7. It is seen that the acquisition of raw materials provides the highest contribution to the total cost of all alloys. The total cost of the Q&P grades (3665.9 – 3709.9 €/tonn) is significantly lower than that of the standard austenitic stainless steel (4475.9 €/tonn). Also, the studied grades have a lower cost than the standard martensitic stainless steel (3841.9 €/tonn).

Table 6-7. The outcomes of cost analysis (provided that the final Q&P treatment is performed by steelmaker).

Alloy	Acquisition of initial raw materials [€/tonn]	Casting and hot rolling [€/tonn]	Cost of final heat treatment [€/tonn]	Other related costs [€/tonn]	Total [€/tonn]
410	1852	477	1291	45.9	3665.9
420	1896	477	1291	45.9	3709.9
420ma	1955	477	1222	45.9	3699.9
1.4310 (AISI 301)	3949	477	4	45.9	4475.9
1.4031 (AISI 420)	1860	477	1459	45.9	3841.9

If the customer-end-user performs the final Q&P heat treatment, the final total costs of the grades studied in this work are reduced by 22 €/tonn. The final costs for this scenario are summarized in Table 6-8.

Table 6-8. The outcomes of cost analysis (provided that the final Q&P treatment is performed by customer-end-user).

Alloy #	Acquisition of initial raw materials [€/tonn]	Casting and hot rolling [€/tonn]	Cost of final heat treatment [€/tonn]	Other related costs [€/tonn]	Total [€/tonn]
3	1852	477	1269	45.9	3643.9
7	1896	477	1269	45.9	3687.9
10	1955	477	1200	45.9	3677.9
1.4310 (AISI 301)	3949	477	4	45.9	4475.9
1.4031 (AISI 420)	1860	477	1459	45.9	3841.9

6.2. Environmental effect

The steel industry is currently responsible for around 5 % of EU carbon emissions [145]. The primary and secondary steelmaking routes have very different carbon emission intensities. In the primary blast furnace - basic oxygen furnace (BF-BOF) steelmaking route, carbon is an energy input and is necessary to bin and remove oxygen from iron ore. This processing step in the blast furnace is the most carbon-intensive. It is responsible for over 50 % (~1.2 tonnCO_2/tonnsteel) of the total carbon emissions (~1.9 tonnCO_2/tonnsteel) of the final product (Figure 6-2). The contribution of casting/rolling/heat treatments is much lower, 0.1–0.3 tonnCO_2/tonnsteel (Figure 6-2). The secondary, electric arc furnace (EAF) steelmaking route is significantly electrified. Much smaller amounts of natural gas and coal are used in the EAF compared to the primary route. At the current average carbon intensity of electricity in the EU, the total emissions from EAF steel melting are ~0.2 tonnCO_2/tonnsteel (Figure 6-3). The emissions from electricity consumption are about 0.1–0.2 tonnCO_2/tonnsteel, and they can be avoided if the EAF used renewable electricity. The carbon emission from the casting/rolling/heat treatments is at the same level as in the primary steelmaking route.

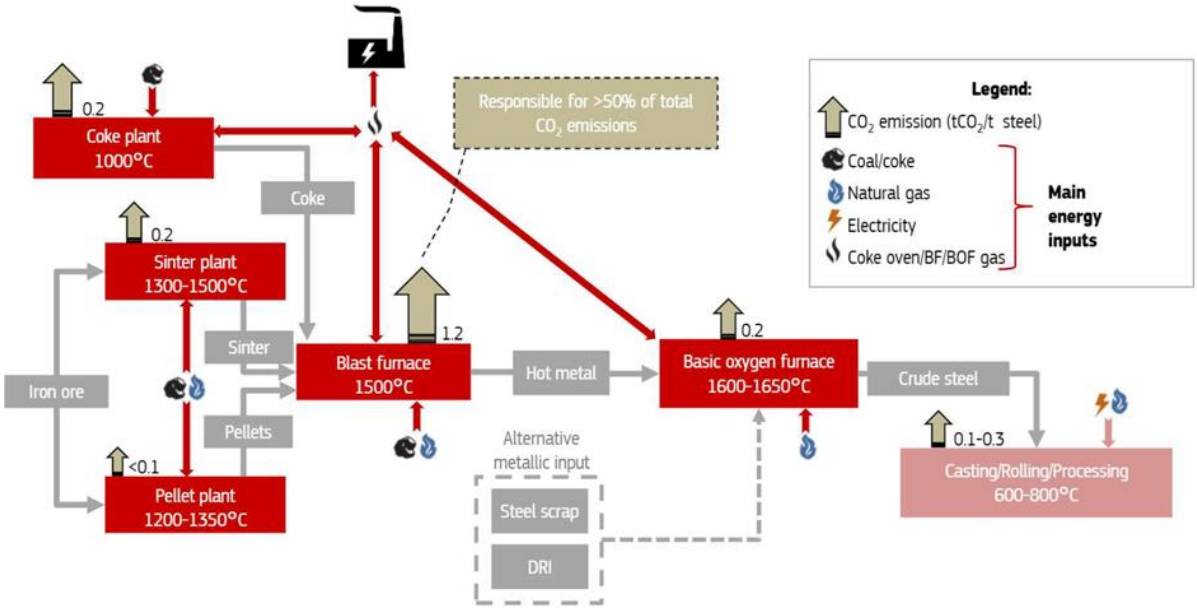

Figure 6-2. Simplified flow diagram and carbon emissions of the BF-BOF steelmaking route [145].

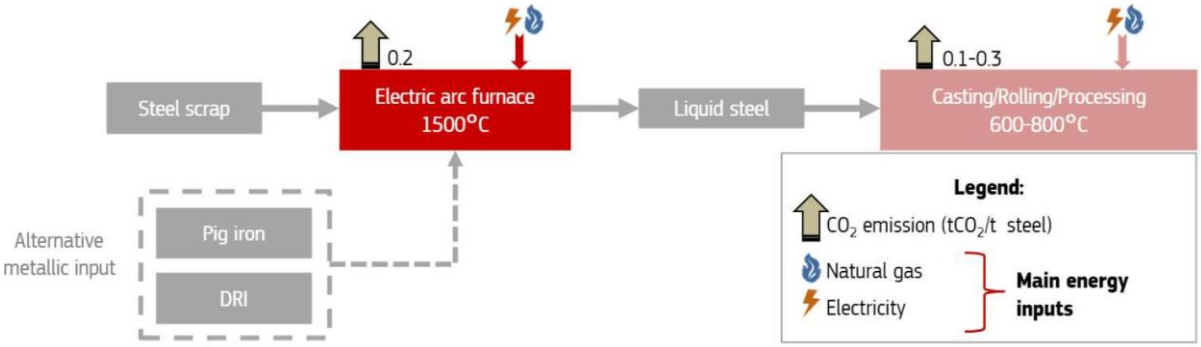

Figure 6-3. Simplified flow diagram and carbon emissions of the EAF steelmaking route [145].

The energy intensity of the Q&P process (168.4 kWh/tonn) is negligible compared even to the energy intensity of the final heat treatments of martensitic stainless steels (9054.9–11008.7 kWh/t). As carbon emissions are related to the energy consumption [145], implementation of the Q&P process will not directly affect the carbon emission in manufacturing martensitic stainless steels. However, it may have an indirect positive effect. The studied Q&P grades have reduced content of Ni: 0.2 wt.% vs. 7–9 wt. % in the standard austenitic stainless steels (Table 6-1). Production of raw Ni is a very carbon-intensive process. It produces 23 % of carbon emissions in the production process of raw materials for stainless steel (Figure 6-4) [146]. A simple calculation shows that the reduction of Ni content in manufactured stainless steel from 7 wt. % to 0.2 wt. % will reduce the raw material - related carbon emissions from 1.92 to 1.49 tonnCO_2/tonnsteel. It should also be noted that Ni is a very expensive metal (Table 6-2) which is fast becoming one of the world's most critical elements [147]. The political dimensions of Europe's dependence on foreign nickel suppliers were already highlighted in 2020 when Indonesia, the world's largest nickel producer, banned exports of the metal in order to increase investments in its domestic metal industry. Russia is another of the world's primary nickel exporters. Nickel's dramatic reduction or even

elimination in steel chemistry will make stainless steel cheaper to produce and also mean that EU stainless steel manufacturers are no longer reliant on third-party suppliers.

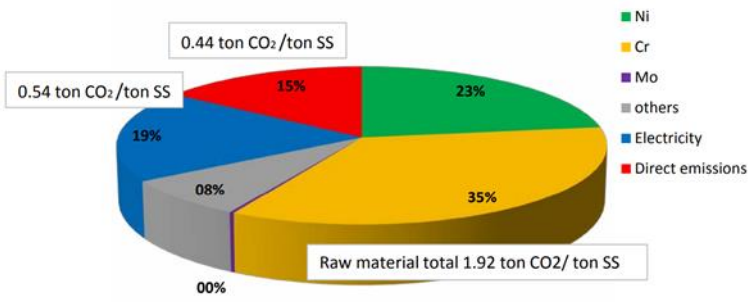

Figure 6-4. Distribution of CO_2 emissions [146].

6.3. Conclusion to Chapter 6

From the LCC analysis and the environmental effect review, the following conclusions can be drawn.

- In all analyzed steels, the highest contribution to total material cost is provided by the initial materials acquisition costs. It is followed by the cost of the final heat treatments and the cost of casting and hot rolling for the Q&P grades and the standard martensitic stainless steel.
- The cost of the standard austenitic stainless steel is significantly higher than that of the Q&P grades and the standard martensitic stainless steels due to the high cost of Ni. The studied Q&P grades show lower cost compared to the traditional martensitic stainless steel.
- The Q&P process demonstrates very low energy intensity and cost compared to other final heat treatments used in stainless steel manufacturing. Implementing the Q&P process into manufacturing would not significantly affect the final energy intensity and material cost.
- The Q&P process has no significant direct effect on carbon emissions. However, it may indirectly reduce manufacturing related-carbon emissions. The manufacturing of raw Ni is a very carbon-intensive process, and the Q&P grades are characterized by reduced Ni content. Replacing the standard austenitic stainless steel with any Q&P grade would reduce the raw material-related carbon emissions.

7. CONCLUSIONS

Several recent studies have demonstrated the viability of Q&P treatment for processing martensitic stainless steels showing an improved balance of high strength and sufficient ductility, particularly with a modified route involving quenching to room temperature for high carbon chemistry. In this thesis, the impact of alloy composition and Q&P heat treatment parameters on microstructure and basic mechanical properties is comprehensively studied, and critical application-related properties, such as fatigue performance and formability, are explored.
Three alloys with varying carbon and manganese content are subjected to Q&P heat treatments with varying parameters to identify the optimum Q&P treatment parameters. The microstructure and basic mechanical properties of the Q&P-treated alloys are examined, and the optimum Q&P parameters are identified. Large sheets are then processed using these optimum Q&P treatment conditions. Their microstructure, tensile properties, high cycle fatigue behavior and formability are investigated. Finally, LCC analysis of the Q&P-treated martensitic stainless steels in comparison to standard stainless steels is conducted, and the environmental effect of implementing Q&P treatment in the industrial process is also analyzed. Based on the outcomes of this work, the following general conclusions can be drawn:

- The microstructure of martensitic stainless steels is notably influenced by alloy chemistry and Q&P parameters. Higher partitioning temperature and time contribute to an increased volume fraction of retained austenite. Alloy composition, especially C and Mn content, plays a crucial role in determining the retained austenite volume fraction. Additionally, microalloying with Nb and Ti proves effective in reducing the prior austenite grain size. Physical simulation emerges as a valuable tool for identifying optimal Q&P parameters, facilitating large-scale predictions despite minor deviations.
- Existing equations for estimating carbon content in retained austenite present in Q&P-treated martensitic stainless steels using XRD measurements are deemed unreliable, prompting the need for a more robust experimental approach.
- Q&P-treated martensitic stainless steels demonstrate a favorable combination of increased strength and satisfactory tensile ductility compared to the commercial martensitic stainless steels. Optimum Q&P parameters lead to enhanced mechanical properties, exemplified by superior combinations such as σ_{UTS}= 1472 MPa and ε_t = 14.0 % reached in the large sheet of 420 alloy. It is demonstrated that the TRIP effect, driven by the high volume fraction of retained austenite, contributes to increased uniform elongation across all alloys. EBSD analysis indicates a limited role of crystallographic orientation in the transformation stability of retained austenite during tensile loading, while local misorientation values suggest the tempered martensitic matrix's high ability to accumulate plastic deformation.
- Q&P-treated martensitic stainless steels show satisfactory fatigue performance compared to conventional counterparts. Alloy 410 displays the best fatigue performance among studied Q&P-treated martensitic stainless steels, with a high σ_f/σ_{UTS} ratio of 0.24.
- Fatigue crack initiation predominantly occurs at the surface along martensite packet or block boundaries. MnS inclusions along with Fe_3C and complex (Ti,Nb) nanocarbides have no impact on the initiation process due to their small size. Crack growth along martensite packet or block boundaries results in surface striations, accompanied by debonding of elongated MnS inclusions. Microplastic deformation near the fatigue crack tip enhances local KAM values and induces localized transformation of retained austenite grains. This local TRIP effect may contribute to improved low cycle fatigue performance in Q&P-treated martensitic stainless steels compared to conventional counterparts.

- Nakajima experiments demonstrate sufficient formability of the Q&P-treated martensitic stainless steels, attributed to the presence of retained austenite and the TRIP effect during plastic deformation.
- Computational modelling, combining the J-C model with FLSD curves, is validated with Nakajima data, showing promising results in predicting formability during cold-stamping. The procedure is efficient and minimally reliant on expensive experimental data, offering reliability compared to alternative methods. Modeling indicates extensive cracking in B-pillar cold forming but feasibility in tunnel part production from Q&P-treated martensitic stainless steels, yet full validation requires physical tests. The proposed approach can be extended to predict formability in other complex parts made from Q&P-treated martensitic stainless steels.
- LCC analysis shows that initial materials acquisition costs contribute most to total material costs, followed by final heat treatments, casting, and hot rolling. Standard austenitic stainless steel is comparatively costly due to high nickel content, making Q&P grades more economically favorable than traditional martensitic stainless steel. The Q&P process exhibits low energy intensity and cost, suggesting minimal impact on overall manufacturing energy and material costs upon implementation. While the Q&P process has no direct effect on carbon emissions, its adoption may indirectly reduce manufacturing-related emissions by utilizing lower-carbon-content materials compared to standard austenitic stainless steel.

8. FUTURE WORK

The following areas of future work are envisioned:

- The present thesis underscores the importance of finding an appropriate methodology to measure carbon concentration in retained austenite in Q&P-treated martensitic stainless steels. To validate existing equations, the atom probe tomography (APT) technique can be utilized.
- The present thesis explores the high-cycle fatigue performance of Q&P-treated martensitic stainless steels. Future studies should delve into the effects of microstructural constituents (size, volume fraction, etc.) on the high-cycle fatigue resistance of the materials. Additionally, investigating low-cycle fatigue behavior of the Q&P-treated martensitic stainless steels is recommended.
- In this thesis, a computational approach was developed to assess the mechanical behavior of the Q&P-treated martensitic stainless steels during cold forming. Cold stamping simulations of two automotive parts, the B-pillar and tunnel, were conducted using the J-C constitutive model and the FLSD. The feasibility of the computational approach should be verified through experimental cold stamping of the B-pillar and tunnel.
- Fracture toughness of the Q&P-treated martensitic stainless steels is worthy of investigation due to its high relevance for automotive applications. The effect of microstructure on fracture behavior should be explored.
- No reports on dynamic/crash behavior of Q&P-treated martensitic stainless steels can be found in the literature up-to-date, despite its relevance to automotive applications. Therefore, it would be interesting to study their high strain rate behavior and crash resistance. The effect of individual microstructural constituents on high strain rate performance is worthy of investigation. Furthermore, strain rate sensitivity studies would provide valuable information on the mechanical behavior of Q&P-treated martensitic stainless steels.
- Weldability is of utmost importance for automotive applications. Therefore, it is recommended to investigate the weldability of Q&P-treated martensitic stainless steels.

9. REFERENCES

[1] M. Bonnett, 'Environmental Consciousness, Sustainability, and the Character of Philosophy of Education', *Studies in Philosophy and Education*, vol. 36, no. 3, pp. 333–347, 2017.

[2] X. Sun, F. Meng, J. Liu, J. McKechnie, and J. Yang, 'Life cycle energy use and greenhouse gas emission of lightweight vehicle – A body-in-white design', *Journal of Cleaner Production*, vol. 220, pp. 1–8, 2019.

[3] J. Speer, D. K. Matlock, B. C. De Cooman, and J. G. Schroth, 'Carbon partitioning into austenite after martensite transformation', *Acta Materialia*, vol. 51, no. 9, pp. 2611–2622, 2003.

[4] A. Kalhor, M. Soleimani, H. Mirzadeh, and V. Uthaisangsuk, 'A review of recent progress in mechanical and corrosion properties of dual phase steels', *Archives of Civil and Mechanical Engineering*, vol. 20, no. 3, pp. 1–14, 2020.

[5] H. Bhadeshia, R. Honeycombe, H. Bhadeshia, and R. Honeycombe, *Chapter 12 – Stainless Steel*, 4th ed. Elsevier Ltd, 2017.

[6] M. M. A. Bepari, 'Carburizing: A Method of Case Hardening of Steel', in *Comprehensive Materials Finishing*, vol. 2–3, Elsevier, 2017, pp. 71–106.

[7] A. Iversen and B. Leffler, 'Aqueous corrosion of stainless steels', in *Shreir's Corrosion*, Elsevier, 2010, pp. 1802–1878.

[8] A. J. Sedriks and O. S. Zaroog, 'Corrosion of Stainless Steels', in *Reference Module in Materials Science and Materials Engineering*, Elsevier, 2017.

[9] V. Kain, 'Stress corrosion cracking (SCC) in stainless steels', in *Stress corrosion cracking: Theory and practice*, Woodhead Publishing, 2011, pp. 199–244.

[10] H. M. Cobb, *The history of stainless steel*. ASM International, 2010.

[11] H. Bhadeshia and R. Honeycombe, 'Stainless Steel', *Steels: Microstructure and Properties*, pp. 343–376, 2017.

[12] W. M. Garrison and M. O. H. Amuda, 'Stainless Steels: Martensitic', in *Reference Module in Materials Science and Materials Engineering*, Elsevier, 2017.

[13] L. A. Espitia, L. Varela, C. E. Pinedo, and A. P. Tschiptschin, 'Cavitation erosion resistance of low temperature plasma nitrided martensitic stainless steel', *Wear*, vol. 301, no. 1–2, pp. 449–456, 2013.

[14] S. Morito, X. Huang, T. Furuhara, T. Maki, and N. Hansen, 'The morphology and crystallography of lath martensite in alloy steels', *Acta Materialia*, vol. 54, no. 19, pp. 5323–5331, 2006.

[15] H. Kitahara, R. Ueji, N. Tsuji, and Y. Minamino, 'Crystallographic features of lath martensite in low-carbon steel', *Acta Materialia*, vol. 54, no. 5, pp. 1279–1288, 2006.

[16] K. Okada, A. Shibata, Y. Takeda, and N. Tsuji, 'Crystallographic analysis of fatigue fracture initiation in 8Ni-0.1C martensitic steel', *International Journal of Fatigue*, vol. 143, p. 105921, 2021.

[17] Y. Tomita and K. Okabayashi, 'Effect of microstructure on strength and toughness of heat-treated low alloy structural steels', *Metallurgical Transactions A*, vol. 17, no. 7, pp. 1203–1209, 1986.

[18] Outokumpu, 'Handbook of Stainless Steel', pp. 1–89, 2013.

[19] S. Lampman, 'Fatigue and Fracture Properties of Stainless Steels', in *Fatigue and Fracture*, ASM International, 1996, pp. 712–732.

[20] T. B. Hilditch, T. de Souza, and P. D. Hodgson, 'Properties and automotive applications of advanced high-strength steels (AHSS)', in *Welding and Joining of Advanced High Strength Steels (AHSS)*, Elsevier, 2015, pp. 9–28.

[21] J. C. M. Farrar, 'Group C Martensitic and ferritic stainless steels', in *The Alloy Tree*, Woodhead Publishing, 2004, pp. 33–51.

[22] 'Standard Specification for Stainless Steel Bars and Shapes. ASTM Standard A276/A276M-17'

[23] D. S. Codd, 'Automotive Mass Reduction with Martensitic Stainless Steel', in *SAE 2011 World Congress and Exhibition*, Apr. 2011.

[24] J. Pearson, 'Atlas Steels Technical Handbook of Stainless Steels', 2021.

[25] W. M. Garrison and M. O. H. Amuda, 'Stainless Steels: Martensitic', in *Reference Module in Materials Science and Materials Engineering*, Elsevier, 2017.

[26] J. Speer, D. K. Matlock, B. C. De Cooman, and J. G. Schroth, 'Carbon partitioning into austenite after martensite transformation', *Acta Materialia*, vol. 51, no. 9, pp. 2611–2622, 2003.

[27] W. Bleck, X. Guo, and Y. Ma, 'The TRIP Effect and Its Application in Cold Formable Sheet Steels', *Steel Research International*, vol. 88, no. 10, p. 1700218, 2017.

[28] J. G. Speer, D. K. Matlock, L. Wang, and D. V. Edmonds, 'Quenched and Partitioned Steels', *Comprehensive Materials Processing*, vol. 1, pp. 217–225, 2014.

[29] J. G. Speer, E. De Moor, and A. J. Clarke, 'Critical assessment 7: Quenching and partitioning', *Materials Science and Technology*, vol. 31, no. 1, pp. 3–9, 2015.

[30] D. V. Edmonds, E. de Moor, D. K. Matlock, and J. G. Speer, 'Quenching and Partitioning Steel', in *Encyclopedia of Iron, Steel, and Their Alloys*, CRC Press, 2016, pp. 2776–2793.

[31] L. Wang and J. G. Speer, ‘Quenching and Partitioning Steel Heat Treatment’, *Metallography, Microstructure, and Analysis*, vol. 2, no. 4, pp. 268–281, 2013.

[32] M. Soleimani, A. Kalhor, and H. Mirzadeh, ‘Transformation-induced plasticity (TRIP) in advanced steels: A review’, *Materials Science and Engineering: A*, vol. 795, p. 140023, 2020.

[33] E. Pereloma, A. Gazder, and I. Timokhina, ‘Retained Austenite: Transformation-Induced Plasticity’, in *Encyclopedia of Iron, Steel, and Their Alloys*, CRC Press, 2016, pp. 3088–3103.

[34] P. Huyghe, S. Dépinoy, M. Caruso, D. Mercier, C. Georges, L. Malet, and S. Godet, ‘On the Effect of Q&P Processing on the Stretch-flange-formability of 0.2C Ultra-high Strength Steel Sheets’, *ISIJ International*, vol. 58, no. 7, pp. 1341–1350, 2018.

[35] P. Xia, I. Sabirov, J. Molina-Aldareguia, P. Verleysen, and R. Petrov, ‘Mechanical behavior and microstructure evolution of a quenched and partitioned steel during drop weight impact and punch testing’, *Materials Science and Engineering: A*, vol. 737, pp. 18–26, 2018.

[36] I. De Diego-Calderón, I. Sabirov, J. M. Molina-Aldareguia, C. Föjer, R. Thiessen, and R. H. Petrov, ‘Microstructural design in quenched and partitioned (Q&P) steels to improve their fracture properties’, *Materials Science and Engineering A*, vol. 657, pp. 136–146, 2016.

[37] I. De Diego-Calderón, D. De Knijf, J. M. Molina-Aldareguia, I. Sabirov, C. Föjer, and R. Petrov, ‘Effect of Q&P parameters on microstructure development and mechanical behaviour of Q&P steels’, *Revista de Metalurgia*, vol. 51, no. 1, p. e035, 2015.

[38] H. Elsayed, A. Drexler, F. Warchomicka, I. Traxler, J. Domitner, M. Galler, R. Vallant, and C. Sommitsch, ‘Resistance of Quench and Partitioned Steels Against Hydrogen Embrittlement’, *Journal of Materials Engineering and Performance*, vol. 32, no. 11, pp. 5186–5200, 2023.

[39] L. Wang and W. Feng, ‘Development and Application of Q&P Sheet Steels’, in *Advanced Steels*, Y. Weng, H. Dong, and Y. Gan, Eds., Berlin, Heidelberg: Springer Berlin Heidelberg, 2011, pp. 255–258.

[40] G. A. Thomas and J. F. Hansman, ‘Development, design, and industrial launch of next-generation steel’, in *Proceedings of the AISTech 2017 Conference*, Nashville, USA, May 2017, pp. 11–18.

[41] L. Yuan, D. Ponge, J. Wittig, P. Choi, J. A. Jiménez, and D. Raabe, ‘Nanoscale austenite reversion through partitioning, segregation and kinetic freezing: Example of a ductile 2GPa Fe–Cr–C steel’, *Acta Materialia*, vol. 60, no. 6–7, pp. 2790–2804, 2012.

[42] J. Mola and B. C. De Cooman, ‘Quenching and Partitioning (Q&P) Processing of Martensitic Stainless Steels’, *Metallurgical and Materials Transactions A*, vol. 44, no. 2, pp. 946–967, 2013.

[43] T. Tsuchiyama, J. Tobata, T. Tao, N. Nakada, and S. Takaki, 'Quenching and partitioning treatment of a low-carbon martensitic stainless steel', *Materials Science and Engineering: A*, vol. 532, pp. 585–592, 2012.

[44] J. Tobata, K.-L. Ngo-Huynh, N. Nakada, T. Tsuchiyama, and S. Takaki, 'Role of Silicon in Quenching and Partitioning Treatment of Low-carbon Martensitic Stainless Steel', *ISIJ International*, vol. 52, no. 7, pp. 1377–1382, 2012.

[45] S.-Y. Lu, K.-F. Yao, Y.-B. Chen, M.-H. Wang, N. Chen, and X.-Y. Ge, 'Effect of quenching and partitioning on the microstructure evolution and electrochemical properties of a martensitic stainless steel', *Corrosion Science*, vol. 103, pp. 95–104, 2016.

[46] S. Barella, A. Gruttadauria, J. T. O. Menezes, E. M. Castrodeza, S. E. Quaini, C. Pelligra, and E. A. McNally, 'The Reliability of Single-Step and Double-Step Quench and Partitioning Heat Treatments on an AISI 420A Low Carbon Martensitic Stainless Steel', *Metallurgical and Materials Transactions A*, vol. 54, no. 10, pp. 3957–3972, 2023.

[47] Q. Huang, C. Schröder, H. Biermann, O. Volkova, and J. Mola, 'Influence of Martensite Fraction on Tensile Properties of Quenched and Partitioned (Q&P) Martensitic Stainless Steels', *Steel Research International*, vol. 87, no. 8, pp. 1082–1094, 2016.

[48] S. Dieck, P. Rosemann, A. Kromm, and T. Halle, 'Reversed austenite for enhancing ductility of martensitic stainless steel', in *IOP Conference Series: Materials Science and Engineering*, IOP Publishing, Mar. 2017, p. 012034.

[49] J. Mola and B. C. De Cooman, 'Quenching and partitioning (Q&P) processing of martensitic stainless steels', *Metallurgical and Materials Transactions A: Physical Metallurgy and Materials Science*, vol. 44, no. 2, pp. 946–967, 2013.

[50] C. Celada-Casero, F. Vercruysse, B. Linke, A. Smith, P. Kok, J. Sietsma, and M. J. Santofimia, 'Analysis of work hardening mechanisms in Quenching and Partitioning steels combining experiments with a 3D micro-mechanical model', *Materials Science and Engineering A*, vol. 846, 2022.

[51] C. Celada-Casero, C. Kwakernaak, J. Sietsma, and M. J. Santofimia, 'The influence of the austenite grain size on the microstructural development during quenching and partitioning processing of a low-carbon steel', *Materials & Design*, vol. 178, p. 107847, 2019.

[52] C. Y. Kung and J. J. Rayment, 'An examination of the validity of existing empirical formulae for the calculation of ms temperature', *Metallurgical Transactions A*, vol. 13, no. 2, pp. 328–331, 1982.

[53] S. Dieck, P. Rosemann, A. Kromm, and T. Halle, 'Reversed austenite for enhancing ductility of martensitic stainless steel', in *IOP Conference Series: Materials Science and Engineering*, IOP Publishing, Mar. 2017, p. 012034.

[54] J. Webel, H. Mohrbacher, E. Detemple, D. Britz, and F. Mücklich, 'Quantitative analysis of mixed niobium-titanium carbonitride solubility in HSLA steels based on atom probe

tomography and electrical resistivity measurements', *Journal of Materials Research and Technology*, vol. 18, pp. 2048–2063, 2022.

[55] C. Capdevila, C. García-Mateo, F. G. Caballero, and C. García de Andrés, 'Proposal of an empirical formula for the austenitising temperature', *Materials Science and Engineering A*, vol. 386, no. 1–2, pp. 354–361, 2004.

[56] T. Nyyssönen, M. Isakov, P. Peura, and V. T. Kuokkala, 'Iterative Determination of the Orientation Relationship Between Austenite and Martensite from a Large Amount of Grain Pair Misorientations', *Metallurgical and Materials Transactions A: Physical Metallurgy and Materials Science*, vol. 47, no. 6, pp. 2587–2590, 2016.

[57] M. J. Santofimia, R. H. Petrov, L. Zhao, and J. Sietsma, 'Microstructural analysis of martensite constituents in quenching and partitioning steels', *Materials Characterization*, vol. 92, pp. 91–95, 2014.

[58] C. Suryanarayana and M. G. Norton, 'X-Rays and Diffraction', in *X-Ray Diffraction*, Springer US, 1998, pp. 3–19.

[59] Q. Hou, Z. Huang, and J. Wang, 'Application of Rietveld refinement to investigate the high chromium white cast iron austempered at different temperatures', *Journal of Iron and Steel Research International*, vol. 16, no. 4, pp. 33–38, 2009.

[60] D. S. Tsai, T. S. Chin, S. E. Hsu, and M. P. Hung, 'A Simple Method for the Determination of Lattice Parameters from Powder X-ray Diffraction Data', *Materials Transactions, JIM*, vol. 30, no. 7, pp. 474–479, 1989.

[61] A. Bojack, L. Zhao, P. F. Morris, and J. Sietsma, 'In Situ Thermo-magnetic Investigation of the Austenitic Phase During Tempering of a 13Cr6Ni2Mo Supermartensitic Stainless Steel', *Metallurgical and Materials Transactions A*, vol. 45, no. 13, pp. 5956–5967, 2014.

[62] L. Zhao, N. H. van Dijk, A. J. E. Lefering, and J. Sietsma, 'Magnetic detection of small fractions of ferromagnetic martensite within the paramagnetic austenite matrix of TWIP steel', *Journal of Materials Science*, vol. 48, no. 4, pp. 1474–1479, 2013.

[63] S. Amelinckx and J. Van Landuyt, 'Transmission Electron Microscopy', in *Encyclopedia of Physical Science and Technology*, Elsevier, 2003, pp. 53–87.

[64] ASTM International, 'ASTM E8 / E8M-09. Standard Test Methods for Tension Testing of Metallic Materials'

[65] ISO, 'ISO 1099:2017 - Metallic materials — Fatigue testing — Axial force-controlled method', 2017

[66] K. Wang, Y. Jin, B. Zhu, and Y. Zhang, 'Investigation on cracking characteristics of Al–Si coating on hot stamping boron steel parts based on surface strain analysis', *Surface and Coatings Technology*, vol. 309, pp. 282–294, 2017.

[67] L. Yan, L. Yuxi, Y. Mingshun, Y. Qilong, and C. Fengkui, 'Analyzing the thermal mechanical coupling of 40Cr cold roll-beating forming process based on the Johnson-Cook dynamic constitutive equation', *International Journal of Heat and Technology*, vol. 33, no. 3, pp. 51–58, 2015.

[68] A. M. Aghdami and B. Davoodi, 'An inverse analysis to identify the Johnson-Cook constitutive model parameters for cold wire drawing process', *Mechanics and Industry*, vol. 21, no. 5, p. 527, 2020.

[69] N. Ben, Q. Zhang, H. Choi, K. Bandyopadhyay, and M. G. Lee, 'Experimental and finite element analysis on oscillating cold forming in consideration of nonlinear loading-unloading-reloading behavior', *Journal of Manufacturing Processes*, vol. 36, pp. 520–534, 2018.

[70] S. Panich, V. Uthaisangsuk, J. Juntaratin, and S. Suranuntchai, 'Determination of forming limit stress diagram for formability prediction of SPCE 270 steel sheet', *Journal of Metals, Materials and Minerals*, vol. 21, no. 1, pp. 19–27, 2011.

[71] A. Shrot and M. Bäker, 'Determination of Johnson–Cook parameters from machining simulations', *Computational Materials Science*, vol. 52, no. 1, pp. 298–304, 2012.

[72] H. Li, L. He, G. Zhao, and L. Zhang, 'Constitutive relationships of hot stamping boron steel B1500HS based on the modified Arrhenius and Johnson-Cook model', *Materials Science and Engineering A*, vol. 580, pp. 330–348, 2013.

[73] A. Banerjee, S. Dhar, S. Acharyya, D. Datta, and N. Nayak, 'Determination of Johnson cook material and failure model constants and numerical modelling of Charpy impact test of armour steel', *Materials Science and Engineering A*, vol. 640, pp. 200–209, 2015.

[74] ISO Central, 'Metallic materials — Determination of forming-limit curves for sheet and strip — Part 1: Measurement and application of forming-limit diagrams in the press shop, Standard ISO 12004-1:2020', Geneva, 2020.

[75] ISO Central, 'Metallic materials — Determination of forming-limit curves for sheet and strip — Part 2: Determination of forming-limit curves in the laboratory, Standard ISO 12004-2:2021', Geneva, 2021.

[76] M. Murugesan and D. Jung, 'Johnson Cook Material and Failure Model Parameters Estimation of AISI-1045 Medium Carbon Steel for Metal Forming Applications', *Materials*, vol. 12, no. 4, p. 609, 2019.

[77] M. Hunkel, 'Segregations in Steels during Heat Treatment – A Consideration along the Process Chain', *HTM Journal of Heat Treatment and Materials*, vol. 76, no. 2, pp. 79–104, 2021.

[78] P. Xia, F. Vercruysse, C. Celada-Casero, P. Verleysen, R. H. Petrov, I. Sabirov, J. M. Molina-Aldareguia, *et al.*, 'Effect of alloying and microstructure on formability of advanced high-strength steels processed via quenching and partitioning', *Materials Science and Engineering A*, vol. 831, no. July 2021, p. 142217, 2022.

[79] E. Pereloma, A. Gazder, and I. Timokhina, 'Retained Austenite: Transformation-Induced Plasticity', in *Encyclopedia of Iron, Steel, and Their Alloys*, CRC Press, 2016, pp. 3088–3103.

[80] J. Xing, G. Zhu, B. Wu, H. Ding, and H. Pan, 'Effect of Ti Addition on the Precipitation Mechanism and Precipitate Size in Nb-Microalloyed Steels', *Metals*, vol. 12, no. 2, p. 245, 2022.

[81] A. G. Kostryzhev, O. O. Marenych, C. R. Killmore, and E. V. Pereloma, 'Strengthening Mechanisms in Thermomechanically Processed NbTi-Microalloyed Steel', *Metallurgical and Materials Transactions A*, vol. 46, no. 8, pp. 3470–3480, 2015.

[82] H. Zhang and H. Xiong, 'First-principles study of NbC heterogeneous nucleation on TiC vs. TiN in microalloy steel', *Ironmaking & Steelmaking*, vol. 47, no. 1, pp. 77–83, 2020.

[83] S. Morito, H. Saito, T. Ogawa, T. Furuhara, and T. Maki, 'Effect of austenite grain size on the morphology and crystallography of lath martensite in low carbon steels', *ISIJ International*, vol. 45, no. 1, pp. 91–94, 2005.

[84] P. Xia, F. Vercruysse, R. Petrov, I. Sabirov, M. Castillo-Rodríguez, and P. Verleysen, 'High strain rate tensile behavior of a quenching and partitioning (Q&P) Fe-0.25C-1.5Si-3.0Mn steel', *Materials Science and Engineering A*, vol. 745, pp. 53–62, 2019.

[85] J. Hidalgo, K. O. Findley, and M. J. Santofimia, 'Thermal and mechanical stability of retained austenite surrounded by martensite with different degrees of tempering', *Materials Science and Engineering A*, vol. 690, no. November 2016, pp. 337–347, 2017.

[86] M. E. McHenry and D. E. Laughlin, 'Magnetic Properties of Metals and Alloys', in *Physical Metallurgy: Fifth Edition*, vol. 1, Elsevier, 2014, pp. 1881–2008.

[87] P. Oxley, J. Goodell, and R. Molt, 'Magnetic properties of stainless steels at room and cryogenic temperatures', *Journal of Magnetism and Magnetic Materials*, vol. 321, no. 14, pp. 2107–2114, 2009.

[88] P. J. Jacques, S. Allain, O. Bouaziz, A. De, A. F. Gourgues, B. M. Hance, Y. Houbaert, *et al.*, 'On measurement of retained austenite in multiphase TRIP steels results of blind round robin test involving six different techniques', *Materials Science and Technology*, vol. 25, no. 5, pp. 567–574, 2009.

[89] N. H. Van Dijk, A. M. Butt, L. Zhao, J. Sietsma, S. E. Offerman, J. P. Wright, and S. Van Der Zwaag, 'Thermal stability of retained austenite in TRIP steels studied by synchrotron X-ray diffraction during cooling', *Acta Materialia*, vol. 53, no. 20, pp. 5439–5447, 2005.

[90] D. Dyson and B. Holmes, 'Effect of alloying additions on the lattice parameter of austenite', *Journal of the Iron and Steel Institute*, vol. 208, no. 5, pp. 469–474, 1970.

[91] S. Ghosh, P. Kaikkonen, V. Javaheri, A. Kaijalainen, I. Miettunen, M. Somani, J. Kömi, and S. Pallaspuro, 'Design of tough, ductile direct quenched and partitioned advanced

high-strength steel with tailored silicon content', *Journal of Materials Research and Technology*, vol. 17, pp. 1390–1407, 2022.

[92] B. Denand, V. A. Esin, M. Dehmas, G. Geandier, S. Denis, T. Sourmail, and E. Aeby-Gautier, 'Carbon content evolution in austenite during austenitization studied by in situ synchrotron X-ray diffraction of a hypoeutectoid steel', *Materialia*, vol. 10, p. 100664, 2020.

[93] H. K. D. H. Bhadeshia, 'Theory and significance of retained austenite in steels - PhD Thesis', University of Cambridge, 1980.

[94] W. Bleck, X. Guo, and Y. Ma, 'The TRIP Effect and Its Application in Cold Formable Sheet Steels', *Steel Research International*, vol. 88, no. 10, p. 1700218, 2017.

[95] B. He, 'On the factors governing austenite stability: Intrinsic versus extrinsic', *Materials*, vol. 13, no. 15, pp. 1–31, 2020.

[96] A. Kumar, A. Dutta, S. K. Makineni, M. Herbig, R. H. Petrov, and J. Sietsma, 'In-situ observation of strain partitioning and damage development in continuously cooled carbide-free bainitic steels using micro digital image correlation', *Materials Science and Engineering A*, vol. 757, pp. 107–116, 2019.

[97] I. De Diego-Calderón, M. J. Santofimia, J. M. Molina-Aldareguia, M. A. Monclús, and I. Sabirov, 'Deformation behavior of a high strength multiphase steel at macro- and micro-scales', *Materials Science and Engineering A*, vol. 611, pp. 201–211, 2014.

[98] M. J. Santofimia, L. Zhao, and J. Sietsma, 'Overview of Mechanisms Involved During the Quenching and Partitioning Process in Steels', *Metallurgical and Materials Transactions A*, vol. 42, no. 12, pp. 3620–3626, 2011.

[99] A. Grajcar, A. Skowronek, and K. Radwański, 'Mechanical behavior and stability of dispersed retained austenite in thermomechanically rolled and isothermally-treated TRIP-aided multiphase steel', *Materials Science and Engineering A*, vol. 830, p. 142300, 2022.

[100] C. B. Finfrock, M. M. Thrun, D. Bhattacharya, T. J. Ballard, A. J. Clarke, and K. D. Clarke, 'Strain Rate Dependent Ductility and Strain Hardening in Q&P Steels', *Metallurgical and Materials Transactions A*, vol. 52, no. 3, pp. 928–942, 2021.

[101] O. Muránsky, P. Šittner, J. Zrník, and E. C. Oliver, 'In situ neutron diffraction investigation of the collaborative deformation-transformation mechanism in TRIP-assisted steels at room and elevated temperatures', *Acta Materialia*, vol. 56, no. 14, pp. 3367–3379, 2008.

[102] D. De Knijf, C. Föjer, L. A. I. Kestens, and R. Petrov, 'Factors influencing the austenite stability during tensile testing of Quenching and Partitioning steel determined via in-situ Electron Backscatter Diffraction', *Materials Science and Engineering A*, vol. 638, pp. 219–227, 2015.

[103] R. Blondé, E. Jimenez-Melero, L. Zhao, J. P. Wright, E. Brück, S. Van Der Zwaag, and N. H. Van Dijk, 'High-energy X-ray diffraction study on the temperature-dependent mechanical stability of retained austenite in low-alloyed TRIP steels', *Acta Materialia*, vol. 60, no. 2, pp. 565–577, 2012.

[104] Y. Wang, R. Li, X. Zuo, N. Chen, and Y. Rong, 'The twice softening of martensitic matrix in Q–P–T steels and its effect on ductility', *Heat Treatment and Surface Engineering*, vol. 1, no. 1–2, pp. 2–10, 2019.

[105] Y. Tomita and K. Okabayashi, 'Effect of microstructure on strength and toughness of heat-treated low alloy structural steels', *Metallurgical Transactions A*, vol. 17, no. 7, pp. 1203–1209, 1986.

[106] I. De Diego-Calderón, D. De Knijf, M. A. Monclús, J. M. Molina-Aldareguia, I. Sabirov, C. Föjer, and R. H. Petrov, 'Global and local deformation behavior and mechanical properties of individual phases in a quenched and partitioned steel', *Materials Science and Engineering A*, vol. 630, pp. 27–35, 2015.

[107] M. Calcagnotto, D. Ponge, E. Demir, and D. Raabe, 'Orientation gradients and geometrically necessary dislocations in ultrafine grained dual-phase steels studied by 2D and 3D EBSD', *Materials Science and Engineering A*, vol. 527, no. 10–11, pp. 2738–2746, 2010.

[108] D. Raabe, B. Sun, A. Kwiatkowski Da Silva, B. Gault, H. W. Yen, K. Sedighiani, P. Thoudden Sukumar, *et al.*, 'Current Challenges and Opportunities in Microstructure-Related Properties of Advanced High-Strength Steels', *Metallurgical and Materials Transactions A*, vol. 51, no. 11, pp. 5517–5586, 2020.

[109] G. E. Dieter and D. Bacon, *Mechanical metallurgy*, vol. 273, no. 4. London: McGraw-Hill, 1988.

[110] S. Morito, H. Saito, T. Ogawa, T. Furuhara, and T. Maki, 'Effect of austenite grain size on the morphology and crystallography of lath martensite in low carbon steels', *ISIJ International*, vol. 45, no. 1, pp. 91–94, 2005.

[111] S. Suresh, *Fatigue of Materials*. Cambridge University Press, 1998.

[112] R. De Finis, D. Palumbo, F. Ancona, and U. Galietti, 'Fatigue limit evaluation of various martensitic stainless steels with new robust thermographic data analysis', *International Journal of Fatigue*, vol. 74, pp. 88–96, 2015.

[113] A. Atrens, W. Hoffelner, T. W. Duerig, and J. E. Allison, 'Subsurface crack initiation in high cycle fatigue in Ti6A14V and in a typical martensitic stainless steel', *Scripta Metallurgica*, vol. 17, no. 5, pp. 601–606, 1983.

[114] C.-S. Shin, T. Do, D. Lee, T.-Y. So, S.-H. Ko, H. Chung, and P. Kwon, 'A comparative study on mechanical properties of fully dense 420 stainless steel parts produced by modified binder jet printing', *Materials & Design*, vol. 224, p. 111343, 2022.

[115] R. O. Ritchie, ‘Mechanisms of fatigue-crack propagation in ductile and brittle solids’, *International Journal of Fracture*, vol. 100, no. 1, pp. 55–83, 1999.

[116] S. Ueki, T. Matsumura, Y. Mine, S. Morito, and K. Takashima, ‘Microstructural fatigue crack growth in single-packet structures of ultra-low carbon steel lath martensite’, *Scripta Materialia*, vol. 173, pp. 80–85, 2019.

[117] M. García-Mazarío, A. M. Lancha, and M. Hernández-Mayoral, ‘Embrittlement susceptibility induced by impurities segregation to grain boundaries in martensitic steels candidates to be used in ADS’, *Journal of Nuclear Materials*, vol. 360, no. 3, pp. 293–303, 2007.

[118] J. C. Newman and I. S. Raju, ‘Stress-intensity factor equations for cracks in three-dimensional finite bodies subjected to tension and bending loads’, NASA-TM-85793, 1984

[119] G. N. Haidemenopoulos, A. T. Kermanidis, C. Malliaros, H. H. Dickert, P. Kucharzyk, and W. Bleck, ‘On the effect of austenite stability on high cycle fatigue of TRIP 700 steel’, *Materials Science and Engineering A*, vol. 573, pp. 7–11, 2013.

[120] Y. Zhang, S. Wang, G. Xu, G. Wang, and M. Zhao, ‘Effect of Microstructure on Fatigue-Crack Propagation of 18CrNiMo7-6 High-Strength Steel’, *International Journal of Fatigue*, vol. 163, p. 107027, 2022.

[121] Y. Murakami, *Metal Fatigue: Effects of Small Defects and Nonmetallic Inclusions*. Elsevier, 2002.

[122] K. Findley, R. Cryderman, A. B. Nissan, and D. K. Matlock, ‘The effects of inclusions on fatigue performance of steel alloys’, *AIST Transactions*, vol. 10, no. 6, pp. 234–243, 2013.

[123] I. Sabirov and O. Kolednik, ‘The effect of inclusion size on the local conditions for void nucleation near a crack tip in a mild steel’, *Scripta Materialia*, vol. 53, no. 12, pp. 1373–1378, 2005.

[124] P. Wang, P. Zhang, B. Wang, Y. Zhu, Z. Xu, and Z. Zhang, ‘Fatigue cracking criterion of high-strength steels induced by inclusions under high-cycle fatigue’, *Journal of Materials Science and Technology*, vol. 154, pp. 114–128, 2023.

[125] K. Hockauf, M. F.-X. Wagner, B. Mašek, and T. Lampke, ‘Mechanisms of fatigue crack propagation in a Q&P-processed steel’, *Materials Science and Engineering A*, vol. 754, pp. 18–28, 2019.

[126] Z. Z. Hu, M. L. Ma, Y. Q. Liu, and J. H. Liu, ‘The effect of austenite on low cycle fatigue in three-phase steel’, *International Journal of Fatigue*, vol. 19, no. 8–9, pp. 641–646, 1997.

[127] A. F. Bower, *Applied Mechanics of Solids*. CRC Press, 2009.

[128] S. Basak, S. K. Panda, and Y. N. Zhou, 'Formability assessment of prestrained automotive grade steel sheets using stress based and polar effective plastic strain-forming limit diagram', *Journal of Engineering Materials and Technology, Transactions of the ASME*, vol. 137, no. 4, 2015.

[129] 'TRIP steels'. Accessed: Apr. 23, 2023. [Online]. Available: https://automotive.arcelormittal.com/products/flat/first_gen_AHSS/TRIP

[130] D. De Knijf, R. Petrov, C. Föjer, and L. A. I. Kestens, 'Effect of fresh martensite on the stability of retained austenite in quenching and partitioning steel', *Materials Science and Engineering A*, vol. 615, pp. 107–115, 2014.

[131] M. E. Korkmaz and M. Günay, 'Finite Element Modelling of Cutting Forces and Power Consumption in Turning of AISI 420 Martensitic Stainless Steel', *Arabian Journal for Science and Engineering*, vol. 43, no. 9, pp. 4863–4870, 2018.

[132] M. Safari, S. J. Hosseinipour, and H. D. Azodi, 'Experimental and Numerical Analysis of Forming Limit Diagram (FLD) and Forming Limit Stress Diagram (FLSD)', *Materials Sciences and Applications*, vol. 02, no. 05, pp. 496–502, 2011.

[133] R. Hernández Rossi, A. Llobet Lorenzo, X. Gomez, and D. Riera Colom, 'FLSD as a good choice in sheet forming of AHSS', in *2011 SIMULIA Customer Conference*, 2011, pp. 238–246.

[134] K. Kolasangiani, M. Shariati, and K. Farhangdoost, 'Prediction of forming limit curves (FLD, MSFLD and FLSD) and necking time for SS304L sheet using finite element method and ductile fracture criteria', *Journal of Computational and Applied Research in Mechanical Engineering*, vol. 4, no. 2, pp. 121–132, 2015.

[135] Z. Zimniak, 'Implementation of the forming limit stress diagram in FEM simulations', *Journal of Materials Processing Technology*, vol. 106, no. 1–3, pp. 261–266, 2000.

[136] R. Hashemi, A. Assempour, and E. M. K. Abad, 'Implementation of the forming limit stress diagram to obtain suitable load path in tube hydroforming considering M-K model', *Materials and Design*, vol. 30, no. 9, pp. 3545–3553, 2009.

[137] M. Erfanian and R. Hashemi, 'A comparative study of the extended forming limit diagrams considering strain path, through-thickness normal and shear stress', *International Journal of Mechanical Sciences*, vol. 148, pp. 316–326, 2018.

[138] R. Hashemi and K. Abrinia, 'Analysis of the extended stress-based forming limit curve considering the effects of strain path and through-thickness normal stress', *Materials and Design*, vol. 54, pp. 670–677, 2014.

[139] 'Kirchoff Automotive - Pilar B'. Accessed: Dec. 22, 2022. [Online]. Available: https://www.kirchoff-automotive.com/

[140] I. Ragai, D. Lazim, and J. A. Nemes, 'Anisotropy and springback in draw-bending of stainless steel 410: Experimental and numerical study', *Journal of Materials Processing Technology*, vol. 166, no. 1, pp. 116–127, 2005.

[141] M. Kim, G. Bae, N. Park, and J. H. Song, ‘Springback Reduction of Ultra-High-Strength Martensitic Steel Sheet by Electrically Single-Pulsed Current’, *Materials*, vol. 15, no. 7, p. 2373, 2022.

[142] H. Medarac, J. A. Moya Rivera, and J. Somers, ‘Production costs from iron and steel industry in the EU and third countries’, Luxembourg, 2020.

[143] C. W. Forsberg, D. C. Stack, D. Curtis, G. Haratyk, and N. A. Sepulveda, ‘Converting excess low-price electricity into high-temperature stored heat for industry and high-value electricity production’, *Electricity Journal*, vol. 30, no. 6, pp. 42–52, 2017.

[144] Acerinox S.A., ‘ACERINOX Annual Report 2021’, Madrid, 2021.

[145] J. Somers, ‘Technologies to decarbonise the EU steel industry’, Luxembourg, 2022.

[146] I. S. S. Forum, ‘Stainless steel in figures 2015’, Brussels, 2015.

[147] B. A. McNulty and S. M. Jowitt, ‘Barriers to and uncertainties in understanding and quantifying global critical mineral and element supply’, *iScience*, vol. 24, no. 7, 2021.